Institut für Angewandte Physik

TU Dresden

Propagation, Scattering and Amplification of Surface Plasmons in Thin Silver Films

von

Jan Seidel

2005

Institut für Angewandte Physik

Fachrichtung Physik

Fakultät Mathematik und Naturwissenschaften

Technische Universität Dresden

Propagation, Scattering and Amplification of Surface Plasmons in Thin Silver Films

Dissertation

zur Erlangung des akademischen Grades

Doctor rerum naturalium

vorgelegt von

Jan Seidel

geboren am 16. September 1975 in Marienberg/Erzg.

Dresden 2005

eingereicht am 18. Januar 2005

Gutachter: Prof. Dr. Lukas M. Eng

Prof. Dr. Joachim R. Krenn

Prof. Dr. William L. Barnes

Abstract

Plasmons, i.e. collective oscillations of conduction electrons, have a strong influence on the optical properties of metal micro- and nanostructures and are of great interest for novel photonic devices. Here, plasmons on metal-dielectric interfaces are investigated using near-field optical microscopy and differential angular reflectance spectroscopy. Emphasis is placed on the study of plasmon interaction with individual nanostructures and on the nonlinear process of surface plasmon amplification.

Specifically, plasmon transmission across single grooves in thin silver films is investigated with the help of a near-field optical microscope. It is found that plasmon transmittance as a function of groove width shows a non-monotonic behavior, exhibiting certain favorable groove widths with strongly decreased transmittance values. Additionally, evidence of groove-mediated plasmon mode coupling is observed. Spatial beating due to different plasmon wave vectors produces distinct interference features in near-field optical images. A theoretical approach explains these observations and gives estimated coupling efficiencies deduced from visibility considerations.

Furthermore, stimulated emission of surface plasmons induced by optical pumping using an organic dye solution is demonstrated for the first time. For this a novel twin-attenuated-total-reflection scheme is introduced. The experiment is described by a theoretical model which exhibits very good agreement. Together they provide clear evidence of the claimed process.

Contents

List of Figures

List of Tables

1 Introduction

Current technological progress involves quantum electronic devices such as quantum wells, quantum dots, single-electron transistors, as well as photonic devices such as wave guides, photonic crystals and others for information processing applications. Managing data requires devices that transform signals between optical and electronic functional structures and vice-versa, although there is a tendency to replace slow electronic devices completely by faster photonic ones. The scaling of photonic and optoelectronic devices to smaller and smaller dimensions and their assembly in integrated circuits requires novel approaches to light manipulation.

One approach is based on photonic crystals. They allow the control of dispersion and propagation of light in a periodic photonic crystal structure [Johnson et al., 2002]. The tailoring of desired properties has led to photonic band-gap structures, which provide efficient interconnection between elements of photonic circuits and passive components, such as filters, waveguides, nanocavities, and others. Implementation of all-optical integrated circuits also requires active photonic elements capable of optically performing operations analogous to their electronic counterparts. Linear optical properties and light manipulation in photonic crystals are significantly developed, however, nonlinear optical effects which are required for the development of all-optical integrated circuits (e.g optical transistors) are much less investigated.

Another approach to photonic integration is based on surface plasmon polariton optics. Surface plasmons (SPs) are surface-bound electromagnetic waves supported by metals [Raether 1988]. Recent years have seen a strong revival of the interest in such excitations, motivated by the possibility they of-

fer for realizing a strong spatial confinement of electromagnetic fields. Because SPs are surface-bound waves, light manipulation can be restricted to only two dimensions. This significantly simplifies the procedure, e.g. full band gaps are much easier to achieve in two dimensions. The SP electromagnetic field decays exponentially from the surface, thus it cannot be observed before it is scattered into light, e.g. at surface defects or specific functional structures.

Near field optics and surface plasmons are related physical phenomena. Both involve excitation and propagation of high-frequency electromagnetic fields in environments composed of different materials. Evanescent (i.e. interface bound) fields are a key point in both topics [e.g. see De Fornel et al., 2001]. Research activities in the two fields strongly influence each other and this has lead to much fruitful cross-thinking [Kawata, 2001]. With the development of scanning near-field optical microscopy (SNOM) [Pohl et al., 1984] it became possible to probe the SP field directly at the surface [Reddick et al., 1989; Courjon et al., 1989; de Fornel et al., 1989; Marti et al., 1993; Adam et al., 1993; Dawson et al., 1994, 2001; Tsai et al., 1994; Bozhevolnyi et al., 1995]. The scattering of SPs and localization have been investigated in order to establish the idea of two-dimensional SP optics [Tsai et al., 1994; Bozhevolnyi et al., 1995, 1996; Hecht et al., 1996; Krenn et al., 1999; Bouhelier et al., 1999; Knoll et al., 1999; Weeber et al., 2001; Barnes et al., 2003;]. Two-dimensional SP photonic crystals exhibiting a plasmonic band-gap have also been reported [Laks et al., 1981; Glass et al., 1984; Barnes et al., 1996; Salomon et al., 2001; Bozhevolnyi et al., 2001]. Moreover, SP waveguiding in SP crystals, enhanced optical transmission through nanosize holes, as well as light-controlled optical switching have been demonstrated [Glass et al., 1984; Barnes et al., 1996; Ebbesen et al., 1998; Salomon et al., 2001; Bozhevolnyi et al., 2001; Smolyaninov et al., 2002]. Many interesting "plasmon optical devices" were brought forward [Krenn et al., 2002 and 2004], for example waveguides [Weeber et al., 2001], mirrors [Bozhevolnyi et al., 1997], and a plasmon interferometer [Ditlbacher et al., 2002]. It is now widely expected that SPs will play an important role in future integrated nanooptical devices.

Historical Milestones Releated to Plasmon Research

In 1704 Newton observed frustrated total reflection when he brought a totally reflecting prism face in contact with a convex lens, thus he discovered evanescent electromagnetic fields (or near-fields), although he did not know about the field concept [Newton, 1704]. Zenneck in 1907 and Sommerfeld in 1909 demonstrated theoretically that radio frequency surface electromagnetic waves occur at the boundary of two media when one medium is either a "lossy" dielectric, or a metal, and the other is a loss-free medium (note: error in sign in [Sommerfeld, 1909], see [Norton, 1935]; see also [Bouwkamp, 1950] for a review of previous work) [Zenneck, 1907; Sommerfeld, 1909]. Fano suggested in 1936 that surface electromagnetic waves were responsible for the anomalies in the continuous-source diffraction spectra of metallic gratings (Wood's anomalies) [Fano, 1936, 1937, 1938]. In 1957 Ritchie showed theoretically the existence of surface plasma excitations at a metal surface [Ritchie, 1957]. In 1958 Stern and Ferrell pointed out theoretically that surface electromagnetic waves at a metallic surface involve electromagnetic radiation coupled to surface plasmons. They derived, for the first time, the dispersion relation for surface electromagnetic waves at metal surfaces [Ferrell, 1958]. Powell and Swan (1960) observed the excitation of surface plasmons at metal interfaces (thin metal foils) using electrons [Powell & Swan, 1960]. Otto in 1969 devised the attenuated-total-reflection (ATR) method for the coupling of bulk electromagnetic waves to surface electromagnetic waves at optical frequencies [Otto, 1968]. Kretschmann and Raether modified the Otto geometry in the same year, proposing the now most widely used device geometry [Kretschmann and Raether, 1968]. In the following years strong interest lead to numerous publications. A good overview until the beginning of the eighties can be found in a book by Agranovich [Agranovich, 1982]. After this period interest faded. Since the invention of scanning probe techniques many approaches to investigating surface plasmons became known, but it dates back only to the nineties of the last century when systematic investigations lead to a revival of the research on surface plasmons.

Objective and Outline

The objective of this work is to investigate local surface plasmon properties in thin metal films. This includes imaging of surface plasmon fields by near-field optical microscopy, understanding of near-field image contrast and influence of different near-field probes. Single grooves in the plasmon-supporting metal film will be studied with respect to their influence on surface plasmon propagation. Especially plasmon transmission properties across grooves are addressed, since a non-monotonic dependance on groove width is expected [Maradudin et al., 1983].

Furthermore, the possibility of stimulated emission of surface plasmons will be treated theoretically and the feasibility of experimental implementations will be examined. Amplification of surface plasmons is of great interest for application in nanooptics [Stockman et al., 2003]. Large spatial field fluctuations and energy concentration in nanosize volumes and the according strong enhancement of optical responses are of interest in many research fields [Alivisatos et al., 1998; Shipway et al., 2000, Xia et al., 2000].

This work is organised as follows: First, I will briefly review the most important electrodynamical and solid-state-theoretical concepts that are relevant to this work in chapter 2. Subsequently, I will discuss experimental methods and materials that were used in this work in chapter 3. Chapter 4 and 5 present results. In particular I will describe and discuss experimental findings and developed theoretical models. I will compare them and I will also point to open questions and possible applications. A brief summary concludes this work, describing all important findings and giving an outlook for possible routes to follow with this work in mind.

2 Fundamental Concepts of Surface Plasmons and Organic Fluorescent Dyes

In this chapter the necessary theoretical background related to this thesis is presented. Certain properties of surface plasmons are discussed that are important for the understanding of the following chapters. Emphasis is also placed on various properties of fluorescent dyes since they are necessary for the discussion of stimulated plasmon emission in chapter 5.

2.1 Properties of Surface Plasmons

2.1.1 The Term "Surface Plasmon"

"A trapped surface mode which has electromagnetic fields decaying into both media but which, tied to the oscillatory surface charge density, propagates along the interface."

R. J. Sambles 1991

"We are dealing with a resonant excitation of a coupled state between the plasma oscillations and the photons, i.e., the plasmon surface polariton."

W. Knoll 1991

The free-electron model of electrons in metals leads to a dielectric function $\epsilon(\omega)$ that can be written [Drude, 1900]:

$$\epsilon(\omega) \cong 1 - \frac{\omega_P^2}{\omega^2} \tag{2.1}$$

where ω_P is the plasma frequency. The scattering of electrons is not considered in this case. The dielectric displacement is given by

$$\overrightarrow{D} = \epsilon_0 \overrightarrow{E} + \overrightarrow{P} = \epsilon_0 \epsilon(\omega) \overrightarrow{E}. \tag{2.2}$$

The solution of the electromagnetic wave equation [e.g. see Landau and Lifshitz, 1980] leads to the conclusion that surface plasmons in this model can only be achieved when $\epsilon(\omega)$ is negative (a rigorous derivation of this condition can be found in a book by Agranovich and Mills [Agranovich and Mills, 1982, p. 7 ff]). In this case the electrical polarisation is 180° out of phase with the exciting electrical field. If the considered medium has an absorption line at ω_0, excitation of the medium just above ω_0 will produce a negative contribution to the electrical polarisation that can be very large. In this case the electromagnetic wave can be described as a coupled mode consisting of the electromagnetic field and the elementary excitation leading to the resonance at ω_0. Such electromagnetic waves are commonly referred to as polaritons, hence the terminus surface plasmon polaritons, which would be a correct description of the phenomenon. Because the distinction of surface plasmons and surface plasmon polaritons can not be considered a central part in this work, I will use the term surface plasmons or shorter, plasmons.

Similar effects related to collective two-dimensional free-electron excitations are known for different systems such as semiconductor surfaces or electrons above a liquid helium surface [Burstein et al., 1980; Andrei, 1997]. In the frequency range below the plasma frequency, where the real part of the dielectric constant is negative, related electromagnetic properties are significantly different from the properties of ordinary dielectric materials. In this frequency range the wave vector of light in the medium is imaginary, and therefore there are no propagating electromagnetic modes in such a medium. The frequency ω_{sp} of a surface plasmon on a flat surface of a semi-infinite metal can be easily determined from the frequency of a bulk plasmon in the metal as it corresponds to $\mathrm{Re}\{\epsilon_m(\omega_{sp})\} = -\epsilon_i$, where $\epsilon_i > 0$ is the dielectric constant of the adjacent dielectric medium. For a Drude metal in contact with vacuum $\omega_{sp} = \omega_p/\sqrt{2}$. Different surface effects and non-local effects in real metals can contribute to

corrections to the surface plasmon frequency. For a review of previous work see the books by Agranovich and Boardman [Agranovich, 1982; Boardman, 1982].

2.1.2 The Attenuated-Total-Reflection (ATR) Method

The most elementary SP is a SP propagating along the flat interface between a metallic and a dielectric half-space. The plasmon field decays exponentially as an evanescent wave in the direction normal to the interface both into the metal and into the dielectric (with different decay lengths) and, hence, does not couple to any freely propagating electromagnetic mode (this means that it cannot be excited by light impinging on the interface).

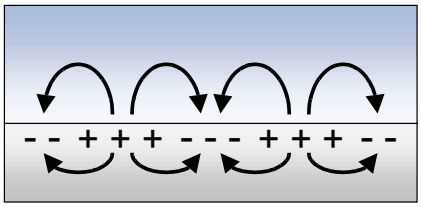

Fig. 2.1. Electromagnetic field pattern associated with charge oscillations at a metal surface.

In the case of a metal film bounded by two dielectrics, there are two plasmon modes. As long as the film is not too thin, each mode can be assigned to one of the interfaces, where its field is concentrated. The situation remains similar to the former case, each mode being characterized by evanescent waves on both sides of the respective interface. The field of the plasmon localized at one interface decays across the metal film and a small residual field extends across the other interface into the second dielectric. However, provided that this is the dielectric with the higher index of refraction, the field may now become propagating rather than remaining evanescent.

This is the effect used in the attenuated-total-reflection configuration (also called Kretschmann-Raether configuration after its inventors) for exciting SPs by light [Raether, 1988]: A metal film is bounded by air on one side and by a glass substrate on the other side (see Fig. 2.2 a). The SP at the metal-air interface couples weakly to a freely propagating mode in the glass. Hence, the

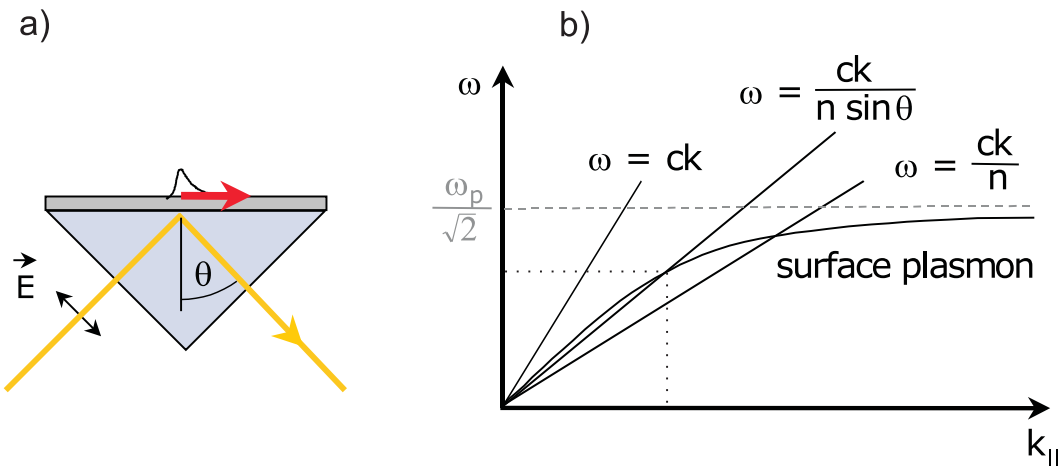

Fig. 2.2. Kretschmann-Raether configuration. A thin metal film is bounded by air on one side and by a glass prism on the other side (a). For a given photon energy, momentum matching with the plasmon at $k_{\|}$ is achieved by adjusting the light incidence angle θ for a prism with refractive index n, indicated by dotted lines in the dispersion relation in (b). ω_P denotes the plasma frequency according to the Drude model.

SP can now be excited by light incident from the glass side at a specific angle θ_{sp} (always lying in the range of total internal reflection) given as:

$$\theta_{sp} = \arcsin\left(\sqrt{\frac{\epsilon'_m}{\epsilon'_m + 1}}\; n^{-1}\right), \tag{2.3}$$

with n being the refractive index of the substrate that supports the metal film. For a given photon energy, momentum matching with the plasmon at $k_{\|}$ (wave vector in the surface plane) is achieved by adjusting the light incidence angle θ, indicated by dotted lines in the dispersion relation in Fig. 2.2 b). At the same time, the SP now suffers from radiative loss and is therefore more strongly damped. The SP at the metal-glass interface, however, remains decoupled from any freely propagating light wave.

Figure 2.3 shows how surface plasmon excitation depends on the polarisation of the exciting light. For p-polarised incident light the plasmon is efficiently excited as indicated by the missing reflected light (dark line in fig. 2.3 a)). Additionally, the total internal reflection edge is visible (fig. 2.3 a)). S polarisation does not lead to excitation of plasmons, hence there is no dark

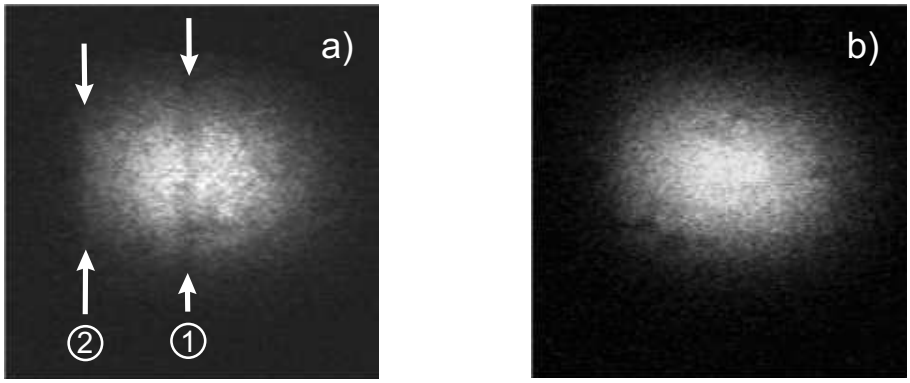

Fig. 2.3. Polarisation-dependant excitation of surface plasmons: a) reflected spot, p polarisation; b) reflected spot, s polarisation. Note the dark line at the angle of plasmon excitation (1) and the total internal reflection edge (2).

line in the reflected light spot (fig. 2.3 b)).

2.1.3 Electromagnetic Field Distribution and Energy Dissipation

The calculation of the electromagnetic field distribution of a plasmon increases the understanding of different modes propagating in thin metal films. If one achieves low field strengths inside the metal film, low loss and thus long propagation lengths are possible [Kretschmann, 1972; Kovacs and Scott, 1977; Sarid, 1981; Craig et al., 1983; Ctyroky et al., 1999]. In the following an approach to calculating the magnetic field distribution of a coupled surface plasmon mode (including the influence of the ATR prism coupling) is shown based on electromagnetic theory in stratified media [e.g. see Wait, 1996]. An incident monochromatic plane wave is assumed, and by using appropriate boundary conditions the electric and magnetic field components are calculated. The Poynting vector field $\overrightarrow{S}$ gives the energy flux associated with the electromagnetic field. The calculation of $\overrightarrow{S}$ for the condition of a resonance minimum of the reflection curve shows at which interface the SP field is excited.

A schematic description of the problem is shown in Figure 2.4. A metallic layer is surrounded by several dielectric layers with differing optical properties. Layer 1 can be understood as spacing layer (e.g. compare the Sarid geometry [Sarid, 1981]) and it may be disregarded by filling it with the same material

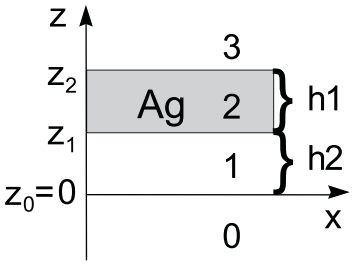

Fig. 2.4. Sketch for the calculation of electromagnetic fields of plasmons in stratified media. Layers 0, 1 and 3 denote variable dielectric materials.

as layer 0, which is essentially the coupling layer (e.g. a glass prism) resulting in the Kretschmann geometry. At the boundary between layers 0 and 1 total internal reflection of the incoming wave creates an evanescent field which couples to layer 2 where it is used for plasmon excitation. The individual field components in a multilayer geometry with layers m=1 ... n are characterized by a reflected and a transmitted part at each interface such as

$$H_{my} = [a_m e^{-u_m z} + b_m e^{u_m z}] e^{-ik_{\text{II}} x}, \tag{2.4}$$

where a_m and b_m are coefficients describing the strength of reflected and transmitted parts, and u_m is given by

$$u_m^2 - k_{\text{II}}^2 = -\varepsilon_m \, \mu_m \frac{\omega^2}{c^2}, \tag{2.5}$$

where ε_m is the permittivity and the permeability μ_m is assumed to be 1. Boundary conditions concerning the continuity of H_y and the derivative of H_y apply as

$$H_{m-1,y} = H_{m,y} \quad \text{and} \quad \frac{\partial H_{m-1,y}}{\partial z} = \frac{\partial H_{m,y}}{\partial z}. \tag{2.6}$$

By solving the given system of equations also the electric field components are determined by using

$$\vec{\nabla} \times \vec{H} = \dot{\vec{D}} \tag{2.7}$$

which leads to expressions for the x and z components of the electric field in the form

$$E_x = -\frac{1}{i\omega\varepsilon_0\varepsilon}\frac{\partial H_y}{\partial z} \quad \text{and} \quad E_z = -\frac{1}{i\omega\varepsilon_0\varepsilon}\frac{\partial H_y}{\partial x}. \tag{2.8}$$

Since we assume an infinite plane wave, the only variation in the Poynting vector field occurs along the z direction, i.e. perpendicular to the film surface plane. The time-averaged divergence of the Poynting vector field given by

$$\langle \overrightarrow{\nabla} \cdot \overrightarrow{S} \rangle = \frac{1}{2}\, \omega\, \varepsilon_0\, \varepsilon''\, |\overrightarrow{E}|^2, \tag{2.9}$$

where ε'' denotes the imaginary part of the dielectric constant, is a direct representation of loss in the system as it describes source or sink terms associated with that vector field.

A complete numerical mathematical solution to the geometry discussed above using *MATHEMATICA*® can be found in appendix A.

Some results for a silver film of 60 nm thickness are shown in figure 2.5. Electric and magnetic components of the plasmon field, which are normalized to their incident amplitude, are localized on the silver-air interface, H_y and E_z being enhanced by a factor of about 10 and E_x by a factor of about 2.5. The only material in the calculation that has a nonvanishing value of ε'' is the silver film. Therefore, only in this layer losses are expected, which are also located on the silver-air interface, as seen in figure 2.5 (d).

The energy of the surface plasmon is subject to dissipation as seen in Figure 2.5 (d). There are two main damping mechanisms. The first one, internal damping Γ_{int}, can be understood by envisioning a time-dependant current $\overrightarrow{j}(t)$ associated with the plasmon oscillation that feels the frequency-dependant resistance of the metal. As described by the imaginary part ϵ'' of the dielectric constant, plasmon energy is finally converted to heat through nonradiative channels. Note that although the Poynting vector can give considerable information about the nature of the excitation in a metal film, it does not give a complete description. The time-averaged values do not necessarily reflect local current and charge distributions, which are time-dependent. Therefore, SP waves which are coupled between two interfaces may exhibit quite similar

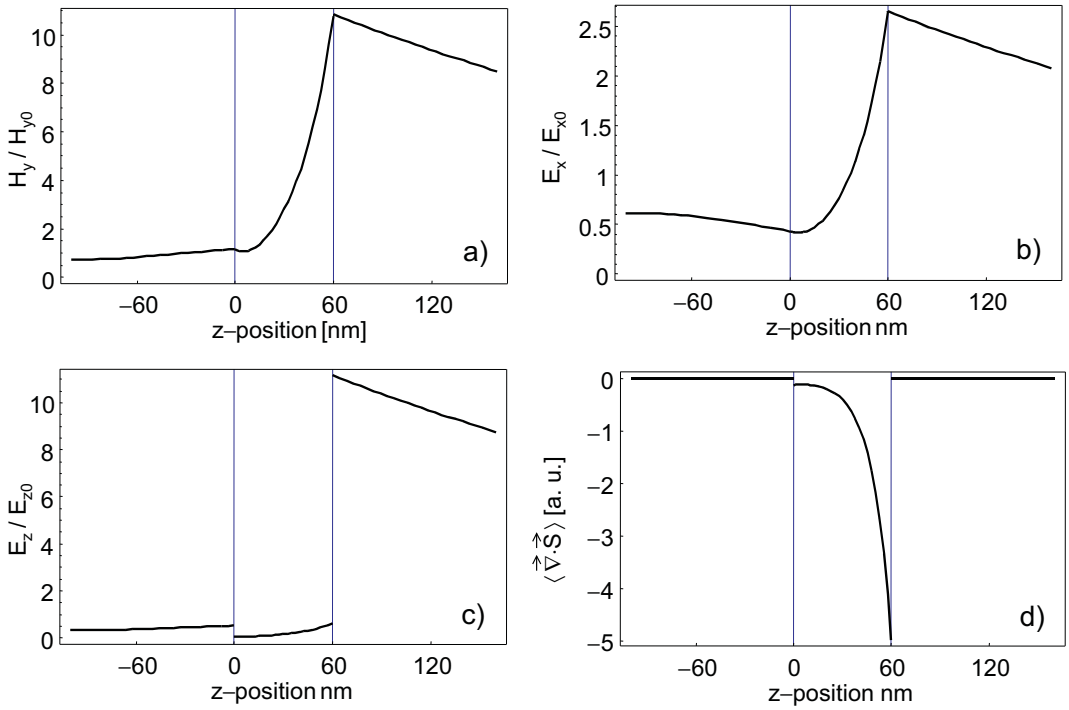

Fig. 2.5. Calculation of electric and magnetic components of the plasmon field (normalized to their incident amplitude) and energy dissipation in a 60 nm thick silver film (reaching from z=0 nm to z=60 nm, position indicated by vertical lines). The light incidence angle was chosen to give maximum plasmon excitation with the optical constants of silver at a wavelength of 632.8 nm [Schröder, 1981].

Poynting vector profiles, but the nature of the associated oscillations can be quite different [Kovacs et al., 1977]. The second dissipative channel, radiation damping Γ_{rad}, occurs because the wave vector of the evanescent plasmon field matches the wave vector of plane waves in an adjacent dielectric medium (e.g. the glass prism in the Kretschmann configuration). This back-coupled radiation can be observed as directional scattering [Simon et al., 1976].

2.1.4 Reflectance Spectra

The angle-dependant reflection is also a function of the thickness of the metal film. By solving Maxwell's equations for stratified media, as explained in the previous section, the curves in figure 2.6 were calculated.

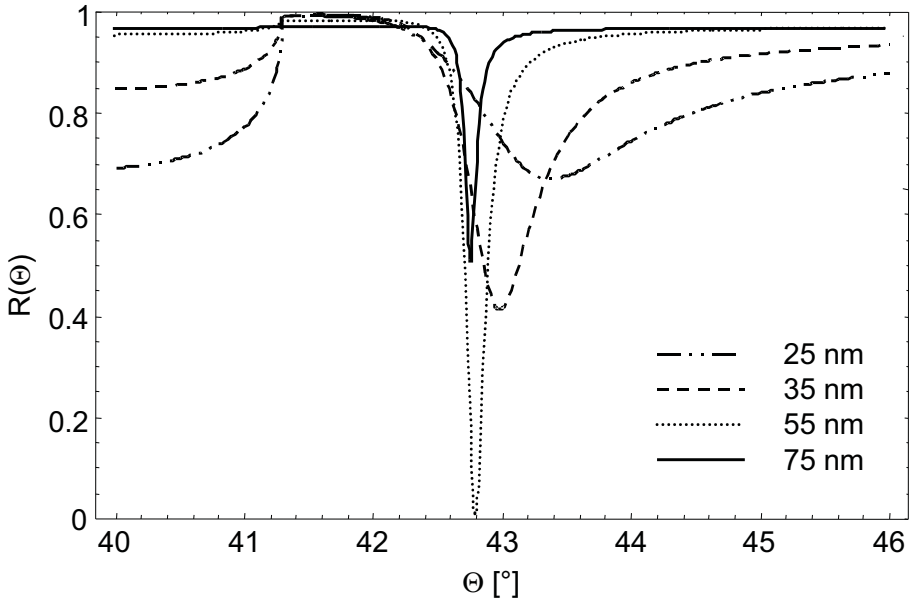

Fig. 2.6. Angle-dependant reflection for different silver film thicknesses at a wavelength of 632.8 nm.

For thin films of ∼25 nm thickness the reflection dip appears broad and shallow. This behavior is explained by increased radiation damping. At about 55 nm the reflectance reaches a minimum depending on the dielectric function of silver (experimental data varies slightly in the literature, e.g. see [Raether 1988]). For thicker films the evanescent field of the incident wave couples less to the surface plasmon field. The half width of the reflectance dip approaches a constant value, however, the absolute depth decreases.

2.1.5 Line Width versus Propagation Length

From the line width of angle-dependent reflection measurements in the ATR geometry the lifetime of the plasmon and accordingly its propagation length can be determined as shown below. Starting with

$$\Delta\theta = \frac{2\ \mathrm{Im}(k)}{n\frac{\omega}{c}\cos\theta} \tag{2.10}$$

where θ is the reflectance dip position and $\Delta\theta$ is the line width of the dip [Bruns and Raether, 1970], and using

$$L = \frac{1}{2\ \mathrm{Im}(k)} \tag{2.11}$$

as an expression for the plasmon propagation length L, one can write

$$L = \frac{1}{\Delta\theta\ n\frac{\omega}{c}\cos\theta} \tag{2.12}$$

A thorough investigation of ATR experiments and comparative SNOM investigations were published recently [Dawson et al., 2001].

2.2 Properties of Fluorescent Dyes

2.2.1 Fluorescent Dye Interna

Laser dyes are organic compounds that may relax radiatively after optical excitation, emitting in the visible or infrared range. Since the development of the first dye laser [Sorokin et al., 1966] many different dyes have been investigated with respect to their fluorescent properties. Almost all of them exhibit basic features, which will be discussed in this chapter. Organic dyes exhibit a strong absorption in the visible electromagnetic spectrum, which is attributed to a transition from the electronic ground state S_0 to the first excited singlet state S_1. The reverse process produces fluorescence light usually by spontaneous emission. The transition matrix element of this transition is very high resulting in a short lifetime of the S_1 state in the order of nanoseconds. By pumping the dye solution optically usually some higher vibronic sublevel of the S_1 state is reached but relaxation to the lowest vibronic level of S_1 takes only a few picoseconds. Such a fast vibronic relaxation also takes place in the vibronic sublevels of the S_0 state, so that a four-level laser system is formed in which inversion is easily achieved.

For the use in dye lasers only radiative transitions from the S_1 level of the dye are desired. However, there are many lossy processes taking place that compete with the fluorescence of the dye. Nonradiative processes include relaxation to the ground state and intersystem crossing to triplet states.

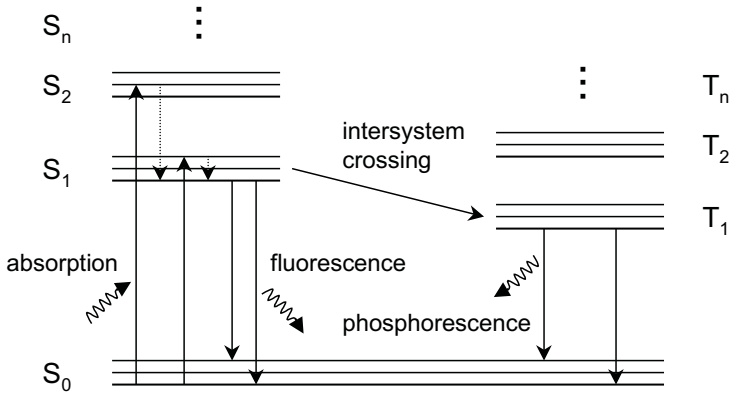

Fig. 2.7. Jabłoński diagram of a fluorescent dye.

2.2.2 Intersystem Crossing

Relaxation of dye molecules from singlet to triplet states may lead to strong loss. Triplet states have lifetimes in the order of microseconds or longer, and may thus become populated over time even if intersystem crossing rates are small. As a consequence only a fraction of the molecules in the dye solution contribute to fluorescence from S_1 to S_0. As a quantum mechanically unlikely process, because of the involved spin change, intersystem crossing usually is a weak effect. Its dependance on π electron distribution was pointed out by Drexhage [Drexhage, 1972] following experimental observations. Increased spin-orbit coupling enhances the effect.

2.2.3 Absorption of Higher Singlet and Triplet States

Absorption may also occur in excited molecules. These include absorption of molecules in excited singlet states S_1 to S_n and absorption of molecules in excited triplet states T_1 to T_n. Absorption spectra of higher singlet states are difficult to determine experimentally because of the short lifetime of these states. Absorption spectra of triplet states are more easily measured, for example by high-intensity flashlamp photolysis. Some data for rhodamine 101 are available [Beaumont et al., 1993].

2.2.4 Photostability

A fundamental prerequisite in order to use organic fluorescent molecules effectively for example as luminophores in flat-screen displays, as sensors, optical amplifiers, and in fiber optics, they must be able to withstand repeated excitations and the large amounts of energy that will be cycled through them. Unfortunately, upon repeated absorption, the dye molecules begin to photooxidize, and they consequently loose the ability to fluoresce [Lakowicz, 1999; Mackey et al., 2001]. This occurs because of a weak probability that an excited molecule undergoes a transition to a chemically altered state as a result of a reaction with e.g. oxygen or water, rather than simply relaxing back to the ground state of the non-reacted molecule [Schäfer et al., 1992].

Designing highly photostable dyes requires understanding of the various electronic states of excited electrons (S_n states, as well as T_n states), as well as the lifetimes associated with each of these states. Among other factors, the photostability of organic dyes depends strongly on the nature of the solvent used [Magde et al., 1979; Moore et al., 1978; Narasimhan et al., 1988] (this includes rigid embedding of the molecules in a polymer host, i.e. in a "solid solution"). Photodegradation of the dye molecule and subsequent reactions of the degraded products amongst themselves, or with the solvent molecules, is a complex phenomenon. For example, xanthene dyes have been reported to exhibit higher photostability when dissolved in water instead of commonly used organic solvents such as ethanol or methanol [Moore et al., 1978; Narasimhan et al., 1988]. Additionally, solvent purity is known to appreciably affect the process of photodegradation [Drexhage, 1973].

2.2.5 Other Effects in Fluorescent Dyes

Among others, additional lossy effects are charge transfer interactions, radiationless energy transfer, dye molecule aggregation and molecule reactions in the excited state. Charge transfer is known as quenching process that involves anions such as e.g. Cl^- or I^-. Concentration and polarity of solvents play an important role. The iodide anion in rhodamine 6G, for example, does not influence fluorescence if solved in ethanol. However, if it is solved in chloroform, which is nonpolar, the fluorescence becomes strongly quenched [Drexhage et

al., 1973]. There are also other compounds leading to similar fluorescence quenching [Pringsheim, 1949; Förster, 1951; Leonhardt et al., 1962]. Energy transfer to suitable energy levels of nearby (∼10 nm) molecules may also occur [Förster, 1951, 1959; Kellogg, 1970; Birks, 1970]. Substances such as molecular oxygen [Snavely et al., 1969; Marling et al., 1970], COT (cyclooctatetraene) [Wehry, 1967; Becker, 1969], and others [Marling, 1970, 1971] have been reported to quench triplet states (see also the work by Thiel for reference [Thiel, 1996]). Aggregation of dye molecules resulting in dimers or multimers can be observed as a change in the fluorescence spectrum, often appearing as an additional band at lower energies [Förster, 1951]. In addition, the fluorescence is usually considerably weaker than for monomers. A discussion can be found in a work by Drexhage [Drexhage, 1973]. Another influence on fluorescence properties is the chemical interaction of excited molecules with nonexcited ones [Förster, 1951; Baranova, 1965].

3 Experimental Methods and Materials

In this chapter emphasis is placed on experimental techniques for fabrication and analysis of plasmonic structures. The chapter concludes with information on the preparation of silver films, SNOM probes and dye solutions.

3.1 Methods

3.1.1 Scanning Near-field Optical Microscopy (SNOM)

The resolution attainable in conventional optical microscopy is limited because of diffraction. Abbe realized that, due to the finite size of lenses, only part of the propagating light waves can be collected [Abbe, 1873]. He proposed a so-called point-spread-function (PSF) which gives the intensity profile in the image plane due to a point source in the object plane. Rayleigh pointed out that objects are resolved when the maximum of one pattern coincides with the (first) minimum of the other, thereby defining the Rayleigh diffraction limit of lateral resolution Δx [Rayleigh, 1879]. It is determined by the wavelength λ of the radiation in use and by the numerical aperture (NA) of the imaging optics :

$$\Delta x \geq \frac{1.22\ \lambda}{2\ \mathrm{NA}} \tag{3.1}$$

The axial resolution Δz is also limited [Muchel, 1988]:

$$\Delta z \geq \frac{2\ \lambda}{\mathrm{NA}^2} \tag{3.2}$$

Hence, a straightforward method to increase the resolution in conventional microscopy is to increase the numerical aperture or decrease the wavelength. However, the practical limit of the numerical aperture is about 1.4, and the light wavelength cannot always be lowered, since information about the sample may be accessible only at larger wavelengths. By using a confocal microscope setup invented by Minsky in 1957, the resolution may be additionally improved by a factor of about 1.4 [Minsky, 1988].

However, the above said is true only for large distances between the light source and the imaging system, also called the far-field regime. Here the electromagnetic field can be described by propagating wave fronts. Very close to a surface this is different. There exist propagating as well as nonpropagating field components, the latter bound to the surface. These surface-bound waves contain optical information described by k vectors that are larger than the k vector of light in vacuo. Therefore they contain optical information about structures smaller than the Rayleigh limit. One possibility to exploit the near-field for high resolution optical imaging is scanning near-field optical microscopy (SNOM) (there are also other methods to increase optical resolution, e. g. [Hell et al., 1992; Klar et al. 2001; Dyba et al., 2002]). This method was first proposed by Synge [Synge, 1928]. Its essential points are an aperture that is smaller than the light wavelength and the fact that this aperture is brought within a distance $d \ll \lambda$ to the region of investigation.

This principle was first proven for microwaves by Ash and co-workers [Ash et al., 1972]. The first working near-field optical microscope for visible light was used by Pohl et al. in 1984 demonstrating a resolution of $\lambda/20$ [Pohl et al., 1984]. They used metal-coated sharpened optical fibers as a probe. The SNOM can be used in so-called transmission mode for light collection or illumination, e.g. by employing an inverted optical microscope. It is also possible to use it in reflection mode, which is usually applied to the study of opaque or solid samples. Other ways to illuminate the sample, such as shining light under a total-internal-reflection angle on a prism onto which the sample is placed, are also used. A second SNOM type makes use of Babinet′s principle by employing a sharp tip for light scattering instead of an aperture for illumination or

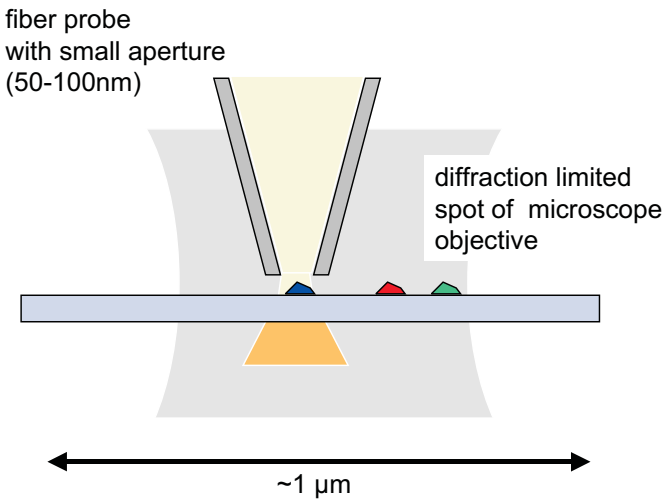

Fig. 3.1. SNOM principle. The diffraction limitation of the free space spot size is overcome by using an aperture smaller than the light wavelength.

light collection. This method was proposed by Wickramasinghe and Williams [Wickramasinghe and Williams, 1989] and has been demonstrated to provide optical resolution in the order of 10 nm [Hamann et al., 1998; Hillenbrand et al., 2000; Labardi et al., 2000].

With the development of scanning probe microscopy (SPM) techniques it became possible to study the properties of SPs directly at the surface where they propagate, with a resolution in the nanometer range. The first SPM applied to study SPs was a scanning tunnelling microscope (STM). The detection mechanism was based on detection of the additional tunnelling currents induced by SPs [Möller et al., 1991; Kroo et al., 1991; Baur et al., 1993; Smolyaninov et al., 1995] or the far-field-scattered light caused by local SP interaction with the STM tip [Specht et al., 1992]. There were also other approaches, where an atomic force microscope (AFM) was used [de Hollander et al., 1995; Kim et al., 1996]. Such experiments provide, in a first approximation, information on the SP field. However, the metal or silicon tips introduce significant perturbations in the SP field due to the field enhancement effects of localized SPs and the lightning-rod effect, which is essentially a geometrical effect at surfaces of large curvature (e.g. edges) [Zayats, 1999; Rendell et al., 1981]. These effects prevent to a great extent the direct measurement of the

local SP field [Zayats, 1999], as they depend on the topology, size and mutual position of tip and surface. SNOM with uncoated optical fibre tips, which is often also referred to as photon scanning tunnelling microscopy (PSTM) [Reddick et al., 1989; Courjon et al., 1989; de Fornel et al., 1989], provides the possibility to probe the surface polariton field directly above a surface [Pohl et al., 1993].

3.1.2 Focussed Ion Beam (FIB) Structuring

Focussed-ion-beam (FIB) structuring can be considered a standard in current semiconductor industry. Applications such as defect analysis, circuit modification, mask repair and transmission-electron-microscope sample preparation of specific locations on integrated circuits have become commonplace procedures. Focussed-ion-beam systems use a finely focused beam of usually gallium ions which can be operated at low beam currents for imaging or high beam currents for site specific sputtering, milling, and implantation.

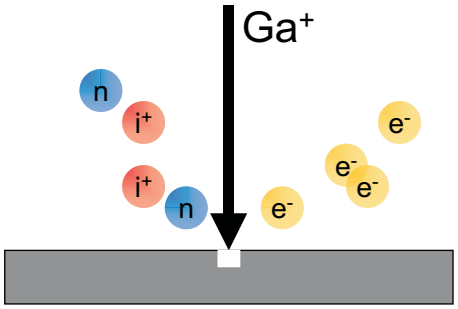

Fig. 3.2. Focussed-ion-beam principle. Positively charged gallium ions hit the sample surface thereby sputtering secondary ions i^+, neutral atoms n, and secondary electrons e^-.

As shown in Fig. 3.2, the gallium primary ions hit the sample surface and sputter a small amount of material, which leaves the surface as either secondary ions or neutral atoms. The primary beam also produces secondary electrons. As revealed by Monte Carlo simulations, the main part of the ion kinetic energy is transferred through incremental collisions with target atoms and is eventually transformed into heat [Lee et al., 1998]. However, a small fraction of the ions will successfully transfer enough momentum to target atoms

to dislodge them from their lattice positions. Such an atom may then transfer momentum to one or more neighbouring lattice atoms. This continuous exchange of energy among lattice atoms, known as the cascade effect, eventually leads to the ejection of atoms from the target surface.

It was discovered that within a crystalline lattice momentum is most efficiently transferred along close-packed atomic directions. For face-centered cubic (fcc) materials, which is the case for silver, the atoms are preferentially ejected from surface grains along a trajectory parallel to the [110] direction [Wehner, 1955]. An accurate model for the direction-dependant sputter yield $S_{(hkl)}$ of single-crystal copper and silver suggests that [Magnusen et al., 1963]

$$S_{(hkl)} = K_{(hkl)}\sqrt{E}P_{c(hkl)} \tag{3.3}$$

where $K_{(hkl)}$ accounts for system factors, and the remaining term addresses the probability of successful collisions of ions with target atoms as dependent on crystal orientation. Magnusen at al. also showed that the sputter yield of fcc crystals varies with orientation such that $S_{(111)} > S_{(001)} > S_{(011)}$.

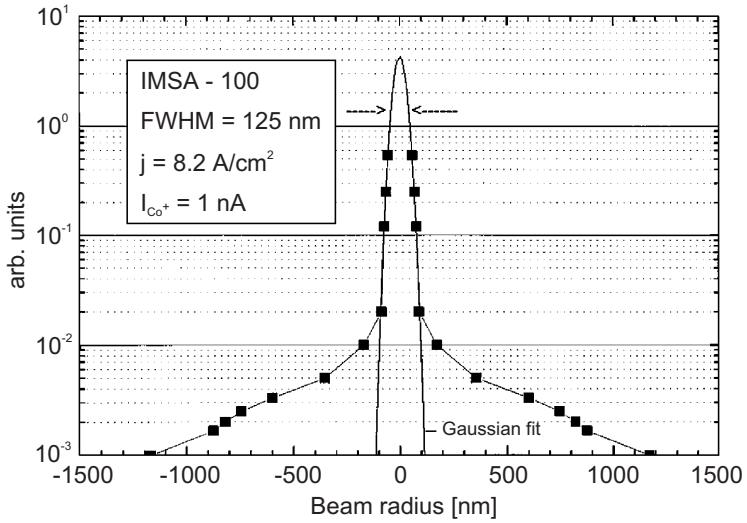

Fig. 3.3. Typical FIB beam profile exhibiting a Gaussian beam center, which is mainly responsible for sputtering, and beam wings containing approximately up to three orders of magnitude fewer ions. [reproduced from Teichert et al., 1998] For the actual structuring the spot size was slightly smaller (30 nm).

As the primary beam raster scans across the sample surface, the signal from the sputtered ions or secondary electrons is collected to form an image. This allows one to observe the modification in-situ. At low beam currents, very little material is sputtered; at higher currents, a great amount of material can be removed by sputtering, allowing precision milling of the sample down to a sub-micron scale. A typical beam profile of the ion beam used in this work is shown in Fig. 3.3.

In this work straight grooves in thin silver films were produced by focussed-ion-beam structuring using the improved IMSA system [Bischoff et al., 1994, 1998] equipped with the high-resolution ion-optical column CANION 31Mplus (Orsay Physics). The beam energy is 30 keV, Ga^+ ions from a liquid-metal source are used for structuring. The spot size of the ion beam on the sample surface is approximately 40-50 nm at a beam current of $\sim$ 20 pA.

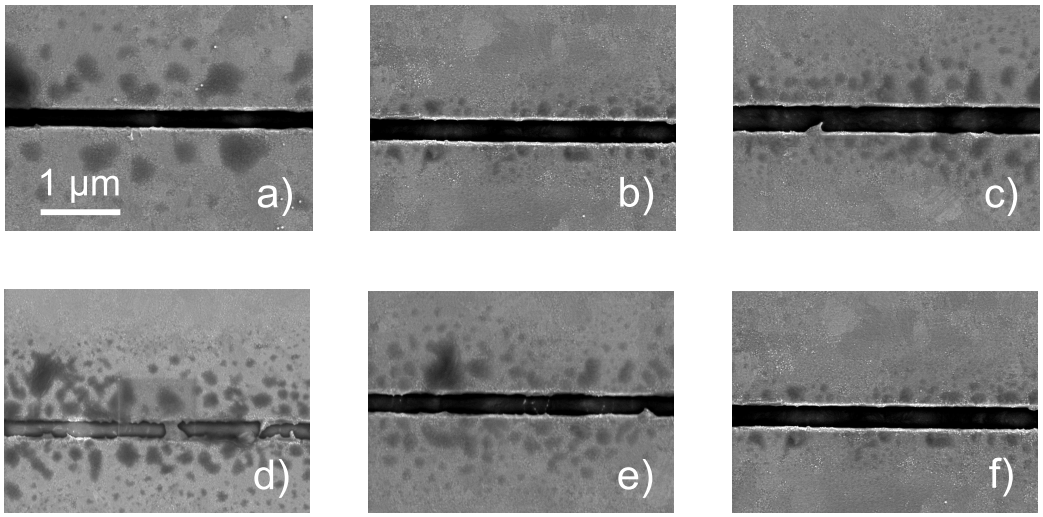

Fig. 3.4. SEM images of sputtered grooves in silver films of 60 nm thickness on a glass substrate. The spot size of the FIB was determined to be about 30 nm. The width of the grooves was adjusted with the digital pattern generator by varying the number of parallel line scans: a) 310 nm, b) 400 nm, c) 470 nm. The increment was adjusted to 15 nm, i.e. the overlapping of one pixel with the next one was 50 %. The calculated sputtering yield of silver amounts to 11.5 atoms/ion (calculated using the SRIM2003 software package) corresponding to a milling rate of 1.2 μm^3/nC. The dependance on the ion dose is shown in the lower row of images: d) 2×10^{16}cm^{-2}, e) 5×10^{16}cm^{-2}, f) 1×10^{17}cm^{-2}.

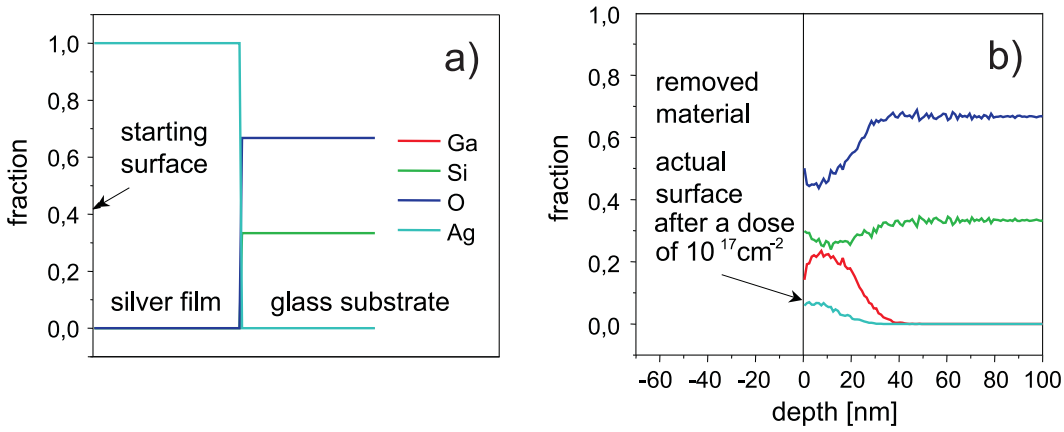

Fig. 3.5. Tridyn simulations of the ion irradiation of a 25 keV Ga FIB onto the silver film. a) shows the starting configuration of the calculation, b) depicts the actual composition of the sample close to the surface after an ion dose of 10^{17} cm^{-1}. The bottom of the groove consists of a 20 nm top layer containing a fraction of recoil-implanted Ag as well as Ga atoms from the beam.

Within the grooves the silver was removed completely down to the bare glass substrate. This was checked by writing circles and subsequent imaging of the structure by ion-generated secondary electrons. When the image contrast of the inside of the circle turns black the conductive bridge has been lost and therefore the ion dose and exposition time was high enough to remove all the metal but not the glass substrate.

Figure 3.4 shows examples of sputtered grooves. The thermal evaporation leads to polycrystalline films with grain sizes in the order of 20-50 nm. The random orientation of these grains gives rise to different sputtering yields [Wehner, 1955; Magnuson et al., 1963; Onderdelinden, 1968], i.e. straight geometric features such as the groove edge are expected to exhibit slight roughness. Additionally, small etch hillocks are sometimes present close to the groove edge. They are due to low ion doses in the beam wings that induce crystal growth. However, for the investigation of plasmon propagation the grooves can be considered fairly smooth, as shown in section 4.4.

In order to understand the sputtering and implantation processes involved simulations using the Tridyn method were performed [Möller et al., 1984, 1988]. Figure 3.5 shows results of these simulations. The ion irradiation process of a 25 keV Ga FIB onto the silver film with an ion dose of 10^{17} cm^{-2} was modelled.

As shown, the bottom of the groove consists of a 20 nm top layer containing a fraction of recoil-implanted Ag as well as Ga atoms from the beam. All samples produced were examined additionally by high-resolution imaging with a SEM for groove width determination.

3.2 Materials

3.2.1 Silver Film Preparation

Evaporation of metals onto different surfaces usually does not result in atomically flat layers. They more commonly tend to form islands, depending on the specific metal and substrate. In general, crystallographic orientation, surface reconstruction, surface termination, and deposition conditions have all been found to be important parameters for Ag film growth on crystalline materials. For amorphous substrates such as glass, silver is a material akin to strong island growth and therefore for thicker layers forms rather rough surfaces. This is especially the case for lower evaporation speeds because the atoms have enough time to arrange themselves on the surface [Krakow et al., 1994]. For film thicknesses below ∼10 nm a partially covered surface exists. Heating of the thin film leads to coagulation of smaller islands into bigger ones. The relaxation time τ to reach the equilibrium shape by surface diffusion for a cube of size 2r is [Kern, 1987]:

$$\tau = (2kT_s r^4)/(v^{4/3} D_s \sigma), \tag{3.4}$$

where k is the Boltzmann constant, v the atomic volume, T_s the temperature, σ the surface energy and D_s the diffusion coefficient. An estimate for silver is given as $\tau = 3.6$ s at 300 K and $2r = 1$ nm. This can be compared to a relaxation time of $\tau = 36000$ s at the same temperature but for $2r = 10$ nm [Wenzel et al., 1999]. Thus large islands can be avoided if additional atoms cover the surface faster than the specific relaxation time. High evaporation speeds are therefore desirable, as they are expected to lead to smoother film surfaces.

Table 3.1.
Influence of evaporation speed on surface roughness.

Nr.	evaporation speed [nm/s]	rms roughness [nm]
1	**15**	**0.6**
2	**1.5**	**0.7**
3	**0.2**	**0.9**

In order to prove this assumption, glass substrates were cleaned in Piranha solution (70:30 volume parts mixture of concentrated H_2SO_4 and H_2O_2) and ethanol. Clean substrates are of importance since surface defects or adherent particles may lead to unwanted scattering of surface plasmons [Pincemin et al., 1994]. Silver with a purity of 99.99% was purchased from Goodfellow Ltd. [Goodfellow Cambridge Limited, Huntington PE29 6WR, England, http://www.goodfellow.com]. Silver films were prepared by thermal evaporation from an annealed tungsten evaporation boat in a high-vacuum chamber (Balzers BAE 080). Different evaporation rates were chosen to investigate their influence on film surface roughness. The values in table 3.1 are obtained by analysing atomic force microscope images of the sample surfaces. For the highest controllable evaporation speed of 15 nm/s the lowest surface roughness of 0.6 nm rms was achieved.

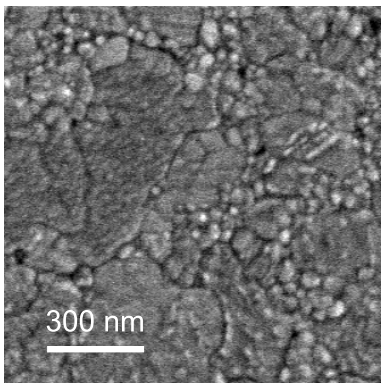

Fig. 3.6. SEM image of a thermally evaporated silver film showing its polycrystalline nature (evaporation rate $\sim$ 10 nm/s).

In all subsequent experiments silver films were prepared by thermal evaporation in high vacuum ($p < 10^{-6}$ mbar) at high evaporation rates ($\sim$ 10 nm/s), so their roughness is expected to be about 0.7 nm rms. As seen in SEM images (Figure 3.6) the thermal evaporation of silver leads to polycrystalline films mainly with grain sizes in the order of 20-50 nm.

3.2.2 SNOM Fibre Probe Preparation

Fabrication of SNOM tips is usually done either by etching or pulling of optical fibres. Both methods allow for subsequent deposition of metal, such that only a small opening at the apex is left over that defines an aperture [Paesler and Moyer, 1996]. Aluminum or aluminum/chromium layers are often used for metal coating because of small penetration depths of the electromagnetic field in the visible range ($\sim$ 7 nm for Al) and smooth layers that prevent light leakage [Betzig et al., 1991].

For pulling the fibre is punctually heated and pulled apart until it breaks [Yakobson et al., 1993; Valaskovic et al., 1995; Williamson et al., 1996; Xiao et al., 1997]. Heating temperature, pulling force, temporal force gradient and fibre alignment are critical parameters in order to achieve good results. Usually tips produced with this method have small opening angles. Because of that and also because of possible stress remaining in the pulled fibre those fibres have a typical throughput of about 10^{-6} for an aperture diameter of about 100 nm, which is quite small. Also the fibre core diameter is reduced within the tapered region. Light propagating in a coated fibre can only be supported until the diameter d is

$$d = j\frac{n\lambda}{2}, \tag{3.5}$$

with j being the mode of propagation (j = 1, 2, ...). In the final part of the tip, where d is smaller, the intensity decreases exponentially [Novotny et al., 1994]. The length of this last part of the fibre tip is also called "cut-off length" [Yakobson et al., 1995].

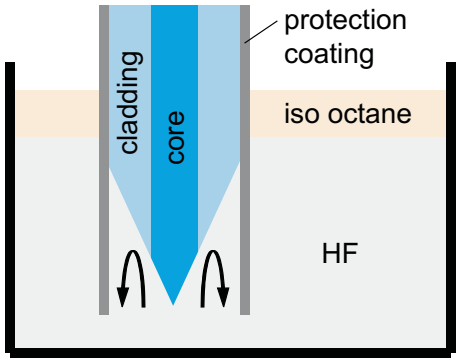

Fig. 3.7. Tube etching principle.

For etching the fibre, usually a method called "tube etching" is used [Stöckle et al., 1999], although there are other approaches as well [Hoffmann et al., 1995; Mononobe et al., 1996]. This is a method by which the fibre is etched inside its polymeric protection coating. The etching agent is hydrogen fluoride, which is covered by a lighter fluid such as paraffin, mineral oil, or octane. This is important if the hydrogen fluoride is heated for faster processing and control of the tip opening angle. Without a coating fluid layer the hydrogen fluoride would evaporate too fast. After etching the polymer protection coating is removed by etching in hot sulfuric acid in an ultrasonic bath in order to uncover the tip. Figure 3.8 shows various fibres of the same type (3M, FS-SN-3224, single mode at 632.8 nm, approx. 5 μm core diameter, 125 μm cladding diameter).

Fig. 3.8. Differences in preparing techniques for fibre probes: a) pulled fibre; b) etched fibre, 135 min in HF at 20°C; c) etched fibre, 60 min in HF at 50°C.

Here the advantage of etched fibres over pulled ones is obvious. The geometrical form is different, opening angles are usually much wider which allows for higher throughput (about 10^{-4} to 10^{-3} for 100 nm aperture). This is due to a smaller cut-off length. However, at elevated etching temperatures surfaces can get rough leading to light leakage. Additionally those fibres have good polarisation behaviour, exhibiting no favoured direction for linearly polarised light

and being able of delivering light at their aperture with polarisation contrasts of about 1:50 to 1:100. Also the damage threshold of the aperture due to high light intensities can be raised considerably if etched fibres are used [Stähelin et al., 1996]. This can be important, because temperature effects usually can't be neglected [La Rosa et al., 1995; Karaldjiev et al., 1995; Boykin et al., 1996].

In experiments for which metal-coated fibre probes are needed, the probe is coated by rotating it under a certain angle in an aluminium evaporation stage (Figure 3.9). The fiber is coated from the side by rotating it around its axis. The aperture will not be coated due to the oblique evaporation. The size of the aperture is dependant upon the angle under which the fiber is held.

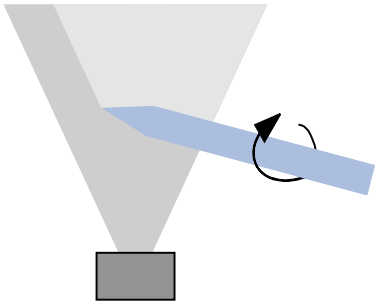

Fig. 3.9. Oblique evaporation. The fiber is rotated at a rate of $\sim 60\ \mathrm{min}^{-1}$. A small aperture at the tip apex is formed.

The opaque aluminium coating was prepared with a thickness of about 100 nm and checked optically for pin-holes in the coating that would lead to unwanted light leakage. Suitable tips were also imaged in an SEM to determine the aperture size (see Figure 3.10).

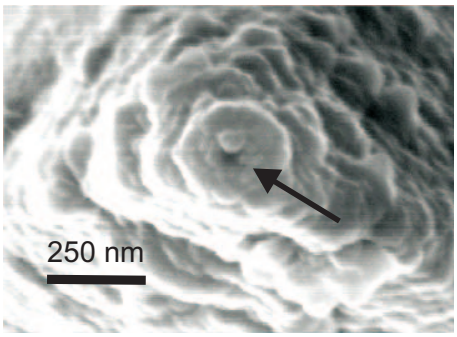

Fig. 3.10. SEM image of an etched, Al-coated fibre tip with a small aperture of approximately 60 nm at the tip apex (arrow).

3.2.3 Preparation of the dye solutions

Rhodamine 101 (8-(2-carboxyphenyl)-2,3,5,6,11,12,14,15-octahydro-1H,4H, 10H,13Hdiqui-nolizino[9,9a,1-bc:9',9a',1-hi]xanthylium perchlorate) and cresyl violet (5,9-diaminobenzo [a]phenoxazonium perchlorate) were purchased from Radiant Dyes [Radiant Dyes Laser & Accessories GmbH, Friedrichstrasse 58, D-42929 Wermelskirchen, http://www.radiant-dyes.com].

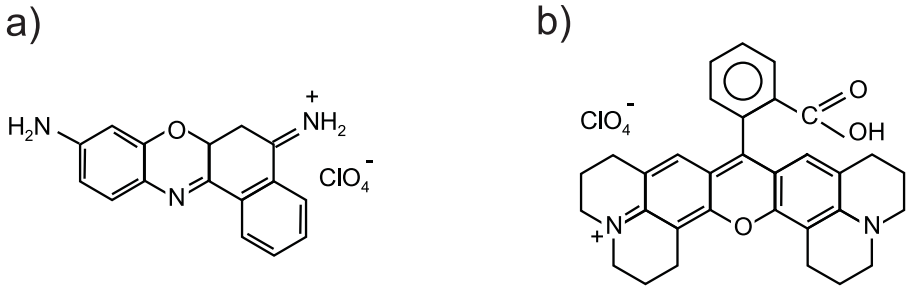

Fig. 3.11. Structure formulas of cresyl violet (a) and rhodamine 101 (b).

Solution of both rhodamine 101 and cresyl violet in ethanol (p.a.) were prepared. The solutions were gently heated to about 50°C and stirred for one hour in order to completely dissolve the dyes in ethanol.

4 Surface Plasmon Interaction with Single Grooves in Thin Silver Films

This chapter describes near-field optical measurements that investigate the interaction of surface plasmons with single grooves in thin silver films. Elastic scattering at groove edges, transmission across grooves, coupling to free-space electromagnetic waves and groove-mediated mode coupling are presented and discussed in detail.

4.1 Basic Concept

Surface plasmons (SPs) at optical frequencies propagate some tens of micrometers in thin silver films [Kroo et al., 1991; Dawson et al., 1994; Hecht et al., 1996]. This is sufficient to manipulate them on that length scale using structured surfaces [Bozhevolnyi et al., 1997]. Passive functionalities such as deflection, focusing, guiding and filtering and even nonlinear interactions of SPs are possible. SP elements may exhibit resonance features and field enhancement at the film surface, thereby offering the chance to design certain surface properties [Pendry et al., 2004]. On the other hand, a potential disadvantage is the restricted propagation length, which requires close integration of structures and perhaps an inclusion of SP amplification elements.

Today, little is known about the effect of confined structures on SP propagation. The understanding of the propagation and localization of surface

plasmons and their interaction with materials and structures is still one of the big challenges in advanced optics, and fundamental knowledge is still needed. It is therefore necessary to systematically investigate structures that can be readily implemented in a thin metal film or substrate. One possible step in this direction would be to quantitatively and locally determine SP reflectivity and transmissivity. As suitable elementary structures, single grooves in a thin metal film are investigated here. They can be prepared, for example, by means of a focused ion beam (FIB).

Single surface grooves were formerly investigated by Bouhelier et al., who used an aperture near-field probe for excitation and an immersion microscope for detection [Bouhelier et al., 1999]. In contrast, our experimental setup is based on the attenuated-total-reflection scheme, in which plasmons are excited only along one direction on the sample surface, whereas Bouhelier et al. excited plasmons in many directions by illumination through an optical fiber aperture. Thus, our setup provides a more direct access to certain properties of surface plasmons. In the following, near-field optical methods are employed in order to directly reveal properties of such travelling surface waves, such as the optical transmission across defined barriers or the coupling to free-space electromagnetic waves.

4.2 Setup

The near-field experiments reported in this work were performed with a home-built SNOM system [Schmidt, 1997; Trogisch, 1997]. Our experimental setup is based on the attenuated-total-reflection (ATR) method (see Fig. 4.1). Plasmon excitation is achieved by focusing light from a HeNe laser (632.8 nm) onto a thin metal film on a rhombic glass prism under total internal reflection. The laser light can be adjusted in intensity by a neutral filter and also in its polarization by a fibre polarisation controller (fibre paddle) being coupled to a single-mode glass fibre (3M, FS-SN-3224, single mode at 632.8 nm, approx. 5 μm core diameter, 125 μm cladding diameter). The illumination optic consists of a microscope objective for collimation, which is matched with its numerical aperture to the fiber, and an achromatic focussing lens with a focal length of 40 mm. The focus on the sample surface measures approximately $7 \times 10\ \mu m^2$

(FWHM) for an incidence angle of 42° with respect to the surface normal. The polarization is adjusted to be parallel to the plane of incidence (p polarization), as the plasmon is a primarily longitudinal oscillation with both k vector and electric field vector (polarization) pointing mainly in the same direction in the surface plane. Successful plasmon excitation manifests itself as a decrease of the reflected intensity in a narrow angular range, which can be observed on a screen as a dark line across the spot of the reflected light (see Fig. 2.3). The near-field probe acts as a local scattering center for the plasmon, thereby converting the plasmon field to a propagating electromagnetic wave travelling down the optical fibre to the detector. Only bare dielectric fibers without any metal coating were used for imaging in order to prevent plasmon field coupling to the metal coating of the fibre.

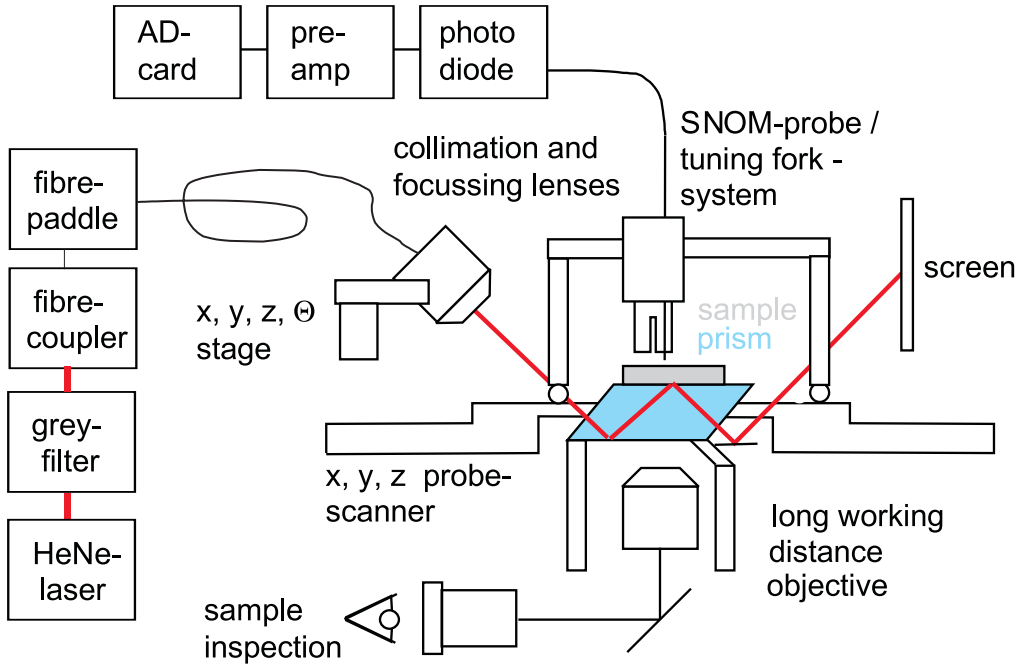

Fig. 4.1.
Experimental setup.

The probe-sample distance is controlled with a feedback mechanism based on a sensitive shear-force detection using a quartz tuning fork to which the fiber tip is glued [Karrai and Grober, 1995]. A shaker piezo excites the tuning fork at its eigenfrequency and the voltage developed between its electrodes is

measured with a lock-in amplifier. The demodulated signal directly reflects the tip vibration amplitude which is kept below 2 nm. Upon tip-sample approach the free vibration amplitude is slightly reduced due to viscous damping forces [Schmidt et al., 2000]. Using a digital feedback loop for accurate distance control the scanning near-field optical microscope (SNOM) is operated with an amplitude damping as small as 0.5 to 1.0 % below the free oscillation amplitude. Such small damping (corresponding to low interaction forces in the order of $\sim$ 100 pN [Schmidt et al., 2000]) is necessary to avoid destructive tip-sample interaction. From Fig. 4.2 it is evident that these values correspond to a probe sample distance of about 20 nm. However, this value depends to some extent on the specific ambient conditions such as temperature and humidity [Brunner et al., 1999; Wei et al., 2000; Schüttler et al., 2001], which might be different for measurements performed on different days. From experience, the above value can be considered a reasonable average.

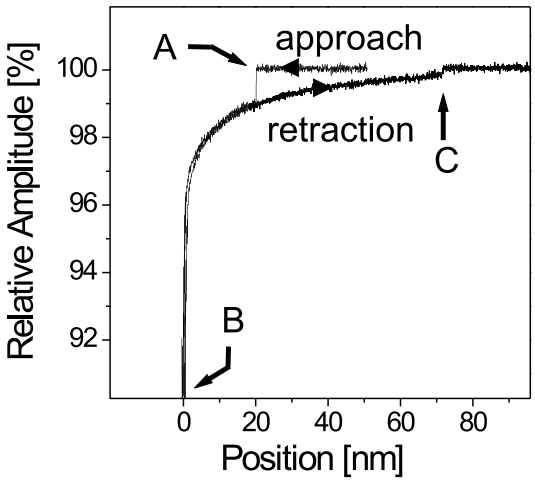

Fig. 4.2. SNOM feedback approach curve. At point A the probe tip snaps to the water film on the sample surface, which is present under ambient conditions. Further approach leads to a strong damping (point B). The snap out of the fiber tip is seen in point C when the tip is being retracted.

The SNOM is mounted onto the sample stage of an inverted optical microscope (Zeiss Axiovert 135) which can be used for visual inspection during adjustment of the exciting laser beam. Plasmon propagation is examined with a setup in which both the sample and the illumination optics used for plasmon excitation are kept in a fixed position during the measurement while the SNOM

tip is three-dimensionally scanned with the help of a $x-y$ table (PI systems) and a homebuild z stage connected to the z feedback loop mentioned above. The light signal picked up by the fibre tip is detected with a photodiode.

Images (except for the tip-retraction scans in 4.3) are acquired by scanning the fibre tip with a constant gap with respect to the substrate (constant gap mode). Bozhevolnyi et al. explored the possibility of artefacts introduced by this method when imaging surface plasmon fields. They found that the contrast observed in near-field images was purely optical, i.e., not induced by topographical variations [Bozhevolnyi, 1997], a fact that can be explained by rather strong and rapid variations of the near-field intensity in the surface plane. There are also other reasons why this method is preferable, i.e. it allows for the best spatial resolution, which would decrease with an increase of the tip-surface distance. It also helps to keep the optically imaged area connected to the surface topography (optical and topographical information are acquired simultaneously) when successive images of the same area are taken. Thereby, it accounts for possible drift of the sample with respect to the fibre tip.

4.3 Near-field Imaging of Surface Plasmons

The electromagnetic field connected with the electron charge oscillations of the plasmon have a mixed transversal and longitudinal nature. The field has its maximum in the surface plane at $z = 0$, whereas for $z \to \infty$ the field disappears, which is typical for surface waves. It can be written (k_z is imaginary)

$$E = E_0^{\pm} e^{i(k_x x \pm k_z z - \omega t)}. \tag{4.1}$$

Intrinsic absorption leads also to an exponential decay of the plasmon in the x direction. This becomes evident in near-field optical images. Figure 4.3 shows the measured near-field intensity distribution close to the surface for a plasmon excited at 632.8 nm in a 60 nm thick silver film.

The elliptic excitation spot, which is due to the oblique light incidence, is located on the left side of the image. Taking this as the starting point, an exponential decay of the detected light intensity to the right side is visible,

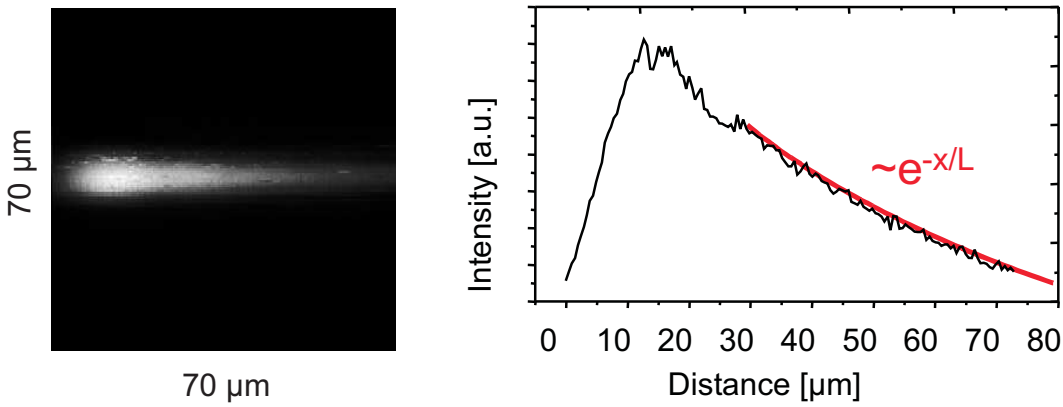

Fig. 4.3. Near-field image of an exponentially decaying plasmon on a 60 nm thick silver film at 632.8 nm excitation wavelength. In the cross section on the right side the decaying part has been fitted. The decay constant (1/e) is 25.6 m.

thus showing the decaying nature of the plasmon field. From cross sections of this image a decay length (1/e) of 25.4 μm can be deduced. This is consistent with theoretical considerations yielding the propagation length L as [Raether, 1988]

$$L = \frac{c}{\omega}\left(\frac{\epsilon'_m + \epsilon_d}{\epsilon'_m \epsilon_d}\right)^{2/3} \frac{(\epsilon'_m)^2}{\epsilon''_m}, \tag{4.2}$$

where ϵ_m and ϵ_m are the dielectric constants of the metal and the dielectric (air) respectively. For solid metal films silver has the longest propagation length, and hence the smallest losses, for plasmons excited with visible light. The introduced energy is deposited as heat in the film. This heat can be measured by a photoacoustic method [Inagaki et al., 1981].

4.3.1 Imaging Characteristics of Coated and Uncoated Fibre Probes

The key point in understanding near-field optical imaging is the influence of the probe on the optical signal being measured. Early treatments of this problem were approaches based on transfer functions [Carminati and Greffet, 1995; Vohnsen et al., 1999], but possible multiple scattering events [Courjon, 1994]

and also different illumination and detection methods lead to the conclusion that it is rather difficult to find a general solution to this problem. Nevertheless, the thorough understanding of the imaging characteristics of fibre probes and also scan modes are crucial for the interpretation of near-field optical images [Betzig et al., 1992 and 1993; Hecht et al., 1997; Kalkbrenner et al., 2000]. Bozhevolnyi studied the influence of the probe on localized plasmons (particle plasmons) and suggested that the probe-sample coupling is determined by the polarisability of the probe (i.e. probe material) [Bozhevolnyi, 1997, 1999]. Experiments by Devaux et al. showed the possibility of differentiating electric and magnetic field components in the near-field by using different metal coatings on the probe [Devaux et al., 2000].

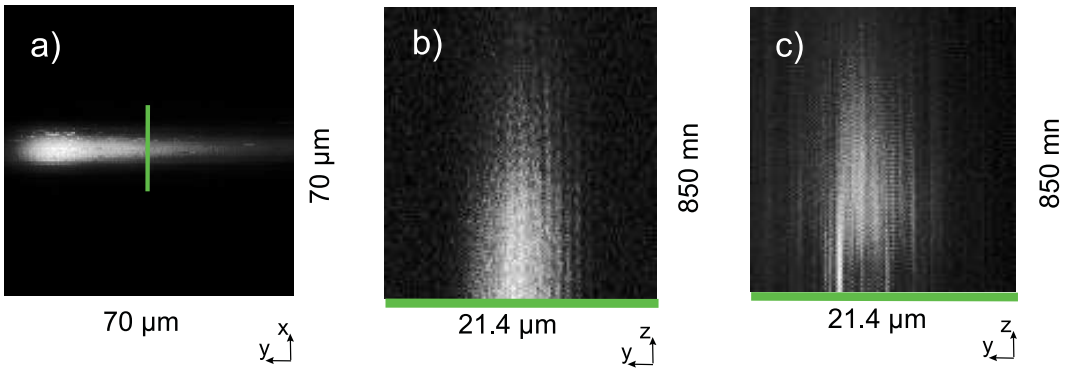

Fig. 4.4. Imaging characteristics of coated and uncoated fibre probes: a) intensity distribution in the surface plane; b) intensity distribution perpendicular to the surface plane for an uncoated purely dielectric fibre; c) intensity distribution perpendicular to the surface plane for an Al-coated fibre

In this work a first approach uses tip retraction scans ($x - z$ scans). This method is employed in order to characterize different plasmon probes and to verify the plasmon decay in the vertical direction (z axis). While the probe tip is moved along a line in the surface plane (green line in Fig. 4.4 a)) it is retracted for each discrete point on the line. For this the feedback loop is halted at each such point and a voltage ramp is added to the electrodes of the z piezo stage which accounts for lifting the probe. After this procedure the feedback loop is reengaged and the probe is moved to the next point. Results are shown in Fig. 4.4 b) and c). While uncoated dielectric fibre tips show the expected exponential decay of the plasmon field in the z direction (Fig. 4.4 b)

), aluminium-coated fibres show a rather strong disturbance of the travelling plasmon when the probe tip is close to the surface (detected intensity drop in Fig. 4.4 c)).

This clearly shows that using metal-coated fibre tips causes problems in studies of metal surfaces. The tip-surface interaction can significantly modify local electromagnetic fields. The use of metal-coated fibres in close proximity to a metal surface results in a strong perturbation. In this case, the detected signal is related to both the tip and surface, rather than to the SP field above the surface. Moreover, reflection of SP from the tip, in addition to surface defects, creates another type of artefact depending on the relative position of the SNOM tip with respect to surface features.

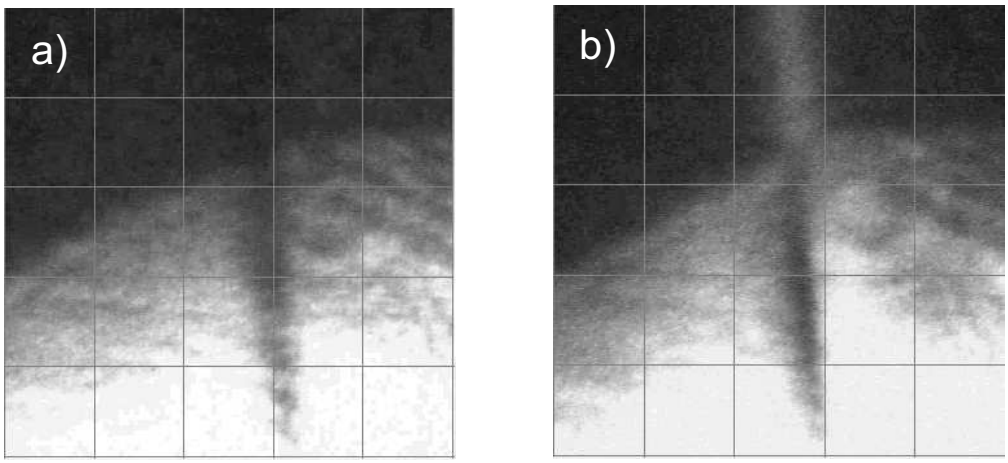

Fig. 4.5. Tip-induced broadening of the reflectance dip in the reflected light spot (only a part is shown, compare Fig. 2.3). In a) no SNOM probe is present while in b) an aluminium-coated tip dips into the propagating plasmon field on the surface. Additionally the plasmon is strongly scattered, seen as a bright band (see also Fig. 4.6).

In a second experiment the change of the angular-dependent reflection of the exciting light is observed while a metal coated-fibre probe maps the field of the propagating surface plasmon. In this method photographic images of the reflected ATR light spot projected onto a screen were taken (see Fig. 4.1).

In Fig. 4.5 b) a broadening of the SP reflection line is observed for the case that an aluminium-coated tip dips into the propagating plasmon field on

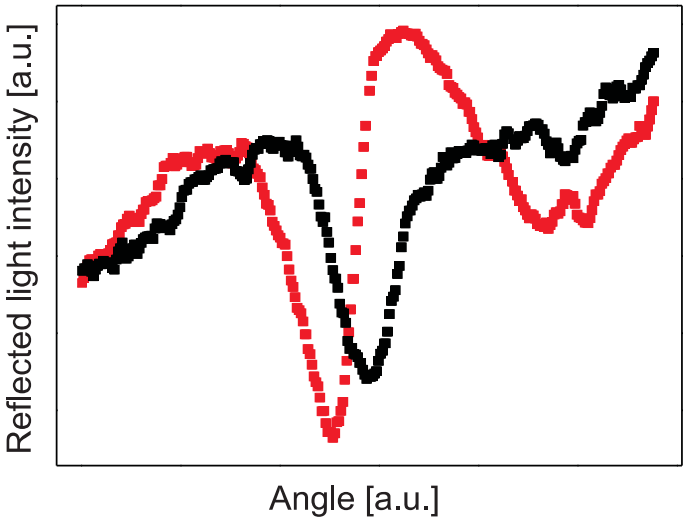

Fig. 4.6. Horizontal cross sections (taken in the middle of the image) of Fig. 4.5 a) (black line) and Fig. 4.5 b) (red line). The reflectance curves appear oblique in the cross sections because of the Gaussian beam profile of the exciting laser beam. The dip in the red curve appears broadened and is superimposed by a light signal stemming from tip-enhanced scattering.

the surface. In this case the metal-coated tip mediates coupling of otherwise not matching k values of the incident light to the plasmon. Additionally the plasmon is strongly scattered when a metal coated-tip is close by, which is seen as a bright band in Fig. 4.5 b).

In contrast, uncoated fibre tips introduce much smaller perturbations in the measured electromagnetic field. They have a relatively low refractive index and the signal detected with such a probe will be closely proportional to the near-field intensity [van Labeke et al., 1993; Carminati et al., 1995; Bozhevolnyi, 2002]. Perturbation will increase with an increase in the tip dielectric constant.

It has generally been assumed that light leakage from bare fibers, which should occur in the far-field when the fiber diameter approaches the mode-field diameter, would lead to a spatial resolution of $\sim \lambda/3$. However, this ignores the electromagnetic field coupling that occurs when a bare fibre tip is used to collect light close to a surface [Greffet et al., 1997]. The resolution of the SP mapping obtained with an uncoated fibre tip is related to the gradient of the SP evanescent field above a metal surface. The lateral resolution of SNOM mapping of the SP field with uncoated fibre tips routinely reaches about 100

nm at a detecting light wavelength of 632.8 nm [Bozhevolnyi et al., 1997]. This is significantly better than the resolution obtained with the same kind of fibre tips in reflection or transmission measurements where propagating field components are dominant, and hence no probe-sample coupling occurs.

Another aspect comes into play when the opening angle of the probe tip and the efficiency of the evanescent-field detection related to this parameter are considered. An increased detected signal caused by an increase of the tip opening angle can be observed. This has been shown to depend on the angle to the fourth power [van Labeke et al., 1993]. Discrimination of propagating light above a surface, that might be scattered from SP out of the surface plane, against the evanescent field of the excited and in-plane scattered SPs, is also more efficient with probe tips with wider opening angles. The propagating field in the dielectric contains components parallel to the surface plane, and the detected signal related to these components increases with the cone angle as the square of the tip opening angle (for small opening angles) [van Labeke et al., 1993]. In conclusion, the relative contribution of the perpendicular field components in the detected signal increases with the cone angle of tip, implying an increase in the relative efficiency of the SP-related signal collection compared to scattered light with an increase of the tip opening angle. As shown later, the fiber tips used in this work have the property to detect mainly the in-plane components (with respect to the surface) of the electric field.

4.3.2 Plasmon Scattering at Surface Grooves

Scattering and interference of surface plasmons at surface defects has been investigated theoretically [Pincemin et al., 1994; Novotny et al., 1997; Bozhevolnyi et al., 1998; Sánchez-Gil et al., 1999; Jamid et al., 1995, 1997] as well as experimentally [Hecht et al., 1996; Smolyaninov et al., 1996, 1997; Bozhevolnyi et al., 1998]. Local SP excitation has also been demonstrated by using a metal-coated tapered fiber probe as a radiation source in the work by Hecht, and by changing coupling conditions in the Kretschmann-Raether configuration by means of individual surface defects created by a probe-based direct writing technique by Smolyaninov. In the latter work, elastic SP scattering in the surface plane by an artificial surface defect was also attempted but with

poor results. More pronounced elastic scattering of SPs has been observed with structures produced by means of electron-beam lithography [Krenn et al., 1997].

From a theoretical point of view an efficient elastic scatterer should be relatively large in size and it should possess smooth boundaries. These properties give rise to a large scattering cross section while preserving an adiabatic perturbation. Other approaches based on film material modification [Smolyaninov et al., 1996, 1997] are probably less promising, as the influence of material properties on SP propagation is known to be quite strong [Agranovich, 1982]. Recently, a technique that relies on local deformation of a metal film surface employing an uncoated fiber tip has been demonstrated for fabricating elastic micro-scatterers. Several micro-optical components, e.g. micromirrors and microcavities for SPs were shown [Bozhevolnyi et al., 1997].

In the following plasmon scattering by single groove structures is investigated.

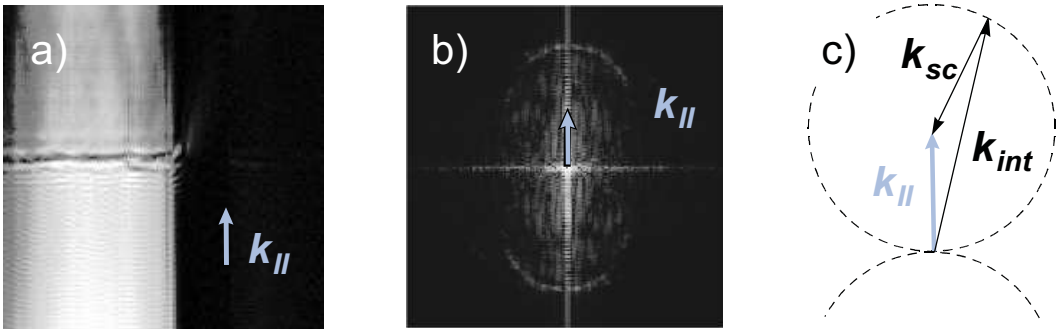

Fig. 4.7. A groove of 500 nm in width shows reflection (interference pattern) and transmission of the surface plasmon (a). The Fourier spectrum clearly shows directional scattering (back reflection) (b). Interference of incident and scattered plasmons creates a standing wave pattern characterised by k_{int} (c).

Fig. 4.7 a) shows a scanning near-field optical image of a surface plasmon incident upon a 500 nm wide groove in a silver film of 60 nm thickness. The propagation direction of the plasmon is indicated by its wave vector $k_{\parallel}$. Clearly visible are intensity fringes in the lower part of the picture which are due to interference of the incident and the reflected surface plasmon. Some of the fringes are not parallel to the groove and can be attributed to elastic

scattering of plasmons at small protrusions at the groove edge resulting in two-dimensional scattering.

This becomes more evident from inspection of the Fourier spectrum of 4.7a, presented in fig. 4.7b. Elastic scattering in different directions within the surface plane creates two circle-like structures, as schematically depicted in fig. 4.7c. The fringes in the original image are due to an interference term in the resulting intensity distribution stemming from the superposition of incident and scattered waves with wave vectors $k_{\shortparallel}$ and k_{sp}, respectively:

$$I \propto \cos(k_{\shortparallel} - k_{sp})r \tag{4.3}$$

Nevertheless, backscattering is more prominent than scattering in other directions, as indicated by a stronger contrast of the opposing ends of the circles in the Fourier spectrum. Hence the groove edge can be considered to be fairly smooth. Note that the Fourier transformation of the near-field images is a simple and powerful tool for studying such effects.

4.3.3 Plasmon Transmission Dependance on Groove Width

Samples with different groove widths were inspected for their transmission behavior. Cross sections of near-field images were used to extract transmission data after subtraction of the background signal of the detector (photodiode). The obtained values are shown in fig. 4.8. The underlaid graph was taken from a theoretical calculation by Maradudin et al. [Maradudin et al., 1983], in which the system was treated as a waveguide structure sandwiched between two metal boundaries, and the fields were represented in terms of waveguide modes. In that article discrete values for certain groove widths were calculated (black dots in fig. 4.8) and fitted by a continuous line. The general decrease of the plasmon transmission is indicated by a broken line in the same figure. Our original data have been superimposed as large solid circles.

The measured transmittance values are highest for small groove widths, as expected. For larger widths the transmittance decreases in general, however,

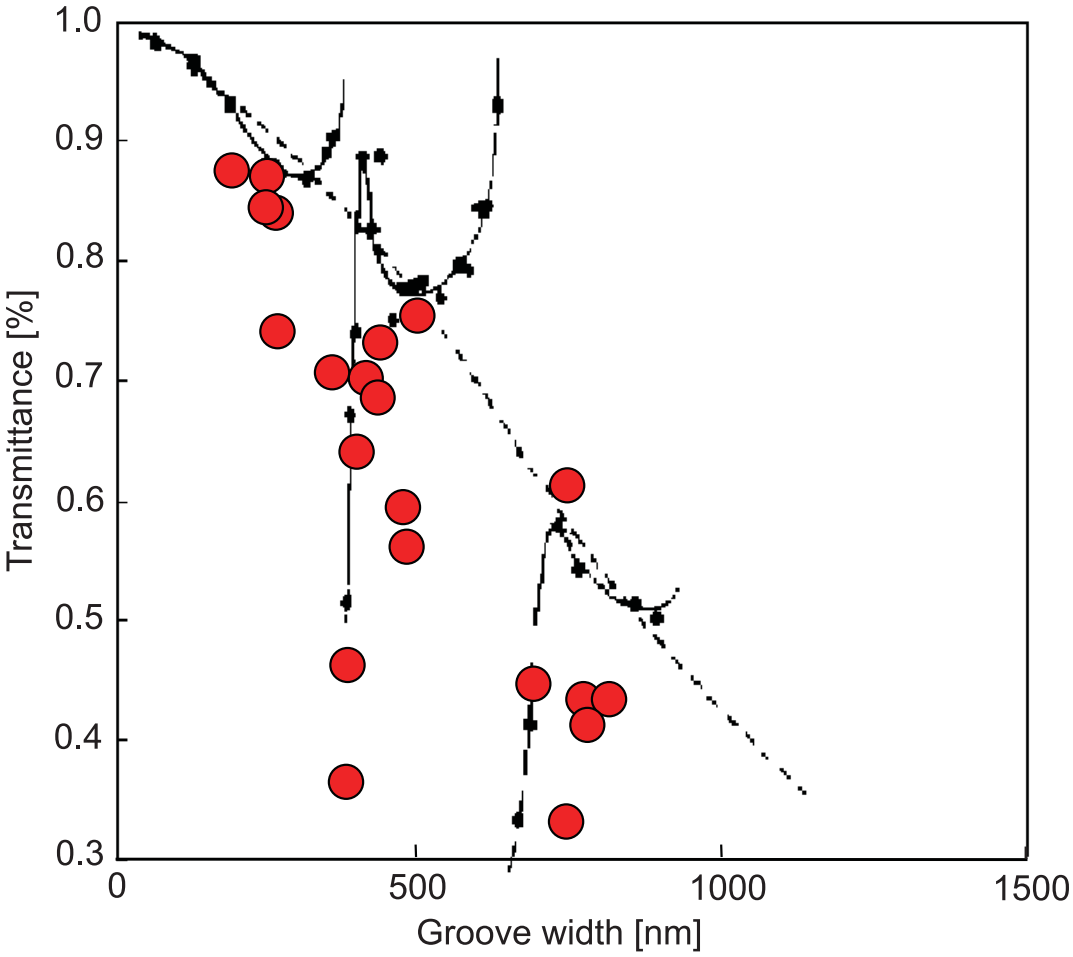

Fig. 4.8. Surface plasmon transmittance as a function of groove width. Experimental data are superimposed (large solid circles) on theoretical data produced by Maradudin et al. (black points with black fit curves; with kind permission of the author, [Maradudin et al., 1983]).

there are two pronounced local minima, one at about 370 nm and the second at about 690 nm. This non-monotonic dependence on groove width agrees with the theoretical predictions of Maradudin. An increase of the transmittance for increasing widths close to the mentioned minima, however, is not verified by the measurement.

One possible explanation was given by Maradudin. He suggests that the complex transmission behavior is due to the existence of certain favorable groove widths supporting electromagnetic modes in the gap region [Maradudin et al., 1983]. The measured values support that interpretation. One may

assume that these resonances occur near integer multiples of one half of the light wavelength, which is 316 nm in our case. Additionally, if it is assumed that the skin depth δ of electromagnetic radiation at 632.8 nm wavelength, which is given by

$$\delta = c/(2\omega\sqrt{\epsilon}), \tag{4.4}$$

that is for silver $\sim$ 13 nm, increases the effective width by two times that value [Martín-Moreno et al., 2004], the calculation yields 342 nm for the effective width. This almost represents the value of the experiment (within an errror of $\sim$10%). The gallium ions implanted by FIB sputtering would also give rise to a larger effective skin depth, because for worse conductors than silver this value is expected to increase.

A pivotal and determining factor, however, always remains, which is the accuracy of the investigated geometry. A broad range of wavevector values is expected to originate from the sharp groove edges assumed in the theoretical considerations. However this is not really true in the measurement, since the FIB structuring always leaves slightly rounded groove edges because of the beam profile. An imposed edge corrugation may, in addition, significantly alter the transmission across the groove as well. It is very well known that an incident plane wave will be reflected into diffracted orders by a periodically corrugated surface. A grating can also provide the momentum required for the incident radiation to be scattered into surface plasmon states, which has been extensively studied [Raether 1988].

One important question arises when different film thicknesses are considered. While Maradudin et al. treat the case of thick metal films, the actual sample film thickness is comparable to the plasmon skin depth, which in our case measures 25 nm [Raether 1988]. Further investigations should therefore address the influence of the film thickness on plasmon transmission behavior.

4.3.4 Coupling to Free-Space Electromagnetic Waves

The exponential decay of the surface plasmon intensity with distance from the point of excitation is interrupted by the groove. There, a sharp increase in the detected signal intensity is followed by a subsequent drop. The initial signal rise suggests that the first groove edge causes the plasmon to couple to free-space electromagnetic modes, thereby leading to partial reradiation of the plasmon energy. This interpretation is supported by the visual observation (see Fig. 4.1) of a bright line on the sample at the location where the plasmon interacts with the groove. Behind the groove the exponential decay is visible again in the near-field images. A small fraction of the incident plasmon is converted to light at the groove. This is due to edge roughness and the propagating nature of the fields in the gap region. For larger gaps the effect is more prominent than for smaller ones, which can be explained by the increased spreading of the beam in the gap. In order to investigate radiation patterns for different groove widths tip retraction scans were performed. Figure 4.9 shows the plasmon field extending into the air side of the metal air interface. There are rays extending from the surface close to the groove edges into the air, which is attributed to reradiated light at the edges. There is also a second radiated part more on the right side of the image which is broader.

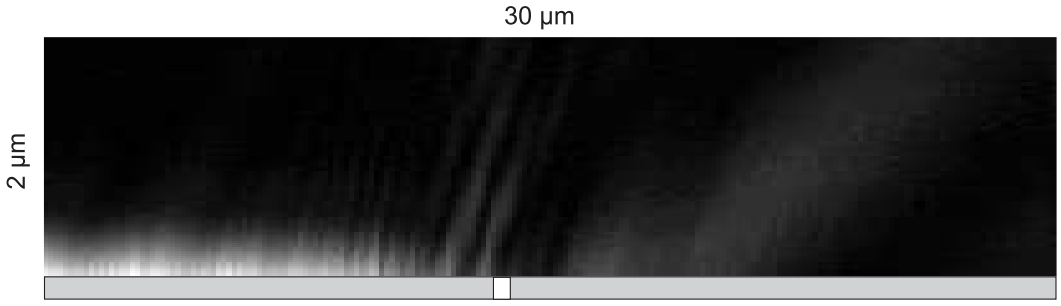

Fig. 4.9. Tip retraction scan showing the plasmon field extending into the air side of the interface. Note the reradiated light at the groove edges. The groove position is indicated. The image is not to scale because of the high aspect ratio.

4.3.5 Coupling between Surface Plasmon Modes on Metal Films

Recently, Ebbesen et al. [Ebbesen et al., 1998; Martín-Moreno et al., 2001 and 2003] and Sönnichsen et al. [Sönnichsen et al., 2000] showed that the energy of SPs excited on one side of a metal film, either by the tip of a scanning near-field optical microscope (SNOM) or via a surface grating, can be transferred to the other side and radiated there via sub-wavelength holes in the film. In the following, we show that a single groove in a silver film can couple energy from the upper SP mode to the non-radiative lower one propagating at the inner interface between the metal film and the glass substrate. The excitation of the lower mode is directly detected with a SNOM as an intensity modulation due to spatial beating between SP modes. For a quantitative analysis we use the formulas describing SPs on the surface of a metal half-space. They provide a good approximation also for films in the thickness range used in our experiment. However, the radiative damping of the upper mode has to be taken into account additionally, as well as the modification of the field of the lower mode close to the film surface where the field is probed. The image contrast can be understood quantitatively and we determine the mode coupling efficiency. We also show in a numerical simulation how the groove gives rise to such a coupling.

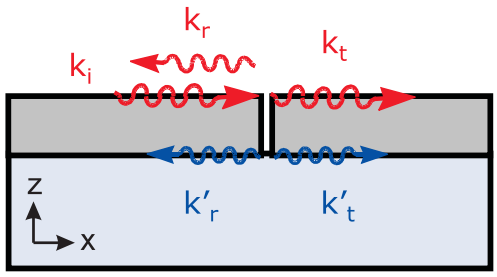

Fig. 4.10. Wave vectors of incoming (k_i), reflected (k_r, k'_r) and transmitted (k_t, k'_t) plasmon modes

The most striking features in the near-field images, obtained by scanning the tip across the surface close to the groove, are a short-wavelength standing-wave pattern in the upstream area (Fig. 4.11 a) and a similar pattern with a much larger period in the region beyond the groove (Fig. 4.11 b). The pattern in Fig. 4.11 a) is readily explained by reflection of the incident wave (k vector $k_i = k$) at the groove leading to a counter-propagating wave ($k_r = -k$). The superposition of the two waves results in a stationary spatial intensity

modulation with period

$$\Lambda_1 = 2\pi/|k_i - k_r| = \pi/k. \tag{4.5}$$

The theoretical value of k follows from the dispersion relation of the SP [Raether, 1988]:

$$k = \frac{\omega}{c}\sqrt{\frac{\epsilon_{mr}\epsilon_d}{\epsilon_{mr}+\epsilon_d}}, \tag{4.6}$$

where $\omega/(2\pi)$ denotes the frequency, ϵ_{mr} is the real part of the dielectric constant of the metal, and ϵ_d is the dielectric constant of the adjacent dielectric medium. With $\epsilon_{mr} = -17.9$ [Schröder, 1981], $\epsilon_d = 1$, and $\omega/c = 2\pi/(632.8$ nm) we obtain $k = 2\pi/(614.8$ nm). Hence, we expect a period of the standing-wave pattern of $\Lambda_1 = 307.4$ nm. For determining an accurate experimental value, every scan line of the SNOM image was Fourier transformed and the average amplitude spectrum was calculated as shown in Fig. 4.11 c). The spectrum is dominated by a narrow peak corresponding to a wavelength of 310 nm, which is very close to the theoretical expectation.

The occurrence of a standing wave after the groove (Fig. 4.11 b) might be surprising at first sight, as only a transmitted wave should exist on that side with no back-propagation. However, the groove breaks the translational invariance along the direction of plasmon propagation and therefore the k vector is no longer a preserved quantity. Hence, in the process of transmission and reflection, also the SP at the metal-glass interface may be excited. The wave number of this SP mode is $k' = 2\pi/(390$ nm) as obtained from Eq. 4.6 with $\epsilon'_d = n^2$, $n = 1.515$ being the refractive index of the glass substrate.

Consequently, two SPs, one at each interface, propagate away from the groove. The evanescent electromagnetic field of the SP at the lower interface extends across the metal film and leaks into the air space above the film, where it is superimposed on the field of the SP at the top interface. The interference of these two transmitted fields, oscillating at the same frequency but propagating with different k vectors $k_t = k$ and $k'_t = k'$, leads to the formation of the standing intensity pattern recorded by the SNOM. The modulation period is

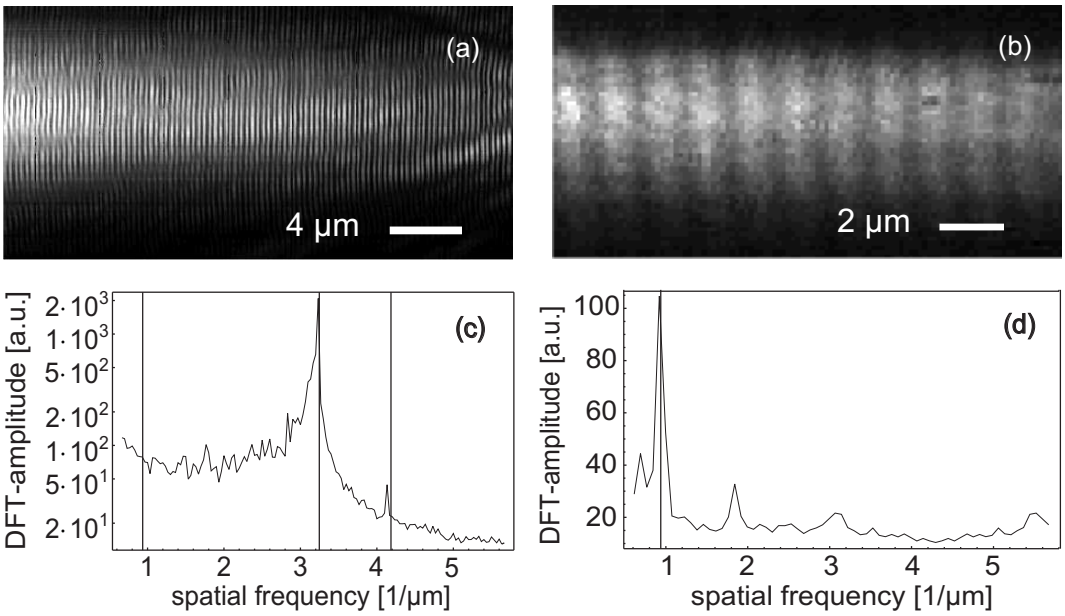

Fig. 4.11. Near-field images of the plasmon intensity before (a) and after (b) the groove. The incident plasmon propagates from left to right. The groove is situated outside the displayed areas close to the right, respectively left border. The two images were taken in different runs at different locations along the groove. (c) and (d): Fourier transforms of (a) and (b). Vertical lines indicate the calculated beating modes. Note the logarithmic ordinate in (c).

given by

$$\Lambda_2 = 2\pi/|k_t - k_t'| = 1.06\ \mu m, \tag{4.7}$$

again in agreement with the experimental value of 1.09 μm deduced from the Fourier spectrum. Note that the visibility of this standing wave after the groove varies. Thus it is not always clearly visible as seen in Fig. 4.7.

At the groove, the lower SP mode should be excited not only in the forward direction; such a wave should also emanate backwards into the upstream region. Thus, in the area imaged in Fig. 4.11a), three waves are expected to interfere with each other: the incident ($k_i = k$) and reflected ($k_r = -k$) SPs at the surface and a reflected SP ($k_r' = -k'$) at the inner interface. The existence of the third wave gives rise to two additional fringe periods beside Λ_1: $\Lambda_2 = 2\pi/|k_r - k_r'| = 1.06$ μm (identical with the period after the groove) and

$$\Lambda_3 = 2\pi/|k_i - k'_r| = 239\ nm. \tag{4.8}$$

However, only one of these two spatial frequencies appears as a clear narrow line in the experimental Fourier spectrum (Fig. 4.11c). This line, representing a period of 242 nm close to the predicted value of Λ_3, is two orders of magnitude smaller in amplitude than the peak at $1/\Lambda_1$. The missing third peak arises from beating between the two reflected SPs (i.e., the two weakest of the three fields) and may therefore easily be lost in the noise (see below).

The visibility of the beating patterns allows us to estimate quantitatively the plasmon reflection coefficient of the groove and the efficiency of the coupling between the two plasmon modes. It appears reasonable to assume that the radiation of energy from the tip into the optical fiber is mainly due to the electric-field component along the sample surface, i.e., in the direction of plasmon propagation (x axis). This assumption is supported by theory [van Labeke et al., 1993], but is still subject to some debate [Dereux et al., 2000].

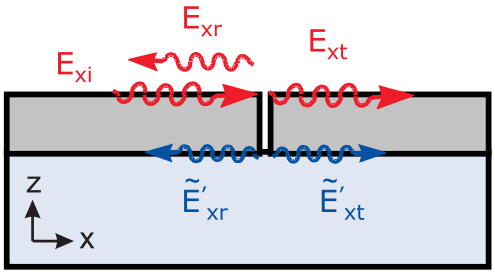

Fig. 4.12. Field components of the two plasmon modes.

Therefore, let E_{xi}, E_{xr}, and E'_{xr} be the respective field amplitudes of the incident, reflected upper, and reflected lower SPs close to the metal surface at the groove edge, situated at $x = 0$. Then, in the upstream region ($x < 0$) the x component of the total field can be written as:

$$E_x(x,t) = (E_{xi}e^{-\kappa x}e^{ikx} + E_{xr}e^{\kappa x}e^{-i(kx+\phi)} + E'_{xr}e^{\kappa' x}e^{-i(k'x+\phi')})e^{-i\omega t}, \tag{4.9}$$

where κ and κ' denote the damping constants of the two plasmon modes, and ϕ and ϕ' account for possible phase shifts upon reflection. The damping is due to internal damping in the metal (described by the imaginary part ϵ_{mi} of its dielectric constant, $\epsilon_{mi} = 0.7$ for silver at $\lambda = 632.8$ nm [Schröder, 1981]):

$$\kappa = \frac{\omega}{c}\left(\frac{\epsilon_{mr}\epsilon_d}{\epsilon_{mr}+\epsilon_d}\right)^{3/2}\frac{\epsilon_{mi}}{2\epsilon_{mr}^2}, \tag{4.10}$$

which yields $\kappa = (85\ \mu\mathrm{m})^{-1}$ and $\kappa' = (22\ \mu\mathrm{m})^{-1}$. The upper SP is additionally subject to radiative loss to the glass substrate, which gives a corrected value of $\kappa = (59\ \mu\mathrm{m})^{-1}$ for a 60 nm thick silver film [Raether, 1988]. This value is in good agreement with the intensity decay length of somewhat less than 30 μm observed in our SNOM images (see Fig. 4.3). From Eq. 4.10 the time-averaged intensity associated with E_x follows as

$$\begin{aligned} |E_x|^2 = {} & E_{xi}^2 e^{-2\kappa x} + E_{xr}^2 e^{2\kappa x} + E_{xr}'^2 e^{2\kappa' x} \\ & + 2E_{xi}E_{xr}\cos(2kx+\phi) \\ & + 2E_{xr}E_{xr}' e^{(\kappa'+\kappa)x}\cos((k'-k)x+\phi'-\phi) \\ & + 2E_{xi}E_{xr}' e^{(\kappa'-\kappa)x}\cos((k'+k)x+\phi'). \end{aligned} \tag{4.11}$$

The average intensities are given by the first three terms, followed by the three beating signals with wave numbers $2k$, $k'-k$, and $k'+k$ corresponding to the periods Λ_1, Λ_2, and Λ_3 defined earlier. The amplitude of the dominating modulation at $2k$ is independent of x (as indeed confirmed by the experiment), whereas the other two modulations decay away from the groove with different decay constants $\kappa' + \kappa = (16\ \mu\mathrm{m})^{-1}$ and $\kappa' - \kappa = (35\ \mu\mathrm{m})^{-1}$.

The visibility

$$v = 2E_{xi}E_{xr}/(E_{xi}^2 + E_{xr}^2 + E_{xr}'^2) \tag{4.12}$$

of the dominant interference pattern close to the groove ($x \simeq 0$) can be determined directly from single line scans taken from the SNOM image and is found to be roughly $v = 0.8$. With $E_{xr}'^2 \ll E_{xi}^2$ it follows that $E_{xr} = 0.5E_{xi}$, which means that 25% of the intensity is reflected in the upper mode in the present case.

From the Fourier spectrum in Fig. 4.11 c) we deduce that the intensity pattern at $k' + k$ (Λ_3) is weaker by a factor of ~ 100, hence $E_{xr}' = 0.01E_{xr}$ according to Eq. 4.11. The field of the lower mode at the inner interface

is connected with the field at the surface mainly by an exponential factor determined by the decay constant

$$\alpha'_m = (k'^2 - \epsilon_{mr}(\omega/c)^2)^{1/2} \tag{4.13}$$

of the evanescent field in the metal. For a film thickness $d = 60$ nm we obtain a factor $\exp(-\alpha'_m d) = 1/15$. However, the field is modified by the presence of the metal-air interface, and this causes a deviation by a factor

$$\beta' = 2\epsilon_{mr}\alpha'_d/(\epsilon_{mr}\alpha'_d + \epsilon_d\alpha'_m), \tag{4.14}$$

where α'_d is the transverse decay constant of the lower mode in the upper dielectric, which is obtained from the same formula as α'_m with ϵ_{mr} replaced by $\epsilon_d = 1$. Here $\beta' = 2.5$, so that the field at the inner interface is $\widetilde{E}'_{xr} = 6E'_{xr} = 0.03E_{xi}$. By integration of the Poynting vector of a weakly damped SP with field amplitude E_x, bound to the interface between two media with dielectric constants ϵ_d and ϵ_{mr}, one can easily show that the total energy flux along the direction of propagation F_{tot} satisfies

$$F_{tot} \propto E_x^2(\epsilon_d + \epsilon_{mr})^2(\epsilon_d - \epsilon_{mr})/(-\epsilon_{mr}\epsilon_d)^{3/2}. \tag{4.15}$$

With this, the factor of 0.03 in the field transforms to 2.4×10^{-4} in the energy flux, which means that only a very small fraction of the power is transferred to the lower reflected mode.

Due to $E_{xr} = 0.5E_{xi}$, the contribution at $k' - k$ should be weaker than the pattern at $k' + k$ by a factor of two. Furthermore, the stronger damping of this signal leads to a broadening of the spectral line at the expense of a reduced peak height. This and the fact that the noise level is relatively high in the interesting wave number region (probably due to diffuse scattering of the incident wave at irregularities of the groove edge) explains why we did not succeed to resolve this line. However, this beating mode, produced by upper and lower SPs propagating in the same direction, can be studied in detail after the groove, where it is clearly resolved (Fig. 4.11 b). A calculation for this region in the same spirit as above yields:

$$|E_x|^2 = E_{xt}^2 e^{-2\kappa x} + E_{xt}'^2 e^{-2\kappa' x} + 2E_{xt}E_{xt}' e^{-(\kappa'+\kappa)x} \cos\left((k'-k)x + \theta\right), \quad (4.16)$$

where E_{xt} and E_{xt}' are the respective field amplitudes of the two waves and θ is their mutual phase shift. A closer analysis of the image displayed in Fig. 4.11 b) clearly shows that the fringe pattern decays faster than the average intensity, in good quantitative agreement with the predicted decay lengths of 16 μm and 30 μm, respectively. The visibility of the interference pattern close to the groove is $v \simeq 0.3$, which yields $E_{xt}' \simeq 0.15 E_{xt}$. Thus, the field at the inner interface $\widetilde{E}_{xt}' = 6E_{xt}' = 0.9E_{xt}$ is almost as strong as the field at the surface. In terms of energy flux the ratio is 0.21. From a comparison of the intensities before and after the groove at the given location, we estimate that 55% of the incident power was transmitted across the groove to the upper mode. Hence, $0.21 \times 55\% = 12\%$ were coupled to the lower mode, indicating a rather efficient excitation. However, the efficiency seems to depend in a sensitive way on the detailed structure of the groove edges. When the plasmon excitation is moved to a different place along the groove, the visibility of the various interference patterns exhibits clear variations. Note that for display in Fig. 4.11 we chose images taken at different locations, showing the clearest patterns.

4.3.6 Numerical Model and Simulations

To gain more insight into the mode coupling introduced by the groove we performed model calculations using the Finite-Difference Time-Domain (FDTD) method, which allows both temporal and permanent responses to be studied [Taflove, 2000]. This method, that is rigorous, is more adapted for the study of a deep groove than the Rayleigh perturbative one used in [Baida et al., 1999]. In order to account for the generation and propagation of the SP, we need to consider a large spatial domain of computation. The stability criteria stipulate that the spatial step width should be less than $\Delta^{limit} = \lambda/20$.

However, in the present case, a finer mesh is needed to describe the metal layer and the groove correctly. In order to achieve a good representation of geometrical details on the nanometre scale while at the same time keeping the

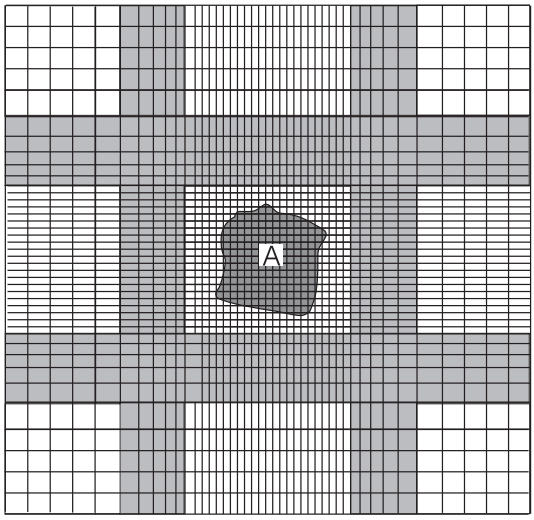

Fig. 4.13. Variable FDTD mesh.

number of nodes within a reasonable limit we developed a new FDTD code allowing a nonuniform discretisation of the structure [Taflove, 2000]. The spatial meshing step is set to 5 nm for fine geometrical features and to 30 nm in other areas. To avoid large local errors (virtual reflections) due to an abrupt change of the step width between two domains, they must be separated by an intermediate domain where the spatial step varies slowly between the fine and the coarse mesh (see Fig. 4.13). Thus, the domain is meshed with only 4.2×10^5 nodes instead of 4×10^8 nodes, which would be necessary for a regular discretisation. In addition, Perfectly-Matched-Layer (PML) absorbing conditions (adapted to the nonuniform mesh) were used in order to cancel parasitic reflections at the boundaries of the FDTD window of computation [Berenger et al., 1994].

In the calculation, the thickness and optical constants of the silver film, the parameters of the exciting laser beam, and the groove width were set to the values specified above. The angle of incidence (42.81°) was chosen to give the most efficient SP excitation.

Figure 4.14 a) shows the time-averaged intensity distribution of the electromagnetic field for the whole FDTD lattice. In Fig. 4.14 b) a cross section taken 5 nm above the metal film across the slit is displayed, which is expected to reflect rather closely the experimentally measured quantity. The characteristic features observed experimentally are well reproduced: The reflection of the SP at the slit induces a fringe pattern with a period of 304 nm. In the

downstream region a long-period standing-wave pattern is clearly visible with a period of 1.08 μm. The role of the lower SP mode becomes evident upon inspection of the intensity close to the lower interface (Fig. 4.14 c), which is not accessible experimentally. Here, in the downstream region the long-period pattern exhibits an increased visibility, while in the upstream region the pattern is now dominated by a modulation period of 240 nm, produced by the interference of the lower reflected mode with the incident upper one. A quantitative comparison with the experiment with respect to the coupling efficiency is again critically dependant on the groove quality, as the experiment clearly indicates a strong dependence on geometrical details.

Nonetheless, the above considerations show that a straight groove in a metal film causes the two plasmon modes at the two film boundaries to exchange energy and that this coupling can be rather pronounced. SNOM provides a unique tool for studying this phenomenon by analyzing the standing-

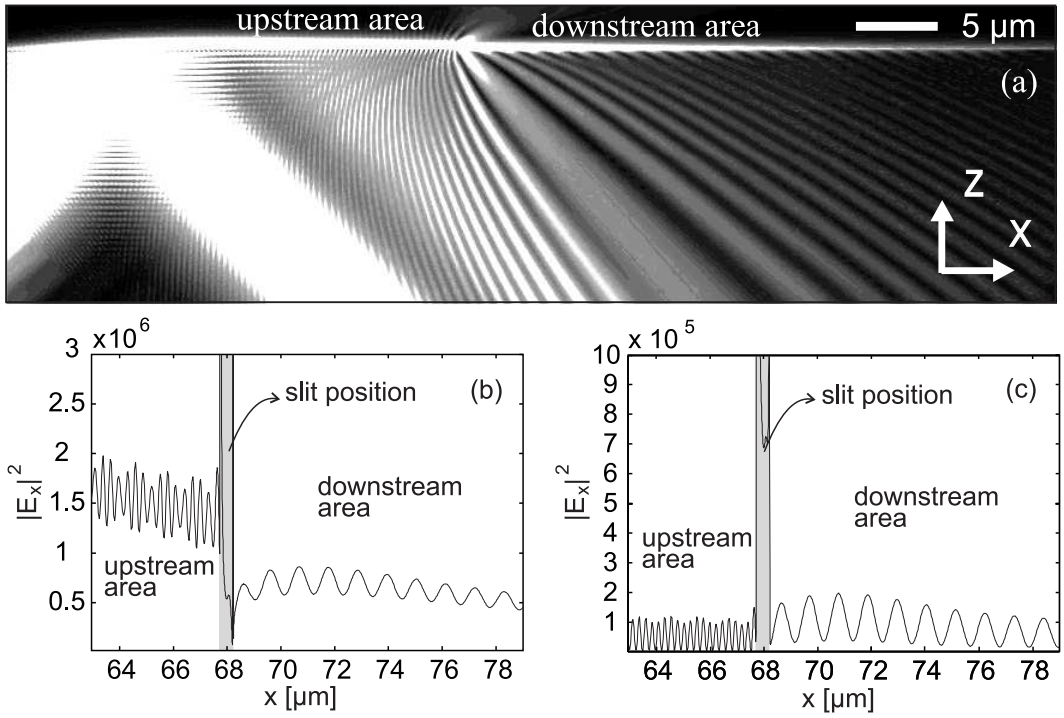

Fig. 4.14. (a): FDTD-calculated intensity distribution in the plane of incidence of the exciting laser beam in logarithmic gray scale; (b) and (c): cross sections in the region of a 490-nm-wide groove, 5 nm above (air) and below (glass) the metal, respectively (courtesy of Fadi Baida).

wave patterns created by the interfering plasmon modes, which allows for deduction of the coupling efficiency. The detailed theoretical modelling based on the FDTD method offers the prospect of gaining an improved understanding of the coupling process and its dependence on various parameters, especially the exact geometrical dimensions of the groove. If one thinks of possible applications, plasmon mode coupling may become an important building block in plasmon-based nano-optical signal processing.

5 Stimulated Emission of Surface Plasmons

In this chapter, amplification of SPs by stimulated emission at the interface between a silver film and an optically pumped dye solution is demonstrated. Here, organic dye molecules act as the amplifying medium. For that, a novel twin-attenuated-total-reflection setup is introduced. Clear evidence of the process is provided by an excellent agreement of the experimental observations with a theoretical analysis.

5.1 Basic Concept

Surface plasmons are of interest not only for functional photonic elements, they may also be used for field amplification when excited at metallic nanoparticles or roughness features of metallic microparticles, where they are greatly enhanced due to resonances [Shalaev et al., 1987]. These local fields exhibit large spatial fluctuations and energy concentration in nanosize volumes, leading to a strong enhancement of optical responses. They can be strong enough to allow, for example, the observation of Raman scattering from a single molecule attached to a metal particle [Kneipp et al., 1997; Nie et al., 1997], or the demonstration of non-linear processes such as near-field fluorescence microscopy based on two-photon excitation [Sánchez et al., 1999].

The phenomena and applications mentioned above are based on the excitation of local fields in a nanostructure by a resonant external optical field. Drawbacks are in particular that only a very small fraction of the excitation

field energy can be concentrated in the local field of the nanoparticle. It is also difficult to select a single eigenmode for excitation [Bergman et al., 2003]. Also, there can exist a large number of dark eigenmodes that have desirable localization properties but cannot be excited by an external wave [Stockman et al., 2001]. For plasmonic signal processing in functional metallic nanostructures the strong damping of the plasmon fields due to dissipation and radiation damping is obstructive. Amplification of plasmons analogous to photon amplification in a laser would be a solution to this problem. Recently, Bergman and Stockman suggested in a theoretical work such a device which they dubbed SPASER ("Surface Plasmon Amplification by Stimulated Emission of Radiation") [Bergman and Stockman, 2003]. In such a device a metal structure supporting a surface plasmon resonance acts as the resonator and, provided that gain can be introduced in the system, a self-sustained oscillation is expected to arise. Several unanswered questions remain, as to what an efficient pumping method and material would be and what kind of high quality resonator on the nanoscale would be used for plasmon amplification.

As a first step toward the realization of the SPASER, stimulated emission of surface plasmons at the interface between a flat continuous silver film and a liquid containing dye molecules is investigated. Optical pumping creates a population inversion in the dye molecules, which then act to deliver energy to the plasmon field by stimulated emission.

In the following an experiment using a twin-attenuated-total-reflection setup for observing stimulated emission of SPs is presented (see Fig. 5.1). In this arrangement a thin metal film is attached to a glass prism. The SP at the outer metal surface is excited if p-polarized light is incident from the glass side at a specific angle for which the projection of the k vector of the photon matches the k vector of the SP. At this angle, the reflectance as a function of incidence angle exhibits a dip whose width and depth depend on the degree of damping that the SP experiences. A reduction of the damping caused by the presence of an amplifying medium at the film surface will therefore result in a characteristic modification of the reflectance curve. This is the basic idea of the experiment, in which the silver film is bounded by a dye solution.

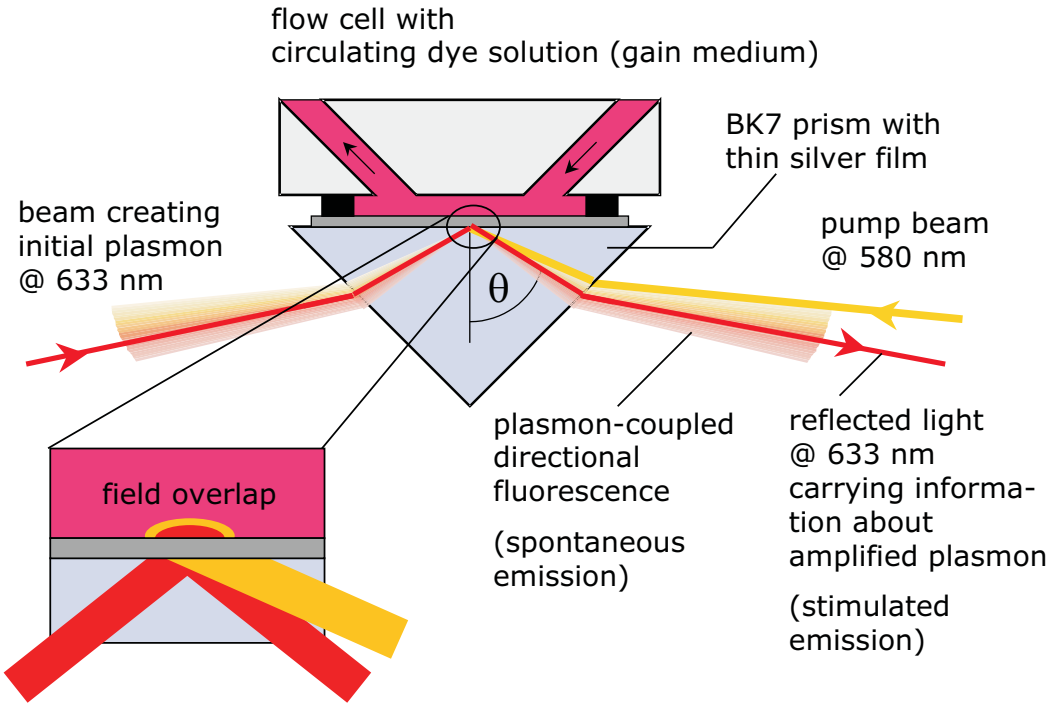

Fig. 5.1. SPASER concept. Twin attenuated-total-reflection method for SP amplification. Dye molecules, which are optically excited by the pump plasmon field, are made to coherently deliver their energy to the probe plasmon field by stimulated emission, thereby producing amplification. The signature of this process can be found in the reflected probe beam (see text). The spontaneous decay channel causes directional plasmon-coupled light emission visible as a light cone containing all colours of the dye emission spectrum.

5.2 Modelling the Lineshape

5.2.1 Intrinsic Damping and Gain

Let us first estimate how much the intrinsic damping of the plasmon could be reduced by this process. We treat the dye as a four-level system (see Fig. 5.2):

Optical excitation from the ground state 0 to the excited state 1 is followed within picoseconds by relaxation to level 2. From there the molecule returns to the ground state via an optical transition to level 3 and subsequent fast relaxation to level 0. Optically pumping transition 0-1 transfers population to level 2, while level 3 remains essentially empty due to fast relaxation. Hence,

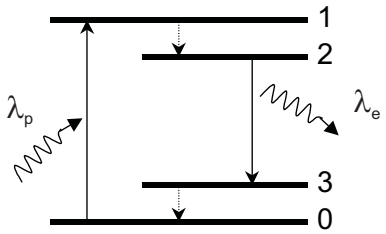

Fig. 5.2. 4-level system describing the the organic dye molecules.

transition 3-2 is characterized by population inversion and provides gain at its transition frequency. At this frequency, the dye solution acquires an imaginary part of the dielectric constant given by

$$\varepsilon_d'' = \frac{n\lambda_e}{2\pi}(N_3 - N_2)\sigma_e, \tag{5.1}$$

where n is the refractive index of the solvent, λ_e the emission wavelength in vacuum, σ_e the emission cross section of the dye, and $N_3 \approx 0$ and N_2 denote the number density of molecules in states 3 and 2 in the solution. Population inversion ($N_3 < N_2$) makes ε_d'' negative, indicating gain rather than absorption.

Now consider a plasmon at the frequency corresponding to λ_e, propagating along the interface between the dye solution and a metal half-space. The intrinsic damping caused by dissipation in the metal leads to an exponential decay $e^{-\gamma_m x}$ of the plasmon intensity along the propagation direction with

$$\gamma_m = \frac{2\pi}{\lambda_e}\frac{\varepsilon_m''}{(\varepsilon_m')^2}\left(\frac{\varepsilon_m'\varepsilon_d'}{\varepsilon_m' + \varepsilon_d'}\right)^{3/2}, \tag{5.2}$$

where ε_m' and ε_m'' denote the real and imaginary part, respectively, of the dielectric constant of the metal, while ε_d' is the real part of the dielectric constant of the solution, which is approximately given by the refractive index of the solvent: $\varepsilon_d' \approx n^2$. If we assume λ_e=632.8 nm and take ethanol as the solvent (n=1.36) and silver as the metal (ε_m'=−18, ε_m''=0.7) [Schröder, 1981] we obtain $\gamma_m = 6.3\times10^4$ m^{-1}. The gain provided by the dye solution reduces this damping by an amount of γ_d following from

$$\gamma_d = \frac{2\pi}{\lambda_e} \frac{\varepsilon_d''}{(\varepsilon_d')^2} \left(\frac{\varepsilon_d' \varepsilon_m'}{\varepsilon_d' + \varepsilon_m'} \right)^{3/2}, \tag{5.3}$$

At best we could transfer all dye molecules to the upper level 2, so that N_2 equals the total concentration N of the dye solution. Typical number densities as used in dye lasers come close to N=10^{18} cm^{-3}, while emission cross sections at the maximum of the fluorescence spectrum lie around σ_e=3×10^{-16} cm^2. These numbers yield ε_d''=-4×10^{-3} and a gain coefficient γ_d=-3.4×10^4 m^{-1}.

Hence, only under the extreme condition of most intense optical pumping is the gain of the same order of magnitude as the intrinsic losses. As shown later, this causes actual problems with the experimental setup. This clearly shows that the realization of the SPASER will crucially depend on finding the most efficient gain medium and designing low-loss metal structures that can function as resonators.

5.2.2 Thermal Effects

By illuminating the sample with intense pump light of several tens of milliwatts the sample is locally heated. Since the plasmon excitation critically depends on the dielectric properties of the involved materials, influences of temperature changes cannot be neglected. In fact, they are so strong for small modulation frequencies that the signal from stimulated emission of plasmons is completely hidden. The heating produced by the power-modulated pump beam gives rise to a periodic variation of the optical constants of the heated materials. Because of the large volumetric thermal expansion of ethanol, mainly the refractive index of the dye solution is modulated. This effect makes the reflectance dip oscillate in its angular position, which produces a pronounced background signal. Therefore a thorough understanding of the thermal effect is vital.

A useful approach to the modelling of this effect considers the temperature distribution in a three-layer geometry, which has been treated before [Jackson et al., 1981]. This theory is then modified to include more than one absorbing layer.

In the geometry in Fig. 5.3 region 0 and 1 (i.e. dye solution and silver film, respectively) are optically absorbing media while region 2 (i.e. the glass prism)

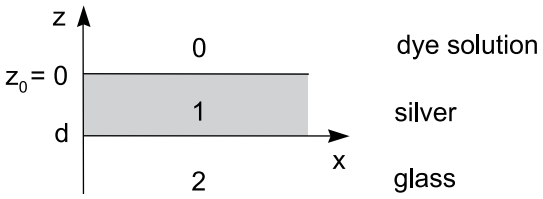

Fig. 5.3. Calculation geometry for the temperature distribution in a three-layer geometry with two absorbing layers.

is assumed non-absorbing. In these regions the temperature T is described by the following equations

$$\nabla^2 T_0 - \frac{1}{\xi_0}\frac{\partial T_0}{\partial t} = \frac{-Q_0(\overrightarrow{r})e^{i\omega t}}{\kappa_0} \tag{5.4}$$

$$\nabla^2 T_1 - \frac{1}{\xi_1}\frac{\partial T_1}{\partial t} = \frac{-Q_1(\overrightarrow{r})e^{i\omega t}}{\kappa_1} \tag{5.5}$$

$$\nabla^2 T_2 - \frac{1}{\xi_2}\frac{\partial T_2}{\partial t} = 0 \tag{5.6}$$

where κ_i is the thermal conductivity and ξ_i is the thermal diffusivity ($\xi_i = \kappa_i/\rho_i c_i$, ρ_i density, c_i specific heat capacity). Q_i describes the heat deposited per unit volume at the frequency ω in the respective absorbing media. The following boundary conditions apply

$$T_0|_{z=0} = T_1|_{z=0}\,, \quad T_1|_{z=d} = T_2|_{z=d} \tag{5.7}$$

and

$$\kappa_0 \frac{\partial T_0}{\partial z}\bigg|_{z=0} = \kappa_1 \frac{\partial T_1}{\partial z}\bigg|_{z=0}, \quad \kappa_1 \frac{\partial T_1}{\partial z}\bigg|_{z=d} = \kappa_1 \frac{\partial T_1}{\partial z}\bigg|_{z=d} \tag{5.8}$$

For the dye solution, Q_0 is given by

$$Q_0 \;=\; \frac{1}{2}\omega\varepsilon_d''\varepsilon_0|E_d|^2 e^{-\alpha_0 z} \tag{5.9}$$

$$= \frac{1}{2}\omega\varepsilon_d''\varepsilon_0|E_0|^2 V e^{-\alpha_0 z} \tag{5.10}$$

where $|E_0|^2$ is the incident pump light power, α_0 the transverse plasmon decay length in the dye solution (now in terms of $|E|^2$, as opposed to 4.14), and V the field enhancement. E_d denotes the plasmon field at $z = 0$ in the dye solution.

The intensity of the incoming beam can be written

$$I = \frac{2P}{\pi a^2} e^{-2\frac{r^2\cos\phi}{a^2}} \tag{5.11}$$

$$= \frac{1}{2}\varepsilon_0\tilde{n}c|E_0|^2 \tag{5.12}$$

where $\tilde{n}$ is the refractive index of the prism and a is the effective beam radius $(1/e^2)$ of the Gaussian pump beam (the actual beam on the interface is elliptical because of the oblique incidence, hence we use the approximation of a circular distribution that yields the same integral). ϕ is the angle of incidence and $r = (x^2 + y^2)^{1/2}$.

This yields

$$Q_0 = \frac{2P}{\pi a^2} e^{-2\frac{r^2 cos\phi}{a^2}} \frac{2\pi}{\tilde{n}\lambda}\varepsilon_d'' V e^{-\alpha_0 z} \tag{5.13}$$

For the metal film one can write

$$Q_1 = \frac{1}{2}\omega\varepsilon_d''\varepsilon_0|E_m|^2 e^{\alpha_1 z}. \tag{5.14}$$

Here, E_m is the plasmon field at $z = 0$ in the metal. Note, that the assumed exponential decay is not entirely correct for a metal film. The presence of the second interface slightly alters the field close to that interface, however, this is neglected here. Using

$$|E_m|^2 = |E_d|^2 \left(-\frac{\varepsilon_d'}{\varepsilon_m'}\right) \tag{5.15}$$

then finally yields

$$Q_1 = \frac{2P}{\pi a^2} e^{-2\frac{r^2 cos\phi}{a^2}} \frac{2\pi}{\tilde{n}\lambda} \left(-\frac{\varepsilon_d'}{\varepsilon_m'} \right) \varepsilon_m'' V e^{\alpha_1 z} \tag{5.16}$$

The field enhancement can be approximately expressed as

$$V = \tilde{n} \ \cos\phi \cdot S \tag{5.17}$$

with

$$S = \frac{2(1 - R_{min}) \left(\frac{-\varepsilon_d'^{\,2}}{\varepsilon_d' + \varepsilon_m'} \right)^{1/2}}{\varepsilon_d'' + \varepsilon_m'' \frac{\varepsilon_d'^{\,2}}{\varepsilon_m'^{\,2}}} \tag{5.18}$$

where R_{min} is the minimum value of R in the angular reflectance curve, which can be calculated using the formulas described in 2.1.5. Separation of the z dependance of Q_i followed by a Fourier transform with respect to x and y yields

$$\tilde{Q}_0 = P \ S \ \frac{\varepsilon_d''}{\lambda} e^{-\frac{k^2 a^2}{8 \cos\phi}} \tag{5.19}$$

and

$$\tilde{Q}_1 = P \ S \ \frac{\varepsilon_m''}{\lambda} \left(-\frac{\varepsilon_d'}{\varepsilon_m'} \right) e^{-\frac{k^2 a^2}{8 \cos\phi}} \tag{5.20}$$

The actual temperature change at the focus center ($r = 0$) of the pump light spot at the metal-fluid interface is then given by

$$\delta T(z) = \int_0^\infty dk \ k \ \tilde{T}(k, z) J_0(0), \tag{5.21}$$

J_0 being the zero-order Bessel function and

$$\tilde{T} = \Gamma_0 e^{-\alpha_0 z} + (\Gamma_1 - \Gamma_0 + A + B) e^{-\beta_0 z} \quad \text{for} \quad z > 0 \tag{5.22}$$

$$\Gamma_i = \frac{\tilde{Q}_i}{\kappa_i} \frac{1}{\beta_i^2 - \alpha_i^2} \tag{5.23}$$

$$A = -\frac{1}{H}\Big[((1-g)(b-r_1)e^{-(\alpha_1+\beta_1)d} + (g+r_1)(1+b))\Gamma_1 \\ -g(r_0-1)(1+b)\Gamma_0\Big] \tag{5.24}$$

$$B = -\frac{1}{H}\Big[((1+g)(b-r_1)e^{-(\alpha_1+\beta_1)d} + (g+r_1)(1-b)e^{-2\beta_1 d})\Gamma_1 \\ -g(r_0-1)(1-b)e^{-2\beta_1 d}\Gamma_0\Big] \tag{5.25}$$

$$H = (1+g)(1+b) - (1-g)(1-b)e^{-2\beta_1 d} \tag{5.26}$$

where

$$g = \frac{\kappa_0\beta_0}{\kappa_1\beta_1}, \quad b = \frac{\kappa_2\beta_2}{\kappa_1\beta_1}, \quad r_i = \frac{\alpha_i}{\beta_i} \tag{5.27}$$

and

$$\alpha_i = \frac{4\pi}{\lambda}\sqrt{\frac{-\varepsilon_i'^{\,2}}{\varepsilon_0' + \varepsilon_1'}} \tag{5.28}$$

$$\beta_j = \sqrt{k^2 + \frac{i\,\omega}{\xi_j}} \tag{5.29}$$

Solving these equations yields the frequency-dependant temperature change $\delta T(\omega)$ induced by the pump beam through local heating.

For the calculation of absolute signal contributions the influence of ΔT on the change of the dielectric constant has to be considered. For small changes $\delta\varepsilon$ of the complex dielectric constant ε

$$\delta\varepsilon = \frac{d\varepsilon}{dn}\frac{dn}{dT}\delta T = 2n\frac{dn}{dT}\delta T = \eta\delta T \tag{5.30}$$

The evanescent plasmon field experiences an effective change of the dielectric constant of

$$\begin{aligned}
\Delta\varepsilon &= \alpha_0 \int_0^\infty e^{-\alpha_0 z}\ \delta\varepsilon(z)\ dz \\
&= \eta\alpha_0 \int_0^\infty e^{-\alpha_0 z}\ \delta T(z)\ dz \\
&= \eta\alpha_0 \int_0^\infty dk\ k\ J_0(0) \left(\frac{\Gamma_0}{2\alpha_0} + \frac{\Gamma_1 - \Gamma_0 + A + B}{\alpha_0 + \beta_0}\right)
\end{aligned} \tag{5.31}$$

The actual change of the angular reflectance curve ΔR is then accessible by the known procedure outlined in 2.1.5. Results are shown in figure 5.4. The maximum values of the absolute reflectance change are plotted versus angular frequency.

Clearly visible are two distinct cut-off frequencies that are attributed to different low-passes in the system. Above a cut-off frequency of roughly 50 Hz the real part and the imaginary part of ΔR decline as a function of modulation frequency ω, essentially following a $\omega^{-1/2}$ dependence, which transforms to a ω^{-1} roll-off at even higher frequencies. The cut-off frequencies are due to the fact that the penetration depth of the thermal wave decreases with increasing frequency. The penetration depth passes certain geometrical limits which are the pump spot size and the transverse plasmon decay length in the dye solution. At these points the effective thermal conductivities and diffusivities change, which leads to differences in heat transport.

The implications that follow are here that for high enough modulation frequencies of the pump light the unwanted thermal change in reflectance can be suppressed.

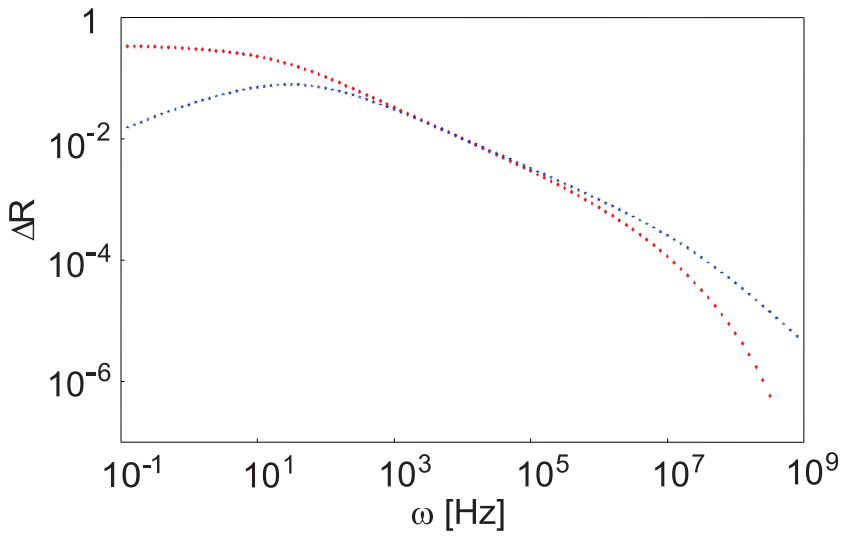

Fig. 5.4. Calculation of the thermal change of reflectance. In-phase part (red) and out-of-phase part (blue) with respect to the power modulation are shown.

5.2.3 Kramers-Kronig Analysis

The relation between dispersion and absorption processes in materials are described by the Kramers-Kronig relations [Kramers, 1926; Kronig, 1926], which couple the real and imaginary parts of the complex dielectric constant in the following way

$$\text{Re } \epsilon(\omega) = 1 + \frac{2}{\pi} \text{ P} \int_0^\infty \frac{\omega' \text{ Im } \{\epsilon(\omega')\}}{\omega'^2 - \omega^2} \, d\omega', \tag{5.32}$$

$$\text{Im } \epsilon(\omega) = -\frac{2\omega}{\pi} \text{ P} \int_0^\infty \frac{[\text{ Re } \{\epsilon(\omega')\} - 1]}{\omega'^2 - \omega^2} \, d\omega', \tag{5.33}$$

These relations are of general validity because they only rely on the assumption that dielectric displacement and electric field are connected by a causal relation. The main problem for practical application of those formulas is that one needs to know Im (ε) over all frequencies to determine Re (ε) using the Hilbert transform, whereas a given experiment only yields values over a finite frequency range. This can be handled in a crude manner, i.e. some approximation for Im (ε) is used outside the measured frequency range, most

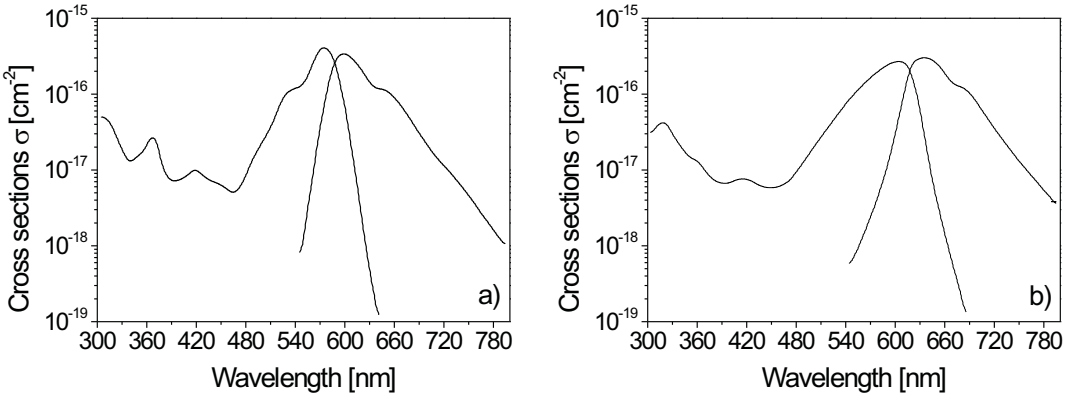

Fig. 5.5. Absorption and emission cross sections of rhodamine 101 (a) and cresyl violet (b) (reproduced from [Bäumler et al., 1992]).

simply the values are set to zero. This is certainly not the correct solution of the given problem, however, under certain circumstances it can be a valuable approximation.

In order to understand the associated changes in the real part of the dielectric constant of the dye solution for the case that the imaginary part changes (which is the case when the excited state gets populated), equation 6.1 is applied to experimental data of absorption and emission cross sections of cresyl violet and rhodamine 101 (Fig. 5.5). In the four-level picture state 2 gets populated and leads to negative absorption. The emission cross section describes this process because we are dealing with stimulated emission, which is the inverse process of absorption. Additionally level 0 gets depopulated. This leads to decreased absorption described by the absorption cross section.

Resulting relative changes of $\Delta\epsilon_r$ at λ=632.8 nm from this analysis are listed in table 5.1. Note that no absolute values are shown, as indicated by an arbitrary factor c (c depending on dye concentration). Both fluorescence (stimulated emission) and absorption contribute with the same sign to the change in $\Delta\epsilon_i$, hence, the sum of the two contributions has to be taken for the whole effect. This yields relative values of $\Delta\epsilon_r/\Delta\epsilon_i \simeq 0.39$ for cresyl violet and $\Delta\epsilon_r/\Delta\epsilon_i \simeq 1.65$ for rhodamine 101. This shows, that the two dyes have quite different properties which will eventually become experimentally evident in significant differences in the ΔR line shape. Note that excited state

Table 5.1. Calculated contributions to $\Delta\epsilon$ from Kramers-Kronig-analysis.

data	$c{\cdot}\Delta\epsilon_r$	$c{\cdot}\Delta\epsilon_i$
cresyl violet fluorescence	$-3.7{\cdot}10^7$	$-1.9{\cdot}10^8$
cresyl violet absorbance	$1.2{\cdot}10^8$	$-2.4{\cdot}10^7$
rhodamine 101 fluorescence	$7.5{\cdot}10^7$	$-8.4{\cdot}10^7$
rhodamine 101 absorbance	$6.5{\cdot}10^7$	$-8.6{\cdot}10^5$

absorption, which might be a considerable factor [Tarkovsky et al., 2003], is neglected in the calculation because no experimental data was available. The above ratios are then used for the calculation of differential reflectance curves for given changes $\Delta\epsilon_i$.

5.2.4 Differential Angular Reflection

With the knowledge of thermal changes and of the relation between dispersion and absorption processes described by the Kramers-Kronig relations it is now possible to calculate the differential angular reflection that reveals the stimulated emission process. Again Maxwell's equations are solved for stratified media, but now including gain, i.e. the change in the real and imaginary parts of the dielectric constant of the dye solution according to

$$\Delta\varepsilon_d'' = \frac{n\lambda_e}{2\pi}(N_3 - N_2)\sigma_e, \tag{5.34}$$

where n is the refractive index of the solvent, λ_e the emission wavelength in vacuum, σ_e the emission cross section of the dye, and $N_3{\approx}0$ and N_2 denote the number density of molecules in states 3 and 2 in the solution. From $\Delta\varepsilon_d''$ the value of $\Delta\varepsilon_d'$ follows according to section 5.2.2.

If $|E_p|$ denotes the electric-field amplitude of the pump plasmon in the dye solution and σ_p is the absorption cross section of the dye at the pump

wavelength λ_p, then the pump rate experienced by a molecule in the ground state is

$$k_p = \varepsilon_0 n \lambda_p \sigma_p |E_p|^2/(2h), \tag{5.35}$$

where h is Planck's constant and ε_0=8.85×10^{-12} C/(Vm). The plasmon intensity $|E_p|^2$ is enhanced with respect to the square modulus $|E_i|^2$ of the incident field in the prism by a factor up to v=35, as calculated by an analysis of the reflection at the layered system glass-metal-liquid. In the center of the pump focus, $|E_i|^2$ can be deduced from the power P_p of the pump beam according to

$$|E_i|^2 = 4P_p/(\pi w_p^2 \varepsilon_0 n_G c), \tag{5.36}$$

n_G=1.5 being the refractive index of the prism and c the speed of light. The risk of thermal damage does not allow us to raise the pump power much above 10 mW. For P_p=10 mW and σ_p=3×10^{-16} cm^2, one obtains a pump rate k_p=1×10^6 s^{-1}. Within the four-level model, the population of the upper level 2 in the steady state is determined by the ratio of the pump rate and the spontaneous decay rate k_s:

$$N_2 = N k_p/(k_p + k_s). \tag{5.37}$$

With a typical lifetime of state 2 of 3 ns we have k_s=3.3×10^8 s^{-1} and thus N_2=3×10^{-3}N, which is only a small fraction of the total number of molecules. According to equation 5.34 the change of the imaginary part of the dye dielectric index can be expected to be in the order of $\sim 10^{-5}$. Therefore, only a rather small modification of the reflectance is expected. In fact, the signal is so small that a special detection method has to be used which is described in the next section. Results of the calculations are shown later on together with experimental curves.

5.3 Setup

The dye (either rhodamine 101 or cresyl violet) is optically pumped by a dye laser operating at λ_p=580 nm. To couple the pump light to the dye molecules close to the silver film the pump beam is made to excite a plasmon at the metal surface [Lakowicz, 2004]. The evanescent field of this plasmon, which is enhanced with respect to the incident field, ensures efficient pumping within a layer having a thickness of the order of 100 nm.

This is realized in a twin-ATR setup sketched in Fig. 5.6. The pump light and the light of a He Ne laser (λ_e=632.8 nm) exciting the plasmon to be amplified enter the prism through opposite faces. The pump light is focussed to a $1/e^2$ radius of w_p=130 μm while the probe beam is more tightly focussed, so that its spot with a radius w_e=60 μm is completely covered by the pump focus.

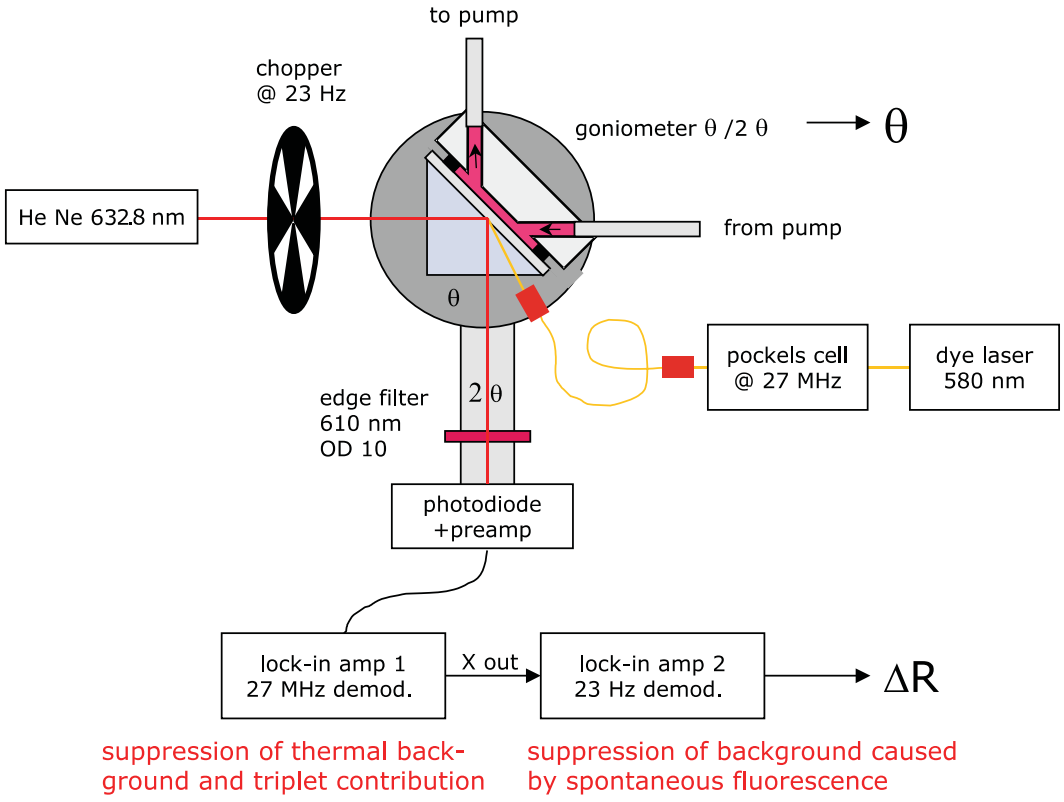

Fig. 5.6. SPASER setup.

A flow cell through which the dye solution circulates is attached to the side

of the prism carrying the metal film. The continuous exchange of the solution at the interface is necessary for the following reasons: photobleaching would otherwise lead to loss of the gain within seconds, and the circulation also helps to reduce the heat load caused by absorption of the pump light in the metal film and in the dye, as even for small pump powers of about 10 mW the ethanol solution starts to boil if not circulated.

Rotating the prism by means of a goniometer varies the angle of incidence of the probe beam while a photodiode monitors the reflected power, thereby recording the reflectance curve. An edge filter with an optical density of 10 at 580 nm prevents stray light produced by the pump beam from reaching the detector. The pump beam is delivered to the prism via a polarization preserving single-mode fiber connected to the Θ-turntable of the goniometer, so that its incidence angle always stays constant. The axis of rotation is offset with respect to the symmetry plane in such a way that the probe spot remains stationary on the silver film during the rotation and, hence, the overlap with the pump focus is preserved. In the case of rhodamine 101 the prism is moved slowly in the direction normal to the plane of incidence during the measurement, so that fresh silver film is continuously moved into the focus. This keeps the problem of photochemical film deterioration to a minimum which is otherwise observed upon inspection as adhering dark remnants on the silver film.

To single out the expected weak effect of stimulated emission with high sensitivity a dynamic measurement with phase-sensitive detection is applied. The pump power is modulated by means of an resonantly driven electro-optic modulator working at 27 MHz while a lock-in amplifier (SR 844, Stanford Research Systems) measures the corresponding modulation as detected by the photodiode. The main part of this signal stems from spontaneous decay of the dye molecules leading to excitation of plasmons on the silver film, whose radiative decay in turn gives rise to directional emission of fluorescence light. This light is concentrated in a cone around the pump focus (see Fig. 5.1). To discriminate the small amount of light produced by stimulated emission against this fluorescence background, the probe beam is mechanically chopped at 23 Hz, which produces a small modulation at the output of the lock-in amplifier. This modulation is detected with a second lock-in amplifier (SR 830, Stanford Research Systems), whose output signal - measured as a function of

the incidence angle of the probe laser beam - directly reflects the difference between the reflectance curves in the presence and absence of the pump beam.

The choice of modulation frequency of the pump light is dictated by the need of suppressing two types of background:

- The thermal effect as discussed before. Above a cut-off frequency of roughly 50 Hz the thermal induced reflectance change declines as a function of modulation frequency ω, essentially following a $\omega^{-1/2}$ dependence, which transforms to a ω^{-1} roll-off at even higher frequencies. At a modulation frequency of 27 MHz, which corresponds to $\omega = 2\pi\times 27$ MHz $\cong$0.17 GHz, the thermal effect is reduced by several orders of magnitude allowing for an observation of the pure effect of stimulated emission. It would not be possible to increase this frequency much further, since then the limit given by the inverse lifetime τ_S^{-1} of the first singlet state would be approached, leading to a loss of signal until it would finally vanish.

- Intersystem crossing transfers some of the excited dye molecules to the metastable triplet state with a lifetime τ_T of microseconds. Periodic optical pumping produces complementary modulation of the populations in the triplet and in the ground state. This may contribute to the change of the dielectric constant of the dye solution and thus represents a further source of background. At frequencies ω larger than τ_T^{-1} this population modulation decreases in proportion to ω^{-1}. Therefore, by choosing a high enough modulation frequency we can suppress both this effect and the thermal background to a large extent. Note, however, that on average also then an appreciable fraction of the molecules may reside in the triplet state, leading to a reduction of the effective density of molecules available for optical pumping. Unlike in a free-jet dye laser the circulation of the dye solution is ineffective in preventing this loss of gain as the flow speed is far too low close to the metal surface.

5.4 Proof of Stimulated Emission

At this point, the actual measurement can be compared with the theoretical predictions following from the previous sections. Figs. 5.7 a) and (b) show experimental differential reflection curves obtained with the two dyes cresyl violet and rhodamine 101 for various thicknesses of the silver film. Theoretical differential reflectance curves are also depicted in Figs. 5.7 c) and (d).

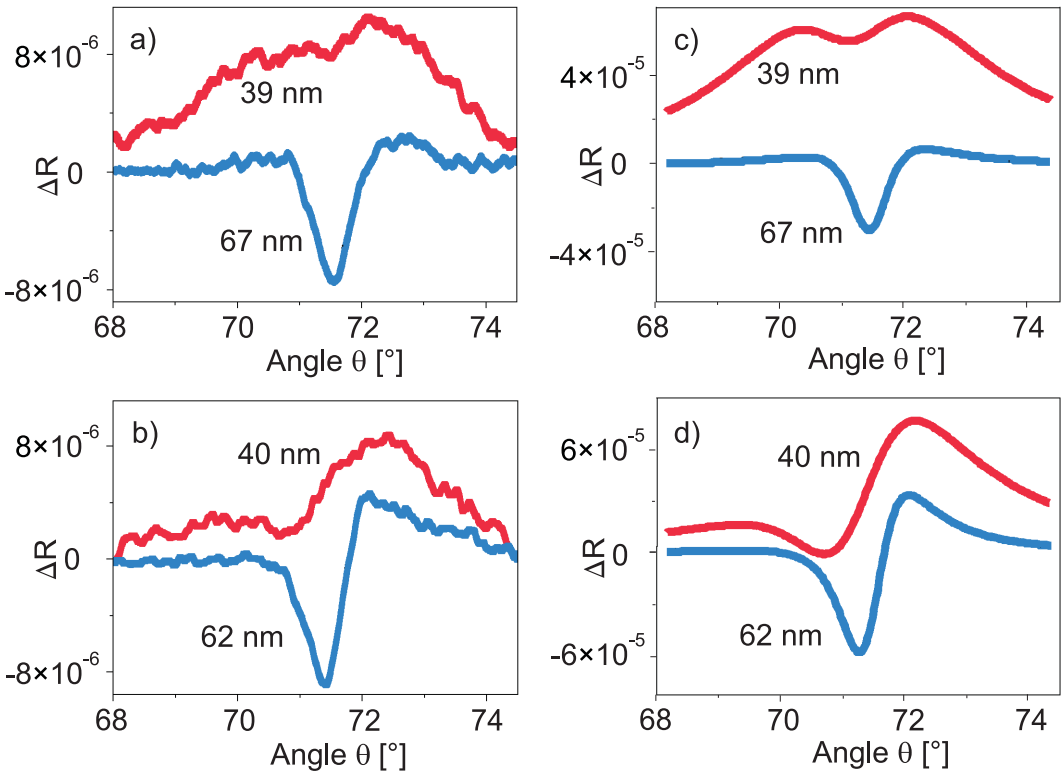

Fig. 5.7. Differential reflectance curves proving stimulated emission of surface plasmons for different metal film thicknesses and dyes; experiment (a, b) and theory (c, d). (a) and (c) refer to cresyl violet, whereas (b) and (d) depict results for rhodamine 101. The respective film thickness is indicated for each curve. The modulation amplitude of the pump power was 10 mW root mean square (rms) for cresyl violet and 9 mW rms for rhodamine 101. The reflectance change ΔR is also given as an rms quantity. The number density of dye molecules was $7 \times 10^{17}\mathrm{cm}^{-3}$ for both dye solutions.

For a film thickness of approximately 40 nm the reflectance change induced by the amplifying medium is positive across the whole reflectance dip (see

the red curves). In this case stimulated emission of SPs simply leads to an increased emission of light into the reflected probe beam due to radiative SP decay. At larger film thicknesses around 65 nm the reduced damping caused by stimulated SP emission manifests itself as a narrowing and deepening of the reflectance dip. This produces a more complicated differential line shape with both positive and negative parts (see the blue curves). In both cases, the effect of stimulated emission is accompanied by an angular shift of the reflectance dip in accordance with $\Delta\epsilon_d^{'}$. The detailed signal shape therefore depends on the ratio $\Delta\epsilon_d^{'}/\Delta\epsilon_d^{''}$ which is different for the two dyes.

The effects listed below have been taken into account in the evaluation. Because they are small they will not change the line shape in a first approximation, however, they alter the absolute signal levels.

- Refraction at the entrance face of the prism makes the beam profile elliptical leading to a change of the effective pump spot size and hence, the introduced pump energy per area. The geometric average of the two elliptic axes is taken as the effective pump spot radius.

- The exponential decay of the pump field into the dye solution results in less efficient pumping of more distant dye molecules as the efficient pump intensity decreases due to absorption of molecules close to the metal film (see treatment in 5.2.1).

- The finite size of the pump focus causes a variation of the pumping efficiency across the probe focus in spite of the fact that the probe spot is completely covered by the pump spot. Comparison of pump spot size (265 μm) and probe spot size (120 μm) for a Gaussian beam yields a factor of ~ 0.8. Hence, the measured signal has been multiplied by a factor of 1.25.

- A thin contamination layer of photochemically deteriorated dye molecules is adsorbed to the silver film causing extra absorption (evidenced by a small change in the reflectance dip). Here the experimental reflectance curve has been fitted assuming a 1 nm thin layer of deteriorated molecules with the dielectric constant of this film as the fit parameter. This layer is then used additionally to the known geometry in all subsequent calculations.

In general, inspection of the experimental curves reveals an excellent agreement with theory as far as the line shape is concerned. In all cases extra absorption instead of gain would lead to a distinctly different signal shape. Hence, the experimental observations provide clear evidence for stimulated emission of surface plasmons. The theory predicts a reduction of the damping by $-\gamma_d \sim 10\ \mathrm{m}^{-1}$, which corresponds to a relative effect of $\sim 1.6 \times 10^{-4}$ with respect to the intrinsic damping. The absolute measured signal levels are generally lower by a factor of 4 to 10 as compared with the theoretical prediction. Four main reasons are expected to contribute to such a loss of signal:

- An appreciable fraction of the dye molecules is trapped in the metastable triplet state, therefore not contributing to the signal. The actual number is difficult to determine, because flow cell parameters and certain gas concentrations (solved oxygen, i.e. air) contribute.

- Additionally, the dye molecules closest to the metal surface are subject to an increased decay rate due to radiationless energy transfer to the metal [Waldeck et al., 1985; Chance et al., 1978]. This strongly reduces the number of molecules in level 2 in a layer approximately 20 nm thick.

- Absorption in the excited state to higher singlet states might occur leading to a decreased population of level 2 of the dye. There is no experimental data available for the dyes in use, however, the effect might contribute significantly to loss of signal, as shown for other organic dyes [Tarkovsky et al., 2003].

In conclusion, stimulated emission of surface plasmons based on optically pumped organic dye molecules as the gain medium has been realized. For future applications higher gain levels are clearly necessary. This should be feasible, since the quantum mechanical limit of the gain cross section [Klyshko, 1988], given by

$$\sigma_g = \frac{3\lambda^2}{2\pi} \tag{5.38}$$

is many orders of magnitude higher than those known for highly efficient organic dyes [Pisignano et al., 2002]. For these dyes gain coefficients of $\gamma_d =$

$2.2 \times 10^3 \mathrm{cm}^{-1}$ have been reported, which is only a factor of 30 below the intrinsic losses of the plasmon in the TATR-geometry. To solve this problem, more efficient materials and pumping methods must be developed, including for example strong local field enhancement in suitable nanostructures, pumping in quantum dots and electrical pumping in semiconductor heterostructures. The latter ones are especially promising, as they have been shown to provide gain coefficients of up to $\gamma_d = 3 \times 10^4 \mathrm{cm}^{-1}$ [Zory, 1993]. This might lead to the development of novel efficient plasmon and light emitters, which holds great potential for applications in nanooptics.

6 Conclusion and Outlook

In this work experiments on surface plasmons on thin metallic films were performed using near-field optical microscopy and differential reflectance spectroscopy under ambient conditions. The following questions were addressed:

- Imaging of surface plasmon fields by near-field optical microscopy
- Understanding of near-field image contrast and influence of different near-field probes
- Influence of single grooves in the plasmon-supporting metal film on surface plasmon propagation
- Theoretical description and feasibility of stimulated emission of surface plasmon polaritons
- Experimental implementations of stimulated emission of surface plasmon polaritons

The following experimental observations have been made:

- Conventional metal-coated SNOM probes are not suited to image surface plasmons because of strong disturbances caused by the metal cladding. Uncoated bare dielectric fibres are a better choice.
- A straight groove in a metal film causes the two plasmon modes at the two film boundaries in the ATR geometry to exchange energy and this coupling can be rather pronounced. Coupling efficiencies were determined.

- SNOM provides a unique tool for studying this phenomenon by directly accessing surface bound electromagnetic fields and subsequent analysis of the standing-wave patterns created by the interfering plasmon modes.

- Stimulated emission of surface plasmon polaritons by optical pumping of organic dye molecules has been proven.

- A detailed theoretical description and one suitable experimental realization have been given. The new concept of Twin Attenuated Total Reflection was introduced.

Plasmon Mode Selection by Refraction

As shown in chapter 4 the k vectors of the silver-air and silver-glass plasmon modes are different. If the plasmon is not incident perpendicularly on the groove, but rather under an angle α, there must be refraction for the transmitted lower mode according to Snell′s law

$$k \ \sin\alpha = k' \ \sin\beta, \tag{6.1}$$

which opens the field for other interesting applications, e.g the spatial selection of modes. Here, the groove acts as a beam splitter for different modes while the splitting depends upon the incident angle of the plasmon on the groove. This effect should be observable in an experiment as the lower mode changing direction with respect to the incident plasmon, i.e. it propagates with a smaller angle β to the groove normal. A double groove structure can act as a test structure. Each groove would then be e.g. 100 μm long with a separation of 30 μm as shown in Figure 6.1.

Here, groove (1) couples part of the incident plasmon field to the lower mode. This mode propagates at the metal-glass interface until it is disturbed by the second groove. Groove (2), which is broader (e.g. some microns), then acts as

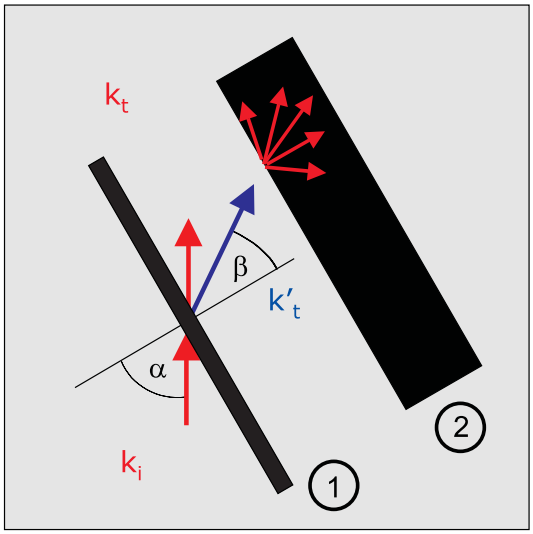

Fig. 6.1. Mode selection by refraction. Groove (1) couples part of the incident plasmon field to the lower mode. Groove (2) acts as probe by scattering the lower mode into observable light.

a probe, scattering the lower mode into observable light.

Appendix

MATHEMATICA® Scripts for Solving Maxwell's Equations for Stratified Media

The following code has been successfully tested with the *MATHEMATICA*® 4.0 software system from Wolfram research (http://www.wolfram.com/). It is intended for a 4-layer system but can easily be adjusted to more layers from symmetry considerations.

Calculation of angle-dependant reflectance spectra

```
(* Calculation of Angle-Dependant Reflectance Spectra *)

e0:=(1.5152)^2
e1:=(1.5152)^2
e2 := -17.99639 - I 0.50912 (* e'' is negative, because
exp(+iwt) for plane waves *)
e3:=1

a0 := 1
h1 := 2.4 10^(-6)
h2 := 60 10^(-9)
lambda := 632.8 10^(-9)
c := 3 10^(8)
w = 2 Pi c/lambda
```

```
theta := (x/180)* Pi

gamma0 = Sqrt[-e0 (w^2)]/c
u0 = Sqrt[-e0 (w^2)/c^2 - (gamma0 Sin[theta])^2]
u1 = Sqrt[-e1 (w^2)/c^2 - (gamma0 Sin[theta])^2]
u2 = Sqrt[-e2 (w^2)/c^2 - (gamma0 Sin[theta])^2]
u3 = Sqrt[-e3 (w^2)/c^2 - (gamma0 Sin[theta])^2]

r0 = I w e0
r1 = I w e1
r2 = I w e2
r3 = I w e3

ergebnis := NSolve[{a0 + b0 == a1 + b1,
(-a0 u0 + b0 u0)/r0 == (-a1 u1 + b1 u1)/r1,
a1 Exp[-u1 h1] + b1 Exp[u1 h1] == a2 Exp[-u2 h1] + b2 Exp[u2 h1],
a3 Exp[-u3 (h1 + h2)] == a2 Exp[-u2 (h1 + h2)] + b2 Exp[u2 (h1
+ h2)],
(-a1 u1/r1) Exp[-u1 h1] + (b1 u1/r1) Exp[ u1 h1] == (-a2 u2/r2)
Exp[-u2 h1] + (b2 u2/r2) Exp[ u2 h1], (-a2 u2/r2) Exp[-u2 (h1 +
h2)]
+ (b2 u2/r2) Exp[ u2 (h1 + h2)] == (-a3 u3/r3) Exp[-u3 (h1 + h2)]},
{a1, a2, a3, b0, b1, b2}, 200]

H0[z_] := a0 Exp[-u0 z] + b0 Exp[u0 z] /.  ergebnis
H1[z_] := a1 Exp[-u1 z] + b1 Exp[u1 z] /.  ergebnis
H2[z_] := a2 Exp[-u2 z] + b2 Exp[u2 z] /.  ergebnis
H3[z_] := a3 Exp[-u3 z] /.  ergebnis

R[x_] := Abs[(b0/a0)]^2 /.  ergebnis Plot[R[x],
{x, 40, 50}, PlotRange -> {0.0, 1}, PlotPoints -> 300,
Axes -> False, Frame -> True, GridLines -> {Automatic, Automatic},
FrameLabel -> {"theta [°]", "R(theta)"}]

{* end *}
```

Calculation of the Electromagnetic Field Distribution and Energy Dissipation

```
(* Calculation of the Electromagnetic Field Distribution
and Energy Dissipation *)

e0:=(1.5152)^2
e1:=(1.5152)^2
e2 := -17.99639 - I 0.50912 (* e'' is negative, because exp(+iwt)
for plane waves *)
e3:=1

a0 := 1
h1 := 2.4 10^(-6)
h2 := 60 10^(-9)
lambda := 632.8 10^(-9)
c := 3 10^(8)
w = 2 Pi c/lambda
theta := (42.8/180)* Pi

gamma0 = Sqrt[-e0 (w^2)]/c
u0 = Sqrt[-e0 (w^2)/c^2 - (gamma0 Sin[theta])^2]
u1 = Sqrt[-e1 (w^2)/c^2 - (gamma0 Sin[theta])^2]
u2 = Sqrt[-e2 (w^2)/c^2 - (gamma0 Sin[theta])^2]
u3 = Sqrt[-e3 (w^2)/c^2 - (gamma0 Sin[theta])^2]

r0 = I w e0
r1 = I w e1
r2 = I w e2
r3 = I w e3

ergebnis := NSolve[{a0 + b0 == a1 + b1,
(-a0 u0 + b0 u0)/r0 == (-a1 u1 + b1 u1)/r1,
a1 Exp[-u1 h1] + b1 Exp[u1 h1] == a2 Exp[-u2 h1] + b2 Exp[u2 h1],
a3 Exp[-u3 (h1 + h2)] == a2 Exp[-u2 (h1 + h2)] + b2 Exp[u2 (h1
+ h2)],
(-a1 u1/r1) Exp[-u1 h1] + (b1 u1/r1) Exp[ u1 h1] == (-a2 u2/r2)
Exp[-u2 h1] + (b2 u2/r2) Exp[ u2 h1], (-a2 u2/r2) Exp[-u2 (h1
+ h2)]
```

```
+ (b2 u2/r2) Exp[ u2 (h1 + h2)] == (-a3 u3/r3) Exp[-u3 (h1 + h2)]},
{a1, a2, a3, b0, b1, b2}, 200]

H0[z_] := a0 Exp[-u0 z] + b0 Exp[u0 z] /.  ergebnis
H1[z_] := a1 Exp[-u1 z] + b1 Exp[u1 z] /.  ergebnis
H2[z_] := a2 Exp[-u2 z] + b2 Exp[u2 z] /.  ergebnis
H3[z_] := a3 Exp[-u3 z] /.  ergebnis

E1x[z_] =(-1)/r1) D[H1[z], z]
E2x[z_] =(-1)/r2) D[H2[z], z]
E3x[z_] =(-1)/r3) D[H3[z], z]

E1z[z_] = (1/r1) (-1) (gamma0 Sin[theta]) H1[z]
E2z[z_] = (1/r2) (-1) (gamma0 Sin[theta]) H2[z]
E3z[z_] = (1/r3) (-1) (gamma0 Sin[theta]) H3[z]

pointingx1[z_] := 0.5 Re[-E1z[z] Conjugate[H1[z]]]
pointingx2[z_] := 0.5 Re[-E2z[z] Conjugate[H2[z]]]
pointingx3[z_] := 0.5 Re[-E3z[z] Conjugate[H3[z]]]

divpointing1[z_] := 0.5 w 8.854 10^2(-12) Im[e1] (Re[E1x[z]]^2
+ Re[E1z[z]]^2
+ Im[E1x[z]]^2 + Im[E1z[z]]^2)
divpointing2[z_] := 0.5 w 8.854 10^2(-12) Im[e2] (Re[E2x[z]]^2
+ Re[E2z[z]]^2
+ Im[E2x[z]]^2 + Im[E2z[z]]^2)
divpointing3[z_] := 0.5 w 8.854 10^2(-12) Im[e3] (Re[E3x[z]]^2
+ Re[E3z[z]]^2
+ Im[E3x[z]]^2 + Im[E3z[z]]^2)

(* Graphen Divergenz Poynting - Vektor - Betrag*)

graph5 = Plot[pointingx[z], {z, h1, (h1 + h2)}, PlotPoints -> 100]
graph6 = Plot[divpointing1[z], {z, (h1 - 0.1 10^2(-6)), h1},
PlotPoints -> 100]
graph7 = Plot[divpointing2[z], {z, h1, (h1 + h2)},
PlotPoints -> 100, PlotRange -> {0, (-6 10^(-13))}]
graph8 = Plot[divpointing3[z], {z, (h1 + h2),
(h1 + h2 + 0.1 10^(-6))},
```

```
PlotPoints -> 100]

graphdivpointingall = Show[graph6, graph7, graph8, PlotRange
-> 0, -6 10^(-13),
Axes -> False, Frame -> True, GridLines -> {{h1, (h1 + h2)},
Automatic}, FrameLabel -> {"z-Wert [m]", "div S(z) [a.u.]"}]

(* Graphen H - Felder *)

graph1 = Plot[Abs[H1[z]], {z, (h1 - 0.1 10^(-6)), h1}]
graph2 = Plot[Abs[H2[z]], {z, h1, (h1 + h2)}]
graph3 = Plot[Abs[H3[z]], {z, (h1 + h2), (h1 + h2 + 0.1 10^(-6))}]

(graphHfieldall = Show[graph1, graph2, graph3, Axes -> False,
Frame -> True,
GridLines -> {{h1, (h1 + h2)}, Automatic},
FrameLabel -> {"z-Wert [m]",
"H_y(z) [a.u.]"}]

(* end *)
```

Bibliography

Abbe, E., Beiträge zur Theorie des Mikroskops, M. Schulzes Archiv für mikroskop. Anat. **9**, 413 (1873), also in: Gesammelte Abhandlungen, Vol. 1, (Verlag Gustav Fischer, Jena 1904).

Adam, P. M., Salomon, L., de Fornel, F., Goudonnet, J. P., Determination of the spatial extension of the surface-plasmon evanescent field of a silver film with a photon scanning tunneling microscope, Phys. Rev. B **48**, 2680 (1993).

Agranovich, V. M., Mills, D. L., (eds.), Surface Polaritons (North Holland Publishing Company, Amsterdam 1982).

Alivisatos, A. P., Barbara, P. F., Castleman, A. W., Chang, J., Dixon, D. A., Klein, M. L., McLendon, G. L., Miller, J. S., Ratner M. A., Rossky, P. J., Stupp, S. I., Thompson, M. E., From Molecules to Materials: Current Trends and Future Directions, Adv. Mater. **10**, 1297 (1998).

Andrei, E. Y., (ed.), Two-Dimensional Electron Systems in Helium and Other Cryogenic Substrates (Kluwer Academic Publishers, Dordrecht 1997).

Ash, E. A., Nichols, G., Super Resolution Aperture Scanning Microscope, Nature **237**, 510 (1972).

Baida, F. I., Van Labeke, D., Vigoureux, J.-M., Near-field surface plasmon microscopy: A numerical study of plasmon excitation, propagation, and edge interaction using a three-dimensional Gaussian beam, Phys. Rev. B **60**, 7812 (1999).

Baida, F. I., Van Labeke, D., Vigoureux, J.-M., Theoretical study of near-field surface plasmon excitation, propagation and diffraction, Optics Commun. **171**, 317 (1999).

Baida, F. I., Van Labeke, D., Bouhelier, A., Huser, T., Pohl, D. W., Propagation and diffraction of locally excited surface plasmons, J. Opt. Soc. Am. A **18**, 1552 (2001).

Baranova, E. G., On the concentration quenching of the luminescence of rhodamine 6G solutions, Opt. Spectr. **18**, 230 (1965).

Barnes, W. L., Preist, T. W., Kitson, S. C., Sambles, J. R., Physical origin of photonic energy gaps in the propagation of surface plasmons on gratings, Phys. Rev. B **54**, 6227 (1996).

Barnes, W. L., Topical review. Fluorescence near interfaces: the role of photonic mode density, J. Mod. Opt. **45**, 661 (1998).

Barnes, W. L., Dereux, A., Ebbesen, T. W., Surface plasmon subwavelength optics, Nature **424**, 824 (2003).

Bäumler, W., Schmalzl, A. X., Gößl, G., Penzkofer, A., Fluorescence decay studies applying a cw femtosecond dye laser pumped ungated inverse time-correlated single photon counting system, Meas. Sci. Technol. **3**, 384, (1992).

Baur, C., Koslowski, B., Mller, R., Dransfeld, K., in: Near Field Optics, Pohl, D. W. and Courjon D. (eds.) (Kluwer, Amsterdam 1993).

Beaumont, P. C., Johnson, D. G., Parsons, B. J., Photophysical properties of laser dyes: picosecond laser flash photolysis studies of Rhodamine 6G, Rhodamine B and Rhodamine 101, J. Chem. Soc., Faraday Trans. **89**, 4185 (1993).

Becker, R. S., Theory and Interpretation of Fluorescence and Phosphorescence (Wiley-Interscience, New York 1969).

Berenger, J.-P., A perfectly matched layer for the absorption of electromagnetic waves, J. Comput. Phys. **114**, 185 (1994).

Bergman, D. J., Stockman, I., Surface plasmon amplification by stimulated emission of radiation: quantum generation of coherent surface plasmons in nanosystems, Phys. Rev. Lett. **90**, 027402 (2003).

Berini, P., Plasmon-polariton modes guided by a metal film of finite width, Opt. Lett. **24**, 1011 (1999).

Betzig, E., Finn, P. L., Weiner, J. S., Combined shear force and near-field scanning optical microscopy, Appl. Phys. Lett. **60**, 2484 (1992).

Betzig, E., Trautmann, J. K., Weiner, J. S., Harrris, T. D., Wolfe, R., Polarization contrast in near-field scanning optical microscopy, Appl. Opt. **31**, 4563 (1992).

Betzig, E., Chichester, R. J., Single Molecules Observed by Near-Field Scanning Optical Microscopy, Science **262**, 1423 (1993).

Birks, J. B., Photophysics of Aromatic Molecules (Wiley-Interscience, New York 1970).

Bischoff, L., Teichert, J., Hesse, E., Panknin, D., Skorupa, W., $CoSi_2$ microstructures by means of a high current focused ion beam, J. Vac. Sci. Technol. B **12**, 3523 (1994).

Bischoff, L., Teichert, J., Focused Ion Beam Sputtering of Silicon and Related Materials, interna Forschungszentrum Rossendorf, FZR-**217**, March 1998.

Boardman, A. D., (ed.), Electromagnetic surface modes (Wiley, New York 1982).

Born, M., Wolf, E., Bhatia, A. B., Principles of Optics (Cambridge University Press, Cambridge 1999).

Bouhelier, A., Huser, Th., Freyland, J. M., Güntherodt, H.-J., Pohl, D. W., Plasmon transmissivity and reflectivity of narrow grooves in a silver film, J. Microsc. **194**, 571 (1999).

Bouhelier, A., Huser, T., Tamaru, H., Güntherodt, H.-J., Pohl, D. W., Baida, F. I., Van Labeke, D., Plasmon optics of structured silver films, Phys. Rev. B **63**, 155404 (2001).

Boykin, P. O., Paesler, M. A., Yakobson, B. I., Energy Dissipation in NSOM Probe Fiber Tapers: Ray Tracing Assessment, Proc. SPIE **2677**, 148 (1996).

Bozhevolnyi, S. I., Smolyaninov, I. I., Zayats, A. V., Near-field microscopy of surface-plasmon polaritons: localization and internal interface imaging, Phys. Rev. B **51**, 17916 (1995).

Bozhevolnyi, S. I., Vohnsen, B., Smolyaninov, I. I., Zayats, A. V., Direct observation of surface polariton localization caused by surface roughness, Opt. Commun. **117**, 417 (1995).

Bozhevolnyi, S. I., Vohnsen, B., Zayats, A. V., in: Optics at the Nanometer Scale, M. Nieto-Vesperinas and N. Garcia (eds.) (Kluwer Academic, Dordrecht 1996).

Bozhevolnyi, S. I., Pudin, F. A., Two-dimensional microoptics of surface plasmons, Phys. Rev. Lett. **78**, 2829 (1997).

Bozhevolnyi, S. I., Vohnsen B., Near-field optics with uncoated fiber tips: light confinement and spatial resolution, J. Opt. Soc. Am. B **14**, 1656 (1997).

Bozhevolnyi, S. I., Topographical artifacts and optical resolution in near-field optical microscopy, J. Opt. Soc. Am. B **14**, 2254 (1997).

Bozhevolnyi S. I., Coello, V., Elastic scattering of surface plasmon polaritons: Modelimg and experiment, Phys Rev. B **58**, 10899 (1998).

Bozhevolnyi, S. I., Near-field optical microscopy of localized excitations on rough surfaces: influence of a probe, J. Microsc. 194, 561 (1999).

Bozhevolnyi, S. I., Erland, J., Leosson, K., Skoglund, P. M. W., Hvam, J. M., Waveguiding in Surface Plasmon Polariton Band Gap Structures, Phys. Rev. Lett. **86**, 3008 (2001).

Bozhevolnyi, S. I. Near-field mapping of surface polariton fields, J. Microsc. **202**, 313 (2002).

Brunner, R., Marti, O., Hollricher, O., Influence of environmental conditions on shear–force distance control in near-field optical microscopy, J. Appl. Phys. **86**, 7100 (1999).

Bruns, R., Raether, H., Plasma Resonance Radiation from Non Radiative Plasmons, Z. Physik **237**, 98 (1970).

Brzoska, J. B., Ben Azouz, I., Rondelez, F., Silanisation of Solid Substrates: A Step toward Reproducibility, Langmuir **10**, 4367 (1994).

Bouwkamp, C. J., On Sommerfeld's surface wave, Phys. Rev. **80**, 294 (1950).

Burstein, E., Pinczuk, A., Mills, D. L., Inelastic light scattering by charge carrier excitations in two-dimensional plasmas: theoretical considerations, Surf. Sci. **98**, 451 (1980).

Carminati, R., Greffet, J.-J., Two-dimensional numerical simulation of the photon scanning tunneling microscope. Concept of transfer function, Opt. Commun. **11**, 316 (1995).

Chance, R. R., Prock, A., Silbey, R., Molecular fluorescence and energy transfer near interfaces, Adv. Chem. Phys. **37**, 1 (1978).

Craig, A. E., Olson, G. A., Sarid, D., Experimental observation of the long-range surface plasmon polariton, Opt. Lett. **8**, 380 (1983).

Courjon, D., Sarayeddine, K., Spajer, M., Scanning tunneling optical microscopy, Opt. Commun. **71**, 23 (1989).

Courjon, D., Near-field optical imaging: some attempts to define an apparatus function, J. Microsc. **177**, 180 (1994).

Ctyroky, J., Homola, J., Lambeck, P. V., Musa, S., Hoekstra, H. J. W. M., Harris, R. D., Wilkinson, J. S., Usievich, B., Lyndin, N. M., Theory and modelling of optical waveguide sensors utilising surface plasmon resonance, Sensors and Actuators B **54**, 66 (1999).

Dawson, P., de Fornel, F., Goudonnet, J.-P., Imaging of surface plasmon propagation and edge interaction using a photon scanning tunneling microscope, Phys. Rev. Lett. **72**, 2927 (1994).

Dawson, P., Puygranier, B. A. F., Cao, W., de Fornel, F., The interaction of surface plasmon polaritons with a silver film edge, J. Microsc. **194**, 578 (1999).

Dawson, P., Puygranier, B. A. F., Goudonnet, J.-P., Surface plasmon polariton propagation length: A direct comparison using photon scanning tunneling microscopy and attenuated total reflection, Phys Rev. B **63**, 205410 (2001).

de Fornel, F., Goudonnet, J. P., Salomon, L., Lesniewska, E., An evanescent field optical microscope, Proc. SPIE **1139**, 77 (1989).

de Fornel, F., Evanescent Waves (Springer, Berlin 2001).

de Hollander, R. B. G., van Hulst, N. F., Kooyman, R. P. H., Near field plasmon and force microscopy, Ultramicroscopy **57**, 263 (1995).

Dereux, A., Girard, C., Weeber, J.-C., Theoretical principles of near-field optical microscopies and spectroscopies, J. Chem. Phys **112**, 7775 (2000).

Devaux, E., Dereux, A., Bourillot, E., Weeber, J.-C., Lacroute, Y., Goudonnet, J.-P., Girard, C., Local detection of the optical magnetic field in the near zone of dielectric samples, Phys. Rev. B **62**, 10504 (2000).

Ditlbacher, H., Krenn, J. R., Schider, G., Leitner, A., Aussenegg, F. R., Two-dimensional optics with surface plasmon polaritons, Appl. Phys. Lett. **81**, 1762 (2002).

Ditlbacher, H., Krenn, J. R., Felidj, N., Lamprecht, B., Schider, G., Salerno, M., Leitner, A., Aussenegg, F. R., Fluorescence imaging of surface plasmon fields, Appl. Phys. Lett. **80**, 404 (2002).

Drexhage, K. H., Design of Laser Dyes, VII. International Quantum Electronics Conference, Montreal, Canada (1972).

Drexhage, K. H., Structure and properties of laser dyes. Dye Lasers. Topics in Applied Physics, Vol. **1**, F. P. Schäfer, (ed.) (Springer Verlag, Hamburg 1973/1977).

Drude, P., Zur Elektronentheorie der Metalle, Annalen der Physik **1**, 566 (1900).

Dyba, M., Hell, S. W., Focal spots of size lambda/23 open up far-field fluorescence microscopy at 33 nm axial resolution, Phys. Rev. Lett. **88**, 163901 (2002).

Ebbesen, T. W., Lezec, H. J., Ghaemi, H. F., Thio, T., Wolff, P. A., Extraordinary optical transmission through subwavelength hole arrays, Nature **391**, 667 (1998).

Eychmüller, A., Structure and photophysics of semiconductor nanocrystals, J. Chem. Phys. B **104**, 6514 (2000).

Fano, U., Some theoretical considerations on anomalous diffraction gratings, Phys. Rev. **50**, 573 (1936).

Fano, U., On the anomalous diffraction gratings. II, Phys. Rev. 51, 288 (1937).

Fano, U., Zur Theorie der Intensittsanomalien der Beugung, Ann. Physik **32**, 393 - 443 (1938).

Ferrell, R. A., Predicted Radiation of Plasma Oscillations in Metal Films, Phys. Rev. **111**, 1214 (1958).

Förster, T., Fluoreszenz organischer Verbindungen (Vandenhoeck and Ruprecht, Göttingen 1951).

Förster, T., 10th Spiers Memorial Lecture. Transfer mechanisms of electronic excitation, Discuss. Faraday Soc. **27**, 7 (1959).

Forstmann, F., Gerhardts, R. R., Metal Optics near the plasma frequency (Springer Tracts in Modern Physics 109, Springer, Berlin 1986).

Glass, N. E., Weber, M., Mills, D. L., Attenuation and dispersion of surface polaritons on gratings, Phys. Rev. B **29**, 6548 (1984).

Greffet, J.-J., Carminati, R. Image formation in near-field optics, Prog. Surf. Sci. 56, 133 (1997).

Gryczynski, I., Malicka, J., Gryczynski, Z., Lakowicz, J. R.,Radiative decay engineering 4. Experimental studies of surface plasmon-coupled directional emission, Anal. Biochem. **324**, 170 (2004).

Hamann, H. F., Gallagher, A., Nesbitt, D. J., Enhanced sensitivity near-field scanning optical microscopy at high spatial resolution, Appl. Phys. Lett. **73**, 1469 (1998).

Hartschuh, A., Anderson, N., Novotny, L., Near-field Raman spectroscopy using a sharp metal tip, J. Microsc. **210**, 234 (2003).

Hecht, B., Bielefeldt, H., Novotny, L., Inouye, Y., Pohl, D. W., Local Excitation, Scattering, and Interference of Surface Plasmons, Phys. Rev. Lett. **77**, 1889 (1996).

Hecht, B., Bielefeldt, H., Inouye, Y., Pohl, D. W., Novotny, L., Facts and artifacts in near-field optical microscopy, J. Appl. Phys. **81**, 2492 (1997).

Hell, S. W., Stelzer, E., Properties of a 4Pi-confocal microscope, J. Opt. Soc. Am. A **9**, 2159 (1992).

Hickel, W., Kamp, D., Knoll, W., Surface-Plasmon Microscopy, Nature **339**, 186 (1989).

Hillenbrand, R., Keilmann, F., Complex Optical Constants on a Subwavelength Scale, Phys. Rev. Lett. **85**, 3029 (2000).

Hoffmann, P., Dutoit, B., Salath, R.-P., Comparaison of mechanically drawn and protection layer chemically etched optical fiber tips, Ultramicroscopy **61**, 165 (1995).

Inagaki, R., Kagami, K., Arakawa, E. T., Photoacoustic observation of nonradiative decay of surface plasmons in silver, Phys. Rev. B **24**, 3644 (1981).

Jackson, W. B., Amer, N. M., Boccara, A. C., Fournier, D., Photothermal deflection spectroscopy and detection, Appl. Opt. **20**, 1333 (1981).

Jackson, J. D., Klassische Elektrodynamik, 2nd ed. (de Gruyter, Berlin 1982).

Jacobs, K., Herminghaus, S., Thin Liquid Films Rupture via Defects, Langmuir **14**, 965 (1998).

Jamid, H. A., Al-Bader, S. J., Diffraction of Surface Plasmon-Polaritons in an Abruptly Terminal Dielectric-Metal Interface, IEEE Phot. Tech. Lett. **7**, 321 (1995).

Jamid, H. A., Al-Bader, S. J., Reflection and Transmission of Surface Plasmon Mode at a Step Discontinuity, IEEE Phot. Tech. Lett. **9**, 220 (1997).

Johnson, S. G., Joannopoulos, J. D., Photonic Crystals: The Road from Theory to Practice (Kluwer, Boston, 2002).

Kalkbrenner, T., Graf, M., Durkan, C., Mlynek, J., Sandoghdar, V., High-contrast topography-free sample for near-field optical microscopy, Appl. Phys. Lett **76**, 1206 (2000).

Karaldjiev, D. I., Toledo-Crow, R., Vaez-Iravani, M., On the heating of the fiber tip in a near-field scanning optical microscope, Appl. Phys. Lett. **67**, 2771 (1995).

Karrai, K., Grober, R. D., Piezoelectric tip-sample distance control for near field optical microscopes, Appl. Phys. Lett. **66**, 1842 (1995).

Karstens, T., Kobs, K., Rhodamine B and Rhodamine 101 as reference substances for fluorescence quantum yield measurements, J. Phys. Chem. **84**, 1871 (1980).

Kawata, S., Near-Field Optics and Surface Plasmon Polaritons (Topics in Applied Physics 81, Springer, Berlin 2001).

Kellogg, R. E., Some aspects of dipole-dipole energy transfer, J. Luminesc. **1-2**, 435 (1970).

Kern, R., in: Sunagawa, I., (ed.), Morphology of crystals (Terra Scientific, Tokyo 1987).

Kim, Y-K., Ketterson, J. B., Morgan, D. J., Scanning plasmon optical microscope operation in atomic force microscope mode, Opt. Lett. **21**, 165 (1996).

Klar, T. A., Engel, E., Hell, S. W., Breaking Abbe's diffraction resolution limit in fluorescence microscopy with stimulated emission depletion beams of various shapes, Phys. Rev. E **64**, 066613 (2001).

Klimov, V. I., Mikhailovsky, A. A., Xu, S., Malko, A., Hollingsworth, J. A., Leatherdale, C. A., Eisler, H-J., Bawendi, M. G., Optical gain and stimulated emission in nanocrystal quantum dots, Science **290**, 314 (2000).

Klimov, V. I., Nanocrystal quantum dots. From fundamental photophysics to multicolor lasing, Los Alamos Science **28**, 214 (2003).

Klyshko, D. N., Photons and Nonlinear Optics (Gordon, New York 1988).

Kneipp, K., Wang, Y., Kneipp, H., Perelman, L. T., Itzkan, I., Dasari, R. R., Feld, M. S., Single Molecule Detection Using Surface-Enhanced Raman Scattering (SERS), Phys. Rev. Lett. **78**, 1667 (1997).

Knoll, W., Kambhampati, D. K., Surface-plasmon optical techniques, Current Opinion in Colloid & Interface Science **4**, 273 (1999).

Konopsky, V. N., Kouyanov, K. E., Novikova, N. N., Investigations of the interference of surface plasmons on rough silver surface by scanning plasmon near-field microscope, Ultramicroscopy **88**, 127 (2001).

Kovacs, G. J., Scott, G. D., Optical excitation of surface plasma waves in layered media, Phys. Rev. B **16**, 1297 (1977).

Krakow, W., Yacaman, M. J., Aragon, J. L., Observation of quasimelting at the atomic level in Au nanoclusters, Phys. Rev. B **49** (15), 10591 (1994).

Kramers, H. A., Some remarks on the theory of absorption and refraction of X-rays, Nature **117**, 775 (1926).

Krenn, J. R., Wolf, R., Leitner, A., Aussenegg, F. R., Near-field optical imaging the surface plasmon fields of lithographically designed nanostructures, Opt. Comm. **137**, 46 (1997).

Krenn, J. R., Dereux, A., Weeber, J. C., Bourillot, E., Lacroute, Y., Goudonnet, J. P., Schider, G., Gotschy, W., Leitner, A., Aussenegg, F. R., Girard,

C., Squeezing the optical near-field zone by plasmon coupling of metallic nanoparticles, Phys. Rev. Lett. **82**, 2590 (1999).

Krenn, J. R., Aussenegg, F. R., Nanooptik mit metallischen Strukturen, Physik Journal (Physikalische Blätter) **3**, 39 (2002).

Krenn, J. R., Ditlbacher, H., Schider, G., Hohenau, A., Leitner, A., Aussenegg, F. R., Surface plasmon micro-and nano-optics, J. Microsc. **209**, 167 (2003).

Krenn, J. R., Leitner, A., Aussenegg, F. R., Metal Nano-Optics, in H. S. Nalwa (ed.), Encyclopedia of Nanoscience and Nanotechnology (American Scientific Publishers, Stevenson Ranch CA, 2004).

Kretschmann, E., Untersuchungen zur Anregung und Streuung von Oberflchenplasmaschwingungen an Silberschichten, Dissertation (Universität Hamburg, 1972).

Kretschmann, E., Raether, H., Radiative decay of non-radiative surface plasmons excited by light, Z. Naturforsch. **23a**, 2135 (1968).

Kronig, R. de L., The theory of dispersion of x-rays, J. Opt. Soc. Am. **12**, 547 (1926).

Kroo, N., Thost, J. P., Vlker, M., Krieger, W., Walther, H., Decay length of surface plasmon determined with a tunnelling microscope, Europhys. Lett. **15**, 289 (1991).

Labardi, M., Patanè, S., Allegrini, M., Artifact-Free Near-Field Optical Imaging by Apertureless Microscopy, Appl. Phys. Lett. **77**, 621 (2000).

Lakowicz, J. R., Principles of Fluorescence Spectroscopy (Kluwer Academic, New York 1999).

Lakowicz, J. R., Shen, Y., D'Auria, S., Malicka, J., Fang, Jiyu, Gryczynski, Z., Gryczynski, I., Radiative decay engineering 2. Effects of silver island films on fluorescence intensity, lifetimes and resonance energy transfer, Anal. Biochem. **301**, 261 (2002).

Lakowicz, J. R., Radiative decay engineering 3. Surface plasmon-coupled directional emission, Anal. Biochem. **324**, 153 (2004).

Laks, B., Mills, D. L., Maradudin, A. A., Surface polaritons on large-amplitude gratings, Phys. Rev. B **23**, 4965 (1981).

Landau, L. D., Lifschitz, E. M., Lehrbuch der theoretischen Physik, Band **8**, Elektrodynamik der Kontinua (Akademie-Verlag, Berlin 1980).

La Rosa, A., Yakobson, B. I., Hallen, H. D., Origins and effects of thermal processes in near-field optical probes, Appl. Phys. Lett. **67**, 2597 (1995).

Leonhardt, H., Weller, A., Luminescence of Organic and Inorganic Materials (Wiley, New York 1962).

Leskova, T. A., Theory of a Fabry-Perot type interferometer for surface polaritons, Solid State Comm. **50**, 869 (1984).

Li, P., Huang, Y., Hu, J., Yuan, C., Lin, B., Surface Plasmon Resonance Studies on Molecular Imprinting, sensors 2002 **2**, 35 (2002).

Lyndin, N. M., Salakhutdinov, I. F., Sychugov, V. A., Usievich, B. A., Pudonin, F. A., Parriaux, O., Long-range surface plasmons in asymmetric layered metal-dielectric structures, Sensors and Actuators B **54**, 37 (1999).

Mackey, M. S., Sisk, W. N., Photostability of pyrromethene 567 laser dye solutions via photoluminescence measurements, Dyes and Pigments **51**, 79 (2001).

Magde, D., Brannon, J. H., Cremers, T. L., Olmsted III, J., Absolute luminescence yield of cresyl violet: A standard for the red, J. Phys. Chem. **83**, 696 (1979).

Magnuson, G. D., Carlston, C. E., Sputtering yields of single crystals bombarded by 1 to 10 keV Ar+ ions, J. Appl. Phys. **34**, 3267 (1963).

Maradudin, A. A., Wallis, R. F., Stegemann, G. I., Surface Polariton Reflection and Transmission at a Barrier, Solid State Commun. **46**, 481 (1983).

Marling, J. B., Gregg, D. W., Wood, L., Chemical quenching of the triplet state in flashlamp-excited liquid organic lasers, Appl. Phys. Lett. **17**, 527 (1970).

Marling, D. W., Wood, L., J. B., Gregg, Long Pulse Dye Laser Across the Visible Spectrum, IEEE J. Quant. Electr. QE-**7**, 498 (1971).

Marti, O., Bielefeldt, H., Hecht, B., Herminhaus, S., Leiderer, P., Mlynek, J., Near-field optical measurement of the surface plasmon field, Opt. Commun. **96**, 225 (1993).

Martín-Moreno, L., García-Vidal, F. J., Lezec, H. J., Pellerin, K. M., Thio, T., Pendry, J. B., Ebbesen, T. W., Theory of Extraordinary Optical Transmission through Subwavelength Hole Arrays, Phys. Rev. Lett. **86**, 1114 (2001).

Martín-Moreno, L., García-Vidal, F. J., Lezec, H. J., Degiron, A., Ebbesen, T. W., Theory of highly directional emission from a single subwavelength aperture surrounded by surface corrugations, Phys. Rev. Lett. **90**, 167401 (2003).

Martín-Moreno, L., García-Vidal, Optical transmission through circular hole arrays in optically thick metal films, Opt. Expr. **12**, 3619 (2004).

Minsky, M., Memoires on inventing the confocal scanning microscope, Scanning, **10**, 128 (1988).

Möller, W., Eckstein, W., Tridyn A TRIM simulation code including dynamic composition changes, Nuclear Instruments & Methods B **2**, 814 (1984).

Möller, W., Eckstein, W., Biersack, J. P., Tridyn-binary collision simulation of atomic collisions and dynamic composition changes in solids, Comput. Phys. Commun. **51**, 355 (1988).

Möller, R., Albrecht, U., Boneberg, J., Koslowski, B., Leiderer, P., Dransfeld, K., Detection of surface plasmons by scanning tunneling microscopy, J. Vac. Sci. Technol. B **9**, 506 (1991).

Mononobe, S., Ohtsu, M., Fabrication of a pencil-shaped fiber probe for near-field optics by selective chemical etching, J. Lightwave Technol. **14**, 2231 (1996).

Moore, C. A., Decker, C. D., Power-scaling effects in dye lasers under high-power laser excitation, J. Appl. Phys. **49**, 47 (1978).

Muchel, F., Zeiss Information No. **100 E**, Oberkochen, 20 (1988).

Narasimhan, L. R., Pack, D. W., Fayer, M. D., Solute-solvent dynamics and interactions in glassy media: Photon echo and optical hole burning studies of cresyl violet in ethanol glass, Chem. Phys. Lett. **152**, 287 (1988).

Nenninger, G. G., Tobiska, P., Homola, J., Yee, S. S., Long-range surface plasmons for high-resolution surface plasmon resonance sensors, Sensors and Actuators B **74**, 145 (2001).

Neumann, T., Johansson, M.-L., Kambhampati, D., Knoll, W., Surface-plasmon fluorescence spectroscopy, Adv. Funct. Mater. **12**, 575 (2002).

Newton, I., Opticks, or, a Treatise of the Reflections, Refractions, Inflections and Colours of Light (Smith & Walford, London 1704).

Nie, S., Emory, S. R., Probing single molecules and single nanoparticles by surface-enhanced Raman scattering, Science **275**, 1102 (1997).

Norton, K. A., Propagatin of radio waves over a plane earth, Nature **135**, 954 (1935).

Novotny, L., Hafner, C., Light propagation in a cylindrical waveguide with a complex, metallic, dielectric function, Phys. Rev. E **50**, 4094 (1994).

Novotny, L., Hecht, B., Pohl, D. W., Interference of locally excited surface plasmons, J. Appl. Phys. **81**, 1798 (1997).

Onderdelinden, D., Single-crystal sputtering including the channeling phenomenon, Can. J. Phys. **46**, 739 (1968).

Otto, A., A new method for exciting nonradiative surface plasma oscillations, phys. stat. sol. **26**, K99 (1968).

Otto, A., Exitation of nonradiative surface plasma waves in silver by the method of frustrated total reflection, Z. Phys. **216**, 398 (1968).

Paesler, M. A., Moyer, P. J., Near-Field Optics: Theory, Instrumentation and Applications (Wiley, New York, 1996).

Pendry, J. B., Martín-Moreno, L., Garcia-Vidal, F. J., Mimicking Surface Plasmons with Structured Surfaces, Science **305**, 847 (2004).

Pincemin, F., Maradudin, A. A., Boardman, A. D., Greffet, J.-J., Scattering of a surface plasmon polariton by a surface defect, Phys. Rev. B **50**, 15261 (1994).

Pisignano, D., Anni, M., Gigli, G., Cingolani, R., Zavelani-Rossi, M., Lanzani, G., Barbarella, G., Favaretto L., Amplified spontaneous emission and efficient tunable laser emission from a substituted thiophene-based oligomer, Appl. Phys. Lett. **81**, 3534 (2002).

Pockrand, I., Reflection of light from periodically corrugated silver films near the plasma frequency, Phys. Lett. A **49**, 259 (1976).

Pockrand, I., Raether, H., Surface plasma oscillations at sinusoidal silver surfaces, Appl. Opt. **16**, 1784 (1977).

Pockrand, I., Raether, H., Surface plasma oscillations at sinusoidal silver surfaces: erratum, Appl. Opt. **16**, 2803 (1977).

Pockrand, I., Brillante, A., Nonradiative decay of excited molecules near a metal surface, Chem. Phys. Lett. **69**, 499 (1980).

Pohl, D. W., Denk, W., Lanz, M., Optical stethoscopy: Image recording with resolution $\lambda/20$, Appl. Phys. Lett. **44**, 651 (1984).

Pohl, D. W., Courjon, D. (eds.), Near Field Optics (Kluwer, Amsterdam 1993).

Pohl, D. W., Novotny, L., Near-field optics: Light for the world of NANO, J. Vac. Sci. Technol. B **12**, 1441 (1994).

Powell, C. J., Swan, J. B., Effect of Oxidation on the Characteristic Loss Spectra of Aluminum and Magnesium, Phys. Rev. **118**, 640 (1960).

Pringsheim, P., Fluorescence and Phosphorescence (Interscience, New York 1949).

Raether, H., Surface Plasmons on Smooth and Rough Surfaces and on Gratings (Springer Tracts in Modern Physics 111, Springer, Berlin 1988).

Rayleigh, Lord, Investigations in optics, with special reference to the spectroscope, Phil. Mag. **8**, 261, 403, 477 (1879).

Reddick, R. C., Warmack, R. J., Ferrel, T. L., New form of scanning optical microscopy, Phys. Rev. B **39**, 767 (1989).

Rendell, R. W., Scalapino, D. J., Surface plasmons confined by microstructures on tunnel junctions, Phys. Rev. B **24**, 3276 (1981).

Ritchie, R. H., Plasma Losses by Fast Electrons in Thin Films, Phys. Rev. **106**, 874 (1957).

Salomon, L., Grillot, F., de Fornel, F., Zayats, A. V., Near-field distribution of optical transmission of periodic subwavelength holes in a metal film, Phys. Rev. Lett. **86**, 1110 (2001).

Salomon, L., Bassou, G., Dufour, J. P., de Fornel, F., Local excitation of surface plasmon polaritons at discontinuities of a metal film: Theoretical analysis and optical near-field measurements, Phys. Rev. B **65**, 125409 (2002).

Sánchez, E. J., Novotny, L., Xie, X. S., Near-Field Fluorescence Microscopy Based on Two-Photon Excitation with Metal Tips, Phys. Rev. Lett. **82**, 4014 (1999).

Sánchez-Gil, J. A., Maradudin, A. A., Near-field and far-field scattering of surface plasmon polaritons by one-dimensional surface defects, Phys. Rev. B **60**, 8359 (1999).

Sarid , D., Long-Range Surface-Plasma Waves on Very Thin Metal Films, Phys. Rev. Lett. **47**, 1927 (1981).

Schäfer, F. P., Dye lasers and laser dyes in physical chemistry, in M. Stuke (ed.), Dye Lasers: 25 Years (Springer, Berlin 1992).

Schmidt, J. U., Aufbau eines kombinierten optischen Nahfeld- und konfokalen Laser-Rastermikroskops zur Abbildung und Spektroskopie fluoreszenzmarkierter Proben, Diplomarbeit TU-Dresden (1997).

Schmidt, J. U., Bergander, H., Eng, L. M., Shear force interaction in the viscous damping regime studied at 100 pN force resolution, J. Appl. Phys. **87**, 3108 (2000).

Schröder, U., Der Einfluss dünner metallischer Deckschichten auf die Dispersion von Oberflächenplasmaschwingungen in Gold-Silber-Schichtsystemen, Surf. Sci. **102**, 118 (1981).

Schüttler, M., Leuschner, M., Lippitz, M., Rühle, W. W., Giessen, H., Towards the Origin of the Shear Force in Near-Field Microscopy, Jpn. J. Appl. Phys., Part 1 **40**, 813 (2001).

Shalaev, V. M., Stockman, M. I., Optical Properties of Fractal Clusters (Susceptibility, Surface Enhanced Raman Scattering by Impurities), Sov. Phys. JETP **65**, 287 (1987).

Shipway, A. N., Katz, E., Willner, I., Nanoparticla Arrays on Surfaces for Electronic, Optical, and Sensor Applications, Chem. Phys. Chem. **1**, 18 (2000).

Simon, H. J., Guha, J. K., Directional surface plasmon scattering from silver films, Opt. Comm. **18**, 391 (1976).

Smolyaninov, I. I., Zayats, A. V., Keller, O., The effect of the surface enhanced polariton field on the tunneling current of a STM, Phys. Lett. A **200**, 438 (1995).

Smolyaninov, I. I., Mazzoni, D. L., Davis, C. C., Imaging of Surface Plasmon Scattering by Lithographically Created Individual Surface Defects, Phys. Rev. Lett. **77**, 3877 (1996).

Smolyaninov, I. I., Mazzoni, D. L., Mait, J., Davis, C. C., Experimental study of surface-plasmon scattering by individual surface defects, Phys. Rev. B **56**, 1601 (1997).

Smolyaninov, I. I., Zayats, A. V., Stanishevsky, A., Davis, C. C., Optical control of photon tunneling through an array of nanometer-scale cylindrical channels, Phys. Rev. B **66**, 205414 (2002).

Snavely, B. B., Schäfer, F. P., Feasibility of CW operation of dye-lasers, Phys. Lett A **28**, 728 (1969).

Sommerfeld, A., Über die Ausbreitung der Wellen in der drahtlosen Telegraphie, Ann. der Physik **28**, 665 (1909).

Sönnichsen, C., Duch, A. C., Steininger, G., Koch, M., von Plessen, G., Feldmann, J., Launching surface plasmons into nano-holes in metal films, Appl. Phys. Lett. **76**, 140 (2000).

Sorokin, P. P., Lankard, J. R. Stimulated emission observed from an organic dye, chloro-aluminum-phthalocyanine, IBM J. Res. Develop. **10**, 162 (1966).

Spear, J. D., Russo, R. E., Silva, R. J., Collinear Photothermal Deflection Spectroscopy with Light-Scattering Samples, Appl. Opt. **29**, 4225 (1990).

Specht, M., Pedarnig, J. D., Heckl, W. M., Hansch, T. W., Scanning plasmon near-field microscope, Phys. Rev. Lett. **68**, 476 (1992).

Stähelin, M., Bopp, M. A., Tarrach, G., Meixner, A. J., Zschokke-Gränacher, I., Temperature profile of fiber tips used in scanning near-field optical microscopy, Appl. Phys. Lett. **68** (19), 2603 (1996).

Stöckle, R., Fokas, Ch., Deckert, V., Zenobi, R., Sick, B., Hecht, B., Wild, U. P., High Quality Near-Field Optical Probes by Tube Etching, Appl. Phys. Lett. **75** (2), 160 (1999).

Stöckle, R., Schaller, N., Deckert, V., Fokas, Ch., Zenobi, R., Brighter Near-Field Optical Probes by way of Improving the Optical Destruction Threshold, Journal of Microscopy **194** (2/3), 378 (1999).

Stockman, M. I., Faleev, S. V., Bergman, D. J., Localization versus Delocalization of Surface Plasmons in Nanosystems: Can One State Have Both Characteristics?, Phys. Rev. Lett. **87**, 167401 (2001).

Synge, E. H., A Suggested Method for extending Microscopic Resolution into the Ultra-Microscopic Region, Philos. Mag. **6**, 356 (1928).

Taflove, T., Hagness, S., Computational Electrodynamics: The Finite-Difference Time-Domain Method, 2nd ed. (Artech House, Boston 2000).

Tanaka, M., Tanaka, K., Computer simulation for two-dimensional near-field optics with use of a metal-coated dielectric probe, J. Opt. Soc. Am. A **18**, 919 (2001).

Tarkovsky, V. V., Kurstak, V. Yu., Anufrik, S. S., Anomalous dependence of the lasing parameters of dye solutions on the spectrum of microsecond pump laser pulses, Quantum Electron. **33**, 869 (2003).

Teichert, J., Bischoff, L., Hausmann, S., Ion beam synthesis of cobalt disilicide using focused ion beam implantation, J. Vac. Sci. Technol. B **16**, 2574 (1998).

Thiel, R., Eigenschaften angeregter Rhodamin-Farbstoffe und deren Wirkung im Farbstofflaser, Habilitationsschrift (Universität Siegen, 1995), published (Shaker, 1996).

Thio, T., Pellerin, K. M., Linke, R. A., Lezec, H. J., Ebbesen, T. W., Enhanced light transmission through a single subwavelength aperture, Opt. Lett. **26**, 1972 (2001).

Toledo-Crow, R., Yang, P. C., Chen, Y., Vaez-Iravani, M. Near-field differential scanning optical microscope with atomic force regulation, Appl. Phys. Lett. **60**, 2957 (1992).

Tsai, D. P., Kovasc, J., Wang, Z., Moskovits, M., Shalaev, V. M., Suh, J. S., Botet, R., Photon scanning tunneling microscopy images of optical excitations of fractal metal colloid clusters, Phys. Rev. Lett. **72**, 4149 (1994).

Trogisch, S., Aufbau der Abtasteinrichtung eines optischen Nahfeldmikroskops / Photonenrastertunnelmikroskops, Diplomarbeit TU-Dresden (1997).

Valaskovic, G. A., Holton, M., Morrison, G. H., Parameter control, characterization, and optimization in the fabrication of optical fiber near-field probes, Appl. Opt. **34**, 1215 (1995).

van Labeke, D., Barchiesi, J., Probes for scanning tunneling optical microscopy: a theoretical comparison, J. Opt. Soc. Amer. A **10**, 2193 (1993).

van Labeke, D., Baida, F. I., Vigoreux, J.-M., A theoretical study of near-field detection and excitation of surface plasmons, Ultramicroscopy **71**, 351 (1998).

Vasilev, K., Knoll, W., Kreiter, M., Fluorescence intensities of chromophores in front of a thin metal film, J. Chem. Phys. **120**, 3439 (2004).

Vohnsen, B., Bozhevolnyi, S. I., Characterization of near-field optical probes, Appl. Opt. **38**, 1792 (1999).

Vohnsen, B., Bozhevolnyi, S. I., Optical characterisation of probes for photon scanning tunnelling microscopy, J. Microsc. **194**, 311 (1999).

Wait, J. R., Electromagetic Waves in Stratified Media (Oxford University Press, Oxford 1996).

Waldeck, D. H., Alivisatos, A. P. Harris, C. B., Nonradiative damping of molecular electronic excited states by metal surfaces, Surf. Sci. **158**, 103 (1985).

Wallis, R. F., Maradudin, A. A., Stegeman, G. I., Surface polariton reflection and radiation at end faces, Appl. Phys. Lett. **42**, 764 (1983).

Weber, W. H., Eagen, C. F., Energy transfer from an excited dye molecule to the surface plasmons of an adjacent metal, Opt. Lett. **4**, 236 (1979).

Weeber, J.-C., Dereux, A., Girard, C., Krenn, J. R., Goudonnet, J.-P., Plasmon polaritons of metallic nanowires for controlling submicron propagation of light, Phys Rev. B **60**, 9061 (1999).

Weeber, J.-C., Girard, C., Krenn, J. R., Dereux, A., Goudonnet, J.-P., Near-field optical properties of localized plasmons around lithographically designed nanostructures, J. Appl. Phys. **86**, 2576 (1999).

Weeber, J.-C., Krenn, J. R., Dereux, A., Lamprecht, B., Lacroute, Y., Goudonnet, J. P., Near-field observation of surface plasmon polariton propagation on thin metal stripes, Phys. Rev. B **64**, 045411 (2001).

Wehner, G. K., Controlled Sputtering of Metals by Low-Energy Hg Ions, Phys. Rev. **102**, 690 (1956).

Wehry, E. L., Structural and environmental factors in fluorescence, in: Fluorescence; Theory, Instrumentation, and Practice, Guilbault, G. G. (ed.) (Dekker, New York 1967).

Wei, P. K., Fann, W. S., The effect of humidity on probe-sample interactions in near-field scanning optical microscopy, J. Appl. Phys. **87**, 2561 (2000).

Wendler, L., Haupt, R., Long-range surface plasmon-polaritons in asymmetric layer structures, J. Appl. Phys. **59**, 3289 (1985).

Wendler, L., Haupt, R., An Improved Virtual Mode Theory of ATR Experiments on Surface Polaritons, Application to Long-Range Surface Plasmon-Polaritons in Asymmetric Layer structures, phys. stat. sol. (b) **143**, 131 (1987).

Wenzel, T., Bosbach, J., Stietz, F., Träger, F., In situ determination of the shape of supported silver clusters during growth, Surf. Sci. **432**, 257 (1999).

Whitmore, P. M., Robota, H. J., Harris, C. B., Mechanisms for electronic energy transfer between molecules and metal surfaces: a comparison of silver and nickel, J. Chem. Phys. **77**, 1560 (1982).

Wickramasinghe, H. K., Williams, C. C., Apertureless Near Field Optical Microscope, U.S. Patent 4,947,034 (April 28th, 1989).

Williamson, R. L., Miles, M. J., Melt-drawn scanning near-field optical microscopy probe profiles, J. Appl. Phys. **80**, 4804 (1996).

Wokaun, A., Lutz, H.-P., King, A. P., Wild, U. P., Ernst, R. R., Energy transfer in surface enhanced luminescence, J. Chem. Phys. **79**, 509 (1983).

Wu, Z.-C., Arakawa, E. T., Inagaki, T., Thundat, T., Experimental observation of a long-range surface mode in metal island films, Phys. Rev. B **49**, 7782 (1993).

Xia, Y., Gates, B., Yin, Y., Lu, Y., Monodispersed Colloidal Spheres: Old Materials with New Applications, Adv. Mater. **12**, 693 (2000).

Xiao, M., Nieto, J., Machorro, R., Siqueiros, J., Escamilla, H., Fabrication of Probe Tips for Reflection SNOM: Chemical Etch and Heating Pulling Methods, J. Vac. Sci. Tech. B **15**, 1516 (1997).

Yakobson, B. I., Moyer, P. J., Paesler, M. A., Kinetic limits for sensing tip morphology in near-field scanning optical microscopes, J. Appl. Phys **73**, 7984 (1993).

Yakobson, B. I., Paesler, M. A., Tip optics for illumination NSOM: Extended zone approach, Ultramicroscopy **57**, 204 (1995).

Yang, F., Samples, J. R., Bradberry, G. W., Long-range surface modes supported by thin films, Phys. Rev. B **44**, 5855 (1991).

Zayats, A. V., Smolyaninov, I. I., Near-field photonics: surface plasmon polaritons and localized surface plasmons, J. Opt. A: Pure Appl. Opt. **5**, 16 (2003).

Zenneck, J., Über die Fortpflanzung ebener elektromagnetischer Wellen längs einer ebenen Leiterfläche und ihre Beziehung zur drahtlosen Telegraphie, Ann. der Physik **23**, 846 (1907).

Zory, P., (ed.), Quantum Well Lasers (Academic, Boston 1993).

Publications

Journal Articles

1. J. Seidel, S. Grafström, Ch. Loppacher, S. Trogisch, F. Schlaphof, and L. M. Eng, Near-Field Spectroscopy with White-Light Illumination, Appl. Phys. Lett. **79** (14), 2291 (2001)

2. J. Seidel, S. Grafström, and L. M. Eng, Surface plasmon transmission across narrow grooves in thin silver films, Appl. Phys. Lett. **82** (9), 1368 (2003)

3. T. Otto, S. Grafström, J. Seidel, and L. M. Eng, Novel transparent electrodes for electro-optical near-field microscopy, Proc. SPIE **5122**, "Advanced optical materials", 369 (2003)

4. J. Seidel, F. I. Baida, L. Bischoff, B. Guizal, S. Grafström, D. Van Labeke, and L. M. Eng, Coupling between surface plasmon modes on metal films, Phys. Rev. B (Rapid Communications) **69**, 121405(R) (2004)

5. J. Seidel, F. I. Baida, L. Bischoff, B. Guizal, S. Grafström, D. Van Labeke, and L. M. Eng, Coupling between surface plasmon modes on metal films, Virtual Journal of Nanoscale Science & Technology **9**, (2004)
[http://www.vjnano.org/nano/]

6. L. M. Eng, S. Grafström, I. Hellmann, Ch. Loppacher, T. Otto, J. Renger, F. Schlaphof, J. Seidel, and U. Zerweck, Nanoscale nondestructive electric field probing in ferroelectrics, organic molecular films and near-field optical nanodevices, Proc. SPIE Int. Soc. Opt. Eng. **5392**, "Testing, Reliability, and Application of Micro- and Nano-Material Systems II", 21 (2004)

7. J. Seidel, S. Grafström, and L. M. Eng, Stimulated emission of surface plasmons at the interface between a silver film and an optically pumped dye solution, submitted to Phys. Rev. Lett.

8. J. Seidel, S. Grafström, L. Bischoff, and L. M. Eng, Focussed ion beam structured grooves for surface plasmon mode coupling in thin silver films, in preparation

9. J. Seidel, S. Grafström, and L. M. Eng, Local photothermal refractive index change by a Gaussian beam, in preparation

Conference Contributions

1. J. Seidel, S. Grafström, Ch. Loppacher, S. Trogisch, F. Schlaphof, and L. M. Eng, Near-Field Imaging and Spectroscopy Using White-Light Illumination, 6th International Conference on Near Field Optics and Related Techniques, Twente (Netherlands) (August 31, 2000)

2. J. U. Schmidt, H. Bergander, S. Grafström, J. Seidel, S. Trogisch, and L. M. Eng, Non-contact Shear Force Feedback for Near-Field Optical Microscopy with 100 pN Force Resolution, 6th International Conference on Near Field Optics and Related Techniques, Twente (Netherlands) (August 28, 2000)

3. J. Seidel, S. Grafström, Ch. Loppacher, S. Trogisch, F. Schlaphof, and L. M. Eng, Near-Field Imaging and Spectroscopy Using White-Light Illumination, Scanning Probe Microscopy in Nanotechnology, Wroclaw (Poland) (July 10, 2001).

4. J. Seidel, S. Grafström, L. Eng, Surface Plasmon Propagation in Structured Metal Films, DPG-Frühjahrstagung, Regensburg (March 13, 2002)

5. J. Seidel, Plasmons on Structured Metal Surfaces, Workshop Photonics in Electronics Technologies, Dresden (July 2, 2002)

6. J. Seidel, S. Grafström, L. M. Eng, Surface Plasmon Propagation in Structured Metal Films, 7th International Conference on Near Field Optics and Related Techniques, Rochester NY (USA) (August 12, 2002)

7. J. Renger, V. Deckert, S. Grafström, I. Hellmann, J. Seidel, L. M. Eng, Calculation of the electromagnetic field enhancement at sharp noble metal tips for tip-enhanced Raman scattering, 7th International Conference on Near Field Optics and Related Techniques, Rochester NY (USA) (August 12, 2002)

8. J. Seidel, S. Grafström, L. Bischoff, L. Eng, Surface Plasmon Propagation in Structured Metal Films, DPG-Frühjahrstagung, Dresden (March 24, 2003)

9. J. Renger, J. Seidel, I. Hellmann, S. Grafström, V. Deckert, L. M. Eng, Field Enhancement at Sharp Metal Tips, The International Symposium on Optical Science and Technology, SPIE's 48th Annual Meeting, San Diego CA (USA) (August 4, 2003)

10. J. Seidel, S. Grafström, L. Bischoff, L. M. Eng, Surface Plasmon Interaction with Single Grooves in Thin Silver Films, The International Symposium on Optical Science and Technology, SPIE's 48th Annual Meeting, San Diego CA (USA) (August 5, 2003)

11. J. Seidel, J. Renger, S. Grafström, L. Bischoff, L. Eng, Surface Plasmon Propagation in Structured Metal Films, Surface Plasmon Photonics, EuroConference on Nano-Optics, Granada (Spain) (September 21, 2003)

12. P. Olk, J. Seidel, S. Grafström, L. Eng , F. Baida, D. Van Labeke, M. Ott, L. Bischoff, Surface Plasmon Propagation In Metallic Nanostructures, DPG-

Frühjahrstagung, Regensburg (March 10, 2004)

13. J. Seidel, S. Grafström, L. Bischoff, L. Eng, Surface Plasmon Interaction with Single Grooves in Thin Silver Films, E-MRS Spring Meeting, Strasbourg (France) (May 24, 2004)

14. J. Seidel, S. Grafström, L. Bischoff, L. Eng, Surface Plasmon Propagation in Structured Metal Films, International Workshop and Seminar on Cooperative Phenomena in Optics and Transport in Nanostructures, Dresden (June 10-20, 2004)

15. J. Seidel, S. Grafström, L. M. Eng, Experiments on Stimulated Emission of Surface Plasmons, The 8th International Conference on Near-field Nano Optics & Related Techniques, Seoul (South Korea) (September 6, 2004)

16. P. Olk, T. Härtling, J. Seidel, J. Renger, S. Grafström, L. M. Eng, M. Ott, M. Möller, Collective Surface Plasmon Propagation in Gold Particle Ensembles, The 8th International Conference on Near-field Nano Optics & Related Techniques, Seoul (South Korea) (September 4, 2004)

17. J. Renger, J. Seidel, P. Olk, S. Grafström, Lukas M. Eng, B. Schmidt, L. Bischoff and C. Akhmadaliev, Focussing of surface plasmon polaritons by triangle-shaped waveguides and coupled SPP resonantors, 2nd Research Workshop and Network Council Meeting, Belfast (UK), December 13-14, 2004

Acknowledgements

I like to thank all those involved with the research presented in this work for their help, guidance, friendship, patience, and criticism.

As head of the group Prof. Lukas Eng has initiated this research and provided the necessary infrastructure and funding. He has influenced this work with many ideas and recommendations and gave me the opportunity to present my work at workshops and conferences.

Dr. Stefan Grafström has supervised many parts of this work by closely following the experiments in all stages. His extensive knowledge and his collection of optomechanical parts helped me out numerous times. Discussions with him have always been a pleasure and proved to be crucial for a deeper understanding and progress of the work presented.

I wish to thank all graduate students that have worked with me and contributed to the findings presented here. Jan Schmidt introduced me to near-field optics with patience and a wide knowledge of the field. Sven Trogisch has spent quite a bit of time with me designing and building the goniometer setup with great enthusiasm. As a welcome side effect I learned something about analogue and digital electronics. Both he and Tobias Otto helped me out with sometimes frustrating computer problems. I also like to thank Tobias for finding fast solutions for problems like missing cables, defect electronic parts, and other things in the lab. Jan Renger and Phillip Olk have been critical discussion partners especially on plasmon properties and electrodynamics. Frank Schlaphof and Ulrich Zerweck, who shared the office with me, had always an open ear for current problems in the lab and shared their ideas and views of the world with me. Thanks go to Frank Sever and Susanne Schneider for numerous shared after-lunch coffees and interesting exchange of views. Dr. Christian Loppacher, Sebastian Teich, Elke Beyreuther, Marc Tobias Wenzel, Thomas Härtling, Robert Lettow, Oliver Mieth, and Enrico Klotzsch have added to the friendly atmosphere in the SPM^2 group. Without all of them it would have been much less fun.

I like to thank Sylke Furkert for sedulously preparing the numerous SNOM fibre tips that I broke in the lab. Thanks also go to Ellen Kern for the SEM imaging and to Volker Trepte, a master of his trade, who contributed some indispensable handmade mechanical parts to the setup. Ralf Raupach designed and built the HF amplifier, which was able to fully modulate the Pockels cell at 27 MHz which was a great help for me. Kai Schmidt helped me out several times, especially on a severe computer breakdown when I was finishing my thesis.

Cooperations with other groups have been an essential part of my work. Special thanks go to Lothar Bischoff at the Research Center Rossendorf, who spent a lot of time with me at the FIB to produce the groove structures. The cooperation with the group of Prof. Daniel van Labeke in Besançon has provided helpful input to this work. I especially like to thank Dr. Fadi Baida who performed the FDTD calculations.

I have enjoyed working in the good atmosphere at the Institute of Applied Photophysics. The people at the institute have been helpful many times with advice and equipment and were a pleasure to work with.

Last but not least, I thank my parents for their great support during the time of my university education who made successful and untroubled work possible.

Die vorliegende Arbeit wurde am Institut für Angewandte Physik der Technischen Universität Dresden unter wissenschaftlicher Betreuung von Prof. Dr. Lukas M. Eng durchgeführt.

Versicherung

Hiermit versichere ich, dass ich die vorliegende Arbeit ohne unzulässige Hilfe Dritter und ohne Benutzung anderer als der angegebenen Hilfsmittel angefertigt habe; die aus fremden Quellen direkt oder indirekt übernommenen Gedanken sind als solche kenntlich gemacht. Die Arbeit wurde bisher weder im Inland noch im Ausland in gleicher oder ähnlicher Form einer anderen Prüfungsbehörde vorgelegt.